

Development and applications of high speed and hyperspectral nonlinear microscopy

Lauren E. Grosberg

Submitted in partial fulfillment of the
requirements for the degree
of Doctor of Philosophy
in the Graduate School of Arts and Sciences

COLUMBIA UNIVERSITY

2013

©2013

Lauren E. Grosberg

All Rights Reserved

ABSTRACT

Development and applications of high speed and hyperspectral nonlinear microscopy

Lauren E. Grosberg

Nonlinear microscopy refers to a range of laser scanning microscopy techniques that are based on nonlinear optical processes such as two-photon excited fluorescence and second harmonic generation. Nonlinear microscopy techniques are powerful because they enable the visualization of highly scattering biological samples with subcellular resolution. This capability is especially valuable for in vivo and live tissue imaging since it can provide both structural and functional information about tissues in their native environment. With the use of a range of exogenous dyes and intrinsic contrast, in vivo nonlinear microscopy can be used to characterize and measure dynamic processes of tissues in their normal environment. These advances have been particularly relevant in neuroscience, where truly understanding the function of the brain requires that its neural and vascular networks be observed while undisturbed. Despite these advantages, in vivo nonlinear microscopy still faces several major challenges.

First, observing dynamics that occur in large areas over short time scales, such as neuronal signaling and blood flow, is challenging because nonlinear microscopy generally requires scanning to create an image. This limits the study of dynamic behavior to either a single plane or to a small subset of regions within a volume. Second, applications that rely on the use of exogenous dyes can be limited by the need to stain tissues before imaging, the availability of dyes, and specificity that can be achieved. Usually considered a nuisance, endogenous tissue contrast from autofluorescence or structures exhibiting second harmonic

generation can produce stunning images for visualizing subcellular morphology. Imaging endogenous contrast can also provide valuable information about the chemical makeup and metabolic state of the tissue. Few methods have been developed to carefully and quantitatively examine endogenous fluorescence in living tissues.

In this thesis, these two challenges in nonlinear microscopy are addressed. The development of a novel hyperspectral two-photon microscopy method to acquire spectroscopic data from tissues and increase the information available from endogenous contrast is presented. This system was applied to visualize and identify sources of endogenous contrast in gastrointestinal tissues, providing robust references for the assessment of normal and diseased tissues. Secondly, three methods for high speed volumetric imaging using laser scanning nonlinear microscopy were developed to address the need for improved high-speed imaging in living tissues. A spectrally-encoded high-speed imaging method that can provide simultaneous imaging of multiple regions of the living brain in parallel is presented and used to study spontaneous changes in vascular tone in the brain. This technique is then extended for use with second harmonic generation microscopy, which has the potential to greatly increase the degree of multiplexing. Finally, a complete system design capable of volumetric scan rates $>1\text{Hz}$ is shown, offering improved performance and versatility to image brain activity.

Contents

List of Figures	iv
List of Tables	vii
Acknowledgments	viii
Publications and Presentations Related to the Thesis	x
Definitions and list of acronyms	xii
Chapter 1 Introduction and Background	1
1.1 Photon interactions	3
1.1.1 Absorption and dispersion	3
1.1.2 Scattering and anisotropy	10
1.1.3 Fluorescence	12
1.1.4 Nonlinear interactions	18
1.2 Optical microscopy	24
1.2.1 Basic concepts in optical microscopy	24
1.2.2 Confocal laser scanning microscopy	29
1.2.3 Nonlinear laser scanning microscopy	32
1.3 Applications of nonlinear microscopy	38
1.3.1 Imaging in research	38

1.3.2	Clinical relevance	39
1.3.3	Neuroscience	40
Chapter 2	Hyperspectral nonlinear microscopy	44
2.1	Intrinsic contrast imaging.	46
2.1.1	Endogenous fluorescence	46
2.1.2	Changes in intrinsic contrast through the onset of cancer	48
2.2	Hyperspectral imaging system	51
2.2.1	Considerations for spectral imaging	51
2.2.2	Instrument design for hyperspectral two-photon microscopy	52
2.3	Hyperspectral nonlinear imaging of freshly excised tissues	57
2.3.1	Morphological examination	57
2.3.2	Linear unmixing for fluorescence identification and image segmentation	59
2.4	Application: hyperspectral nonlinear microscopy in normal and diseased gas- trointestinal tissues	63
2.4.1	Animal models	63
2.4.2	Morphology of the lower gastrointestinal tract	64
2.4.3	Image guided two-photon spectroscopy	67
2.4.4	Origin of intrinsic contrast	72
2.4.5	Linear unmixing	74
2.4.6	Goodness of fit	80
2.4.7	Summary	82
Chapter 3	Development of techniques for fast 3D nonlinear microscopy	84
3.1	Current state of the art for 3D nonlinear microscopy	87
3.2	Multiplane imaging using spectral encoding	94
3.2.1	Spectral encoding and linear unmixing	94

3.2.2	Instrument design for dual beam, dual plane imaging	96
3.2.3	Application: resting-state hemodynamics	98
3.2.4	Summary	106
3.3	Multiplexed SHG microscopy with spectrally resolved detection	109
3.3.1	Extension of dual plane spectral encoding to SHG microscopy	109
3.3.2	Parallelization of SHG microscopy to more than two foci	110
3.3.3	Proof of principle demonstration	114
3.3.4	Summary	118
3.4	Resonant scanning with remote focusing	119
3.4.1	Technical considerations for fast scanning in 2D	119
3.4.2	Resonant scanning system design and characterization	124
3.4.3	Remote focusing with an electrically tunable lens	131
3.4.4	In vivo demonstration of system capability	138
	Summary and future directions	149
	Bibliography	151

List of Figures

1.1	Electron oscillations in response to a periodic driving force.	5
1.2	Absorption and dispersion	8
1.3	Light propagation in an absorbing medium	9
1.4	Light propagation in a scattering medium	11
1.5	Mean free path for scattering	11
1.6	Chemical structures of example fluorophores	13
1.7	Jablonski diagram for an example molecule.	14
1.8	General absorption and fluorescence emission spectra	15
1.9	Energy diagram and excitation-emission spectra for TPEF	19
1.10	Comparison of one-photon (green) and two-photon (red) excitation spectra .	21
1.11	Energy diagram and excitation-emission spectra for S/THG	22
1.12	Basic ray tracing rules	24
1.13	Numerical aperture	25
1.14	The Airy pattern and Rayleigh criterion for point resolution	26
1.15	Spherical, comatic, and chromatic aberrations	28
1.16	Images that compare wide field and confocal microscopy	30
1.17	Principle of confocal microscopy	30
1.18	Optical sectioning and laser scanning with confocal microscopy	32
1.19	TPEF in scattering tissue	34

1.20	Two-photon microscopy in neuroscience	42
2.1	Metabolism schematic	47
2.2	Custom two-photon microscope design for in vivo imaging	53
2.3	TPEF and SHG imaging of excised tissues with intrinsic contrast	58
2.4	Demonstration of hyperspectral unmixing using four excitation wavelengths.	61
2.5	Comparison of small intestine and colon using white light imaging, two-photon microscopy and conventional H&E histology	66
2.6	The effects of varying two-photon excitation wavelength.	68
2.7	Mean spectral signatures of the four GI tissue components before FAD cali- bration	70
2.8	Mean spectral signatures of the four GI tissue components after FAD calibration	71
2.9	FAD spectral calibration, and corrected spectra of in vitro pure fluorophores	72
2.10	Hyperspectral data unmixing of images of gastric tissues using averaged basis spectra.	75
2.11	False color merges of component images	78
2.12	Residuals for the non-negative least squares fits of hyperspectral data	81
3.1	Signatures of dye combination used for spectrally encoded multiplane imaging	95
3.2	Optical layout for dual beam TPLSM	96
3.3	Characterization of axial resolution for multiplane remote focusing configuration	97
3.4	In vivo configuration for dual plane imaging and unmixing demo	98
3.5	Vascular imaging in two planes shows that baseline fluctuations in vessel tone propagate towards the cortical surface.	101
3.6	Multi-region timing analysis of different locations along a vessel branch. . . .	103
3.7	Comparison of calculation of vessel FWHM to intensity fluctuations	105
3.8	Validation of the dual plane unmixing method	107
3.9	Dual plane SHG imaging.	110

3.10 Optical layout for the spatial separation of excitation wavelengths using a transmission grating	112
3.11 OpTaliX model for multi-spot scanning	113
3.12 Spatial separation of wavelengths from a single pulse at the focal plane . . .	114
3.13 SHG image shift for varying central wavelengths.	115
3.14 Two-channel SHG images obtained with 835 nm excitation	117
3.15 Optical layout for resonant scanning and sensitive detection	126
3.16 AO signals required for resonant scanning with Limberger	128
3.17 Experimental setup for remote focusing with an ETL and offset lens.	132
3.18 Axial focal shifts using ETL and various offset lenses	133
3.19 Effect of remote focusing with ETL on numerical aperture	135
3.20 Change in field of view with remote focusing	136
3.21 Voltage signals generated for new scan types that use the ETL	137
3.22 Demonstration of axial scanning to view vasculature	140
3.23 Full field measurement of capillary flow 80 μm below the pial surface	142
3.24 Arterial flow imaging at 400 fps	143
3.25 Arterial flow speed calculations using 1000 fps images	144
3.26 Volume imaging of GCaMP6 using the ETL	146
3.27 Connectivity between neurons in multiple planes using correlation analysis .	147

List of Tables

1.1	Selected fluorescent labels used for TPLSM in the brain	41
2.1	One and two-photon fluorescence excitation and emission properties for endogenous fluorophores.	46
3.1	Advanced techniques for fast 3D scanning nonlinear microscopy	88
3.2	Comparison of high-speed 2D scanning methods, adapted from Prairie Tech.	121
3.3	Commercially available high-speed multiphoton microscopes	125
3.4	Specifications and components for upgraded scanning system	130
3.5	Imaging speed and characteristics for upgraded scan types. Pixel rates used to determine scan speeds for the original system with 3-channel detection are 500 kS/s, and for the resonant scanning system are 10 MS/s.	139

Acknowledgments

I would like to express heartfelt thanks and appreciation to all those who provided support and guidance during my graduate studies. I thank my thesis advisor, Elizabeth Hillman, who gave me the opportunity to work in her lab and whose ideas and expectations taught me to aim high and work hard to succeed. Her advice, critiques, and teaching helped me immensely to grow as a scientist. I am truly grateful for her mentorship and friendship.

My committee members, Drs. Henry Hess, Lance Kam, Wei Min, Ken Shepard, and Andrew Laine, provided important insights and feedback while developing the research proposal that led to this dissertation. I sincerely appreciate their guidance and willingness to provide assistance in my research. I also would like to thank members of the Columbia community whose collaborations were critical to this research project. Drs. Sam Asfaha and Timothy Wang were invaluable resources for all things gastrointestinal - from dissection tips to cancer identification techniques to mouse models. Many thanks for the knowledge transfer and time spent helping me with my studies. Thanks to Drs. Randy Bruno and Clay Lacefield for providing samples and useful discussions on neural networks that helped tailor the development of our imaging system and software.

I am indebted to many colleagues who have provided assistance and valuable discussion, which has significantly contributed to the work presented here. In particular, I would like to acknowledge the contributions of Andrew Radosevich, P. T. Gali Galwaduge, Matt Bouchard, Ugne Klibaite, and Elsa Swanson, all of whom worked directly on the development of our two-photon microscope. I would also like to thank Brenda Chen and Mariel

Kozberg for hours of help with animal experiments and for their friendship. I owe many thanks to all current and former members of the Laboratory for Functional Optical Imaging, for assistance with research and for laughter and conversation.

I would like to acknowledge the National Science Foundation for providing generous funding for this thesis work, and also for the opportunity to perform research in a corporate environment through their graduate fellowship program.

I thank my parents, who have always encouraged and believed in me. I could not have done this without the countless opportunities they ensured for me over the years. Finally, I thank Ryan Field, who impresses me every day with his determination, intelligence, and integrity. I am grateful for his careful editing of this thesis, numerous discussions about research, and for his help with troubleshooting my circuits. Most importantly, I am grateful for his love and constant support, which has made completing this dissertation a pleasure.

Publications and Presentations

Related to the Thesis

Peer Reviewed Publications

Grosberg LE, Chen BR, and Hillman EMC. Simultaneous multiplane in vivo nonlinear microscopy using spectral encoding. *Optics Letters*, Vol. 37, Issue 14, pp. 2967-2969 (2012).

Grosberg LE, Radosevich AJ, Asfaha S, Yang X, Wang TJ, and Hillman EMC. Spectral characterization and unmixing of intrinsic contrast in intact normal and diseased gastric tissues using hyperspectral two-photon microscopy. *PLoS ONE*, 2011. 6(5): p. e19925.

Oral Presentations

Hillman EMC, **Grosberg LE**, Chen BR, Klibaite U, Galwaduge PTG. Multi-plane two photon microscopy for high speed 3D neuroimaging. Part of Proceedings of SPIE Volume 8207G Photons and Neurons IV at BIOS SPIE Photonics West, January 2012; San Francisco, CA.
**Featured in *Nature Photonics* 6, 222–223 (2012) doi:10.1038/nphoton.2012.74

Grosberg LE and Hillman EMC. Dual-beam two-photon microscopy for simultaneous fast acquisition of two focal planes. Part of Proceedings of SPIE Vol. 8086 Advanced Microscopy Techniques II at the European Conferences on Biomedical Optics, May 2011; Munich, Germany.

Conference Abstracts

Kozberg MG, **Grosberg LE**, Hillman EMC. Postnatal development of neurovascular coupling at a cellular and microvascular level. Abstract A-551-0010-00793. The XXVIth International Symposium on Cerebral Blood Flow, Metabolism and Function, May 2013; Shanghai, China. (Poster presentation)

Cayce JM, Bouchard MB, Chernov M, Chen B, **Grosberg L**, Jansen ED, Hillman EMC, Mahadevan-Jansen A. Evaluating the cellular mechanisms of infrared neural stimulation in the rat somato-sensory cortex. Paper 8565-216. Part of Proceedings of SPIE Volume 8565G Neurophotonics at BIOS SPIE Photonics West, February 2013; San Francisco, CA.

Grosberg LE, Radosevich AJ, Bouchard MB, Hillman EMC. Characterization of intrinsic contrast in intact tissues using hyperspectral two-photon microscopy. Society of General Physiologists, New Optical Methods in Cell Physiology, September 2010; MBL Woods Hole, MA. (Poster presentation)

Grosberg LE, Radosevich AJ, Asfaha S, Yang X, Wang TJ, Hillman EMC. 3D visualization of intrinsic contrast in neoplastic colon tissue using hyperspectral two-photon microscopy. In: OSA Biomedical Topical Meetings, OSA Technical Digest, Optical Society of America, April 2010; Miami, FL. (Poster presentation) **Winner of OSA Biomed Best Student Poster Prize

Bouchard MB, **Grosberg LE**, Burgess SA, Hillman EMC. Laser-Scanning Intersecting Plane Tomography (L-SIPT) for high speed 3D optical imaging and microscopy. In: OSA Biomedical Topical Meetings, OSA Technical Digest, Optical Society of America, April 2010; Miami, FL. (Poster presentation)

Grosberg LE, Radosevich AJ, Bouchard MB, Chen BR, Hillman EMC, Hyperspectral Two-Photon Microscopy for 3D Instant Histology. Engineering Conferences International meeting: Advances in Optics for Biotechnology, Medicine and Surgery XI, June 2009; Burlington, VT. (Poster presentation)

Patents

U.S. Patent Application No. 1,115,304, Unpublished (filing date Dec. 17, 2011) (Elizabeth M.C. Hillman and **Lauren E. Grosberg**, applicants) “Concurrent Multi-Region Optical Imaging”

Definitions and list of acronyms

AI	analog input
AO	analog output
DAQ	data acquisition
ETL	electrically tunable lens
FOV	field of view
GI	gastrointestinal
H&E	hematoxylin and eosin
NA	numerical aperture
PBS	polarizing beam splitter
PSF	point spread function
PMT	photomultiplier tube
RGB	red-green-blue
SHG	second harmonic generation
THG	third harmonic generation
TPEF	two-photon excited fluorescence
TPLSM	two-photon laser scanning microscopy

Chapter 1

Introduction and Background

Advances in biology have come largely through the ability to observe. Optical microscopy has played an important role, enabling the discovery of cells and their structure and the existence of microorganisms (Porter, 1976; Fara, 2009). Improvements in optical resolution, sample preparation, and staining techniques led to a deeper understanding of cells as basic biological building blocks (Karling, 1939), the role of bacteria in disease and disease transmission (Pasteur, 2002; Münch, 2003; Pasteur and H. C. Ernst, 2010), and the relationship of chromosomes and heredity (O'Connor Ilona, 2008). More recently, fluorescent labeling has allowed scientists to engineer precisely which molecules or proteins will glow under the microscope, a reversal of the mindset that microscopes can only reveal what is already there (Coons et al., 1941; Chalfie et al., 1994; Tsien et al., 1998). Today, microscopes are a staple in biological research and medical diagnosis. The physical size of microscopes ranges tremendously - some electron microscopes are several stories tall and can generate electrons with energies high enough to pass through thick tissues to enable unprecedented detail in biological imaging (Cyranoski, 2009), while optofluidic devices are being developed on microchips that can be easily distributed (Cui et al., 2008). Advanced techniques continue to be introduced that push the limits of the types of samples that can be imaged, how contrast is obtained, resolution that can be achieved, and the rate that images can be recorded.

This thesis will present some advances in the capability of nonlinear microscopy techniques, with a particular focus on in vivo imaging. Nonlinear microscopy enables the visualization of highly scattering biological samples with subcellular resolution, providing both structural and functional information about tissues in their native environment. The overarching goal of all techniques presented here is to maximize the information that can be obtained from living tissues using nonlinear microscopy. The presentation is organized into three chapters:

Chapter 1 provides a foundational background for the work done in Chapters 2 and 3. The basic photon interactions with matter that are important for nonlinear microscopy are discussed, along with concepts in microscopy. These fundamental principles were considered in instrument and experimental design for the remainder of the thesis. General applications of nonlinear microscopy are discussed to provide broad context for this work; specific motivation for the original research techniques presented are provided at the start of Chapters 2 and 3.

Chapter 2 details the development of a novel hyperspectral two-photon microscopy method to acquire spectroscopic data from tissues as a method to analyze the relative abundance and microscopic distribution of endogenous fluorescence in bulk tissues. A study quantifying the biochemical origin of contrast in particular tissue types in normal and cancerous colon tissue is presented.

Chapter 3 provides a description of three different methods that were developed for high speed, volumetric nonlinear microscopy. The design, characterization, and application of these methods are discussed. Data showcasing the ability of these methods as a valuable tool for live brain imaging in neuroscience is presented.

1.1 Photon interactions

Optical microscopy is fundamentally the observation of how light interacts with a sample. This section is a primer for concepts that were important to understand through the development of the methods presented in Chapters 2 and 3. In Section 1.1.1, the properties of absorption and dispersion are discussed as a result of modeling a molecule as a forced oscillator in an electric field. The information in this section has been drawn largely from textbooks focused on electrodynamics and optics, and many more details can be found in these books (Griffiths, 1999; Hecht, 2002; Demtröder, 2003). Scattering and anisotropy are discussed in Section 1.1.2. Fluorescence and nonlinear interactions are discussed in Sections 1.1.3 and 1.1.4.

1.1.1 Absorption and dispersion

In the classical theory of light absorption and propagation in dielectric materials, light interactions with atoms can be described using a mechanical model of an electron on a spring. The driving force exerted on a bound electron is related to the electron charge q_e and the electric field of the incident light wave $E(t)$ by Equation 1.1, where E_0 is the initial amplitude of the wave, ω is the frequency of the light, and t is time¹:

$$F_{driving} = q_e E(t) = q_e E_0 e^{-i\omega t} \quad (1.1)$$

When the periodic optical field interacts with a naturally oscillating electron bound to an atom, the result is a forced oscillator. The forces governing the motion of the electron are the driving force (Equation 1.1), the damping force, which is proportional to the velocity of the electron, and the dipole interaction force, or restoring “spring” force, which is proportional to the position of the electron. Summing these forces and using Newton’s second law gives

¹Complex notation is used to describe the electric field. The actual wave function is the real part of E ; $Re\{E_0 e^{-i\omega t}\}$

Equation 1.2, where x_e is the position of the electron, m_e is the mass of an electron, γ is a damping constant, and ω_0 is the naturally occurring oscillation frequency of the electron.

$$m_e \frac{d^2 x_e}{dt^2} = F_{total} = q_e E_0 e^{-i\omega t} - m_e \gamma \frac{dx_e}{dt} - m_e \omega_0^2 x_e \quad (1.2)$$

Equation 1.2 can be rearranged into the standard form for an inhomogeneous second order differential equation with a solution given by

$$x_e(t) = \frac{q_e}{m_e} \cdot \frac{1}{\omega_0^2 - \omega^2 - i\omega\gamma} E_0 e^{-i\omega t} \quad (1.3)$$

Since the sinusoidal wave is written in complex notation (i.e., using $e^{-i\omega t}$), any phase information is absorbed into the constant in front of the exponential. The imaginary term in the denominator indicates that there is a phase shift that varies with the frequency of the input light. The phase relationship is shown in Figure 1.1. When the frequency of the driving optical field ω matches the frequency of the atom ω_0 , resonance occurs and the amplitude of the electron oscillation is at its largest. For cases off-resonance, the electron oscillation is much weaker.

A molecule consists of many bound electrons, and this analysis assumes that the ‘electron’ is really the electron cloud, and its position oscillates with respect to the positive nucleus. The forced oscillation induced by the electric field causes a molecule to become polarized, illustrated in Figure 1.1A. The degree of polarization is described by the induced dipole moment, which is time-varying and given by:

$$p(t) = q_e x_e(t) = \frac{q_e^2}{m_e} \cdot \frac{1}{\omega_0^2 - \omega^2 - i\omega\gamma} E_0 e^{-i\omega t} \quad (1.4)$$

In a sample with N molecules per unit volume, the macroscopic polarization P is the sum of all the dipole moments in that volume. For simplicity, assume that all oscillators within

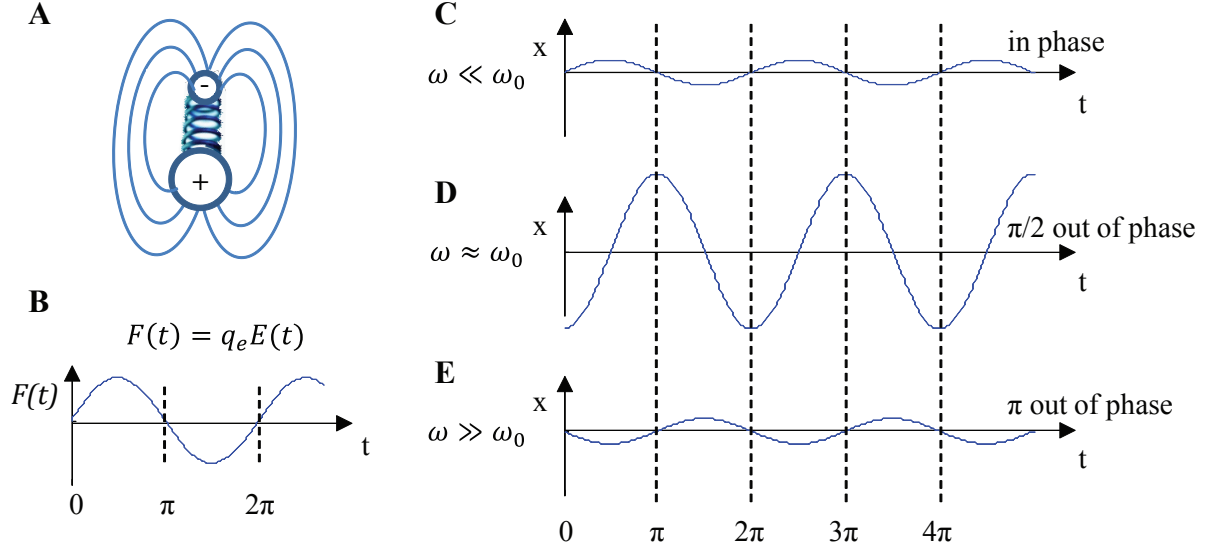


Figure 1.1: Electron oscillations in response to a periodic driving force. A. The spring model for an atom behaves like an electric dipole. B. Driving force arising from an optical electric field. C. For light frequencies far below resonance, the electron oscillation is weak and in phase with the light. D. At resonance, the electron oscillation is strong and lags $\pi/2$ behind the driving field. E. Driving frequencies much larger than resonance produce weak electron oscillations that are π out of phase with the optical wave.

the volume have the same resonant frequencies and damping coefficients². The relationship is given by:

$$P(t) = Nq_e x_e(t) = \frac{Nq_e^2}{m_e} \cdot \frac{1}{\omega_0^2 - \omega^2 - i\omega\gamma} E_0 e^{-i\omega t} \quad (1.5)$$

The polarization P is also related to the E field by the susceptibility, χ_e , and the permittivity of free space, ϵ_0 , by Equation 1.6

$$P(t) = \epsilon_0 \chi_e E(t) \quad (1.6)$$

Equating the proportionality constants in Equations 1.5 and 1.6 gives the definition of the electric susceptibility, χ_e , which quantifies the degree to which a particular dielectric material

²In reality, the electrons contributing to the dipole moment in a molecule have different frequencies and damping coefficients. Equation 1.5 can be generalized to account for this by replacing the complex amplitude $\frac{1}{\omega_0^2 - \omega^2 - i\omega\gamma}$ with $\sum_j \frac{f_j}{\omega_{0j}^2 - \omega^2 - i\omega\gamma_j}$, where the sum describes a molecule with f_j oscillators with j frequencies ω_{0j} and damping coefficients γ_j (see Griffiths, 1999, chap. 9) and (Hecht, 2002, chap. 3-4).

becomes polarized in response to an electric field:

$$\chi_e(t) = \frac{Nq_e^2}{\epsilon_0 m_e} \cdot \frac{1}{\omega_0^2 - \omega^2 - i\omega\gamma} E_0 e^{-i\omega t} \quad (1.7)$$

Equations 1.1 through 1.7 have described the way light affects a material. The interactions discussed depend on properties of the material and the frequency of the driving field. The goal of this derivation is to provide a physical basis for some observed behavior of light as it propagates through a medium. Of particular importance to this thesis are the observations that 1) light is attenuated as it travels through materials and 2) dispersion occurs as a function of wavelength. To get at this point, consider a plane wave propagating through space and time:

$$E(z, t) = E_0 e^{i(\tilde{k}z - \omega t)} \quad (1.8)$$

The variables in Equation 1.8 have been defined above, except for the spatial dependence of the field, z , and the spatial constant, \tilde{k} . This constant is determined by substituting Equation 1.8 into the wave equation (Equation 1.9). The permittivity of the material is ϵ , and the permeability of free space is μ_0 , which is used instead of a material-specific permeability since it is very close to the permeability of nonmagnetic materials.

$$\nabla^2 E = \epsilon \mu_0 \frac{\partial^2 E}{\partial t^2} \quad (1.9)$$

From Equations 1.8 and 1.9, the constant \tilde{k} is:

$$\tilde{k} = \omega \sqrt{\epsilon \mu_0} \quad (1.10)$$

The permittivity and the susceptibility are related by:

$$\epsilon = \epsilon_0 (1 + \chi_e) \quad (1.11)$$

Substituting with Equation 1.11 and using $c = 1/\sqrt{\epsilon_0\mu_0}$ gives

$$\tilde{k} = \omega\sqrt{\epsilon\mu_0} = \omega\sqrt{\epsilon_0\mu_0(1 + \chi_e)} = \frac{\omega}{c}\sqrt{(1 + \chi_e)} \quad (1.12)$$

$$\tilde{k} = \frac{\omega}{c}\sqrt{1 + \frac{Nq_e^2}{\epsilon_0 m_e} \cdot \frac{1}{\omega_0^2 - \omega^2 - i\omega\gamma}} \quad (1.13)$$

Equation 1.13 can be simplified to exclude the radical expression using the binomial approximation for small values of x .

$$\tilde{k} \approx \frac{\omega}{c} \left(1 + \frac{Nq_e^2}{\epsilon_0 m_e} \cdot \frac{1}{\omega_0^2 - \omega^2 - i\omega\gamma} \right) \quad (1.14)$$

Separating \tilde{k} into its real and imaginary components can be done by multiplying numerator and denominator in the final term of Equation 1.14 by the complex conjugate of the denominator. The constant \tilde{k} can therefore be written as Equation 1.15, where, k and κ are the real and imaginary components.

$$\tilde{k} = k + i\kappa \quad (1.15)$$

Now, \tilde{k} is substituted back into Equation 1.8 and an exponential falls out:

$$E(z, t) = E_0 e^{-\kappa z} e^{i(kz - \omega t)} \quad (1.16)$$

Equation 1.16 shows that an E field propagating through a dielectric medium loses energy exponentially. The attenuation rate constant is given by the imaginary part of Equation 1.14 and is defined as the absorption coefficient α (also commonly written as μ_a):

$$\alpha \equiv 2\kappa = \frac{\omega^2}{c} \left(\frac{Nq_e^2}{\epsilon_0 m_e} \cdot \frac{\gamma}{(\omega_0^2 - \omega^2)^2 + \omega^2\gamma^2} \right) \quad (1.17)$$

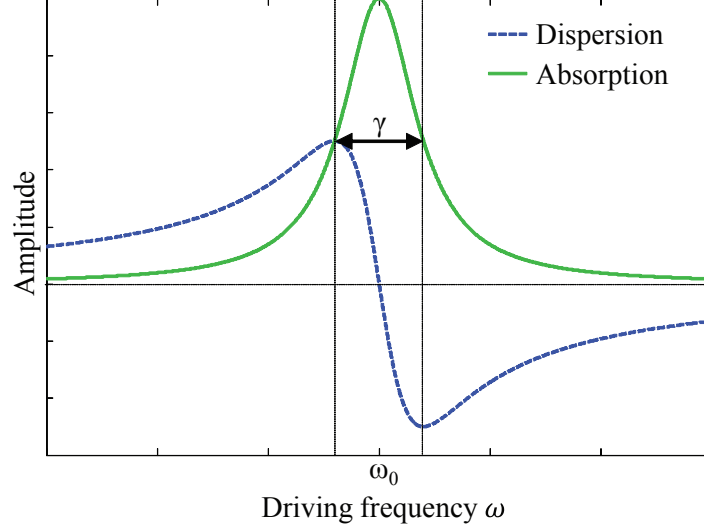


Figure 1.2: The real and imaginary components of the wavevector give the dispersion and the absorption, respectively, of light in a dielectric medium.

The wave velocity, ν , can also be described by Equation 1.16 and is ω/k . The refractive index in a medium, n , is defined as the ratio of the speed of light in a vacuum to the speed of light in the medium. Like the absorption coefficient, the refractive index can be written in terms of the frequency of the light and the properties of the material through which the light propagates:

$$n \equiv \frac{c}{\nu} = \frac{ck}{\omega} = 1 + \left(\frac{Nq_e^2}{2\epsilon_0 m_e} \cdot \frac{(\omega_0^2 - \omega^2)}{(\omega_0^2 - \omega^2)^2 + \omega^2 \gamma^2} \right) \quad (1.18)$$

The absorption coefficient and index of refraction for a medium are shown as a function of the frequency of light in Figure 1.2. Around the resonant frequency of the material, the refractive index is decreasing and absorption is at its highest. As a result, materials do not transmit light well in this region. In optics, lenses are designed to work with particular wavelength ranges of light because of the properties of the material used to construct the lens. In general, resonant frequencies of molecules making up a material are scattered through the spectrum. Most of the resonant frequencies for glass are in the ultraviolet range of light and dispersion decreases with wavelength in the visible light range (Hecht, 2002). The wavelength

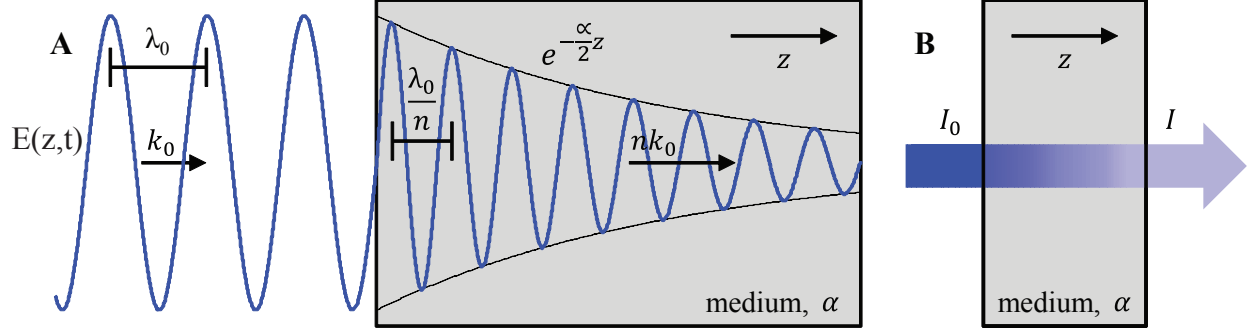


Figure 1.3: Light entering an absorbing medium. A. The electric field of light is attenuated exponentially with the distance travelled in the medium. The wavelength is decreased and the wavevector is multiplied according to the refractive index of the medium. B. Irradiance is attenuated exponentially in a medium.

dependence of dispersion causes white light to split into a rainbow spectrum when passing through a prism. It also causes a short pulse of light containing multiple wavelengths to spread out in time, since the different wavelengths contained in the pulse travel through glass at different speeds. Spatial and temporal dispersion both should be taken into account in microscopic imaging. Figure 1.3A shows the energy wave of light entering an absorbing medium. As discussed above with Equations 1.16 and 1.17, the overall amplitude of the light is attenuated exponentially as it travels through the medium. The effect on the wavelength and propagation vector is also shown in Figure 1.3A. In practice, the intensity of light entering and leaving a medium can be measured to experimentally determine the absorption coefficient of a material, depicted in Figure 1.3B.

The intensity or brightness of the light is the time-averaged square of the energy. From Equation 1.16, the irradiance or intensity is:

$$I(z) = I_0 e^{-\alpha z} \quad (1.19)$$

This result is known as the Beer-Lambert law. As described above and shown in Figure 1.2, the absorption coefficient depends on the properties of the medium and the wavelength of the light passing through it. The absorption properties of materials are often measured ex-

perimentally using this relationship, and can be reported using the absorption cross-section, σ . The absorption cross-section is a measure of the likelihood of absorption and is usually given in units of cm^2 , or other unit area. It is related the absorption coefficient and the number of absorbing molecules per unit volume, N , by

$$\sigma = \frac{\alpha}{N} \quad (1.20)$$

The classical model absorption and dispersion described here is very good for predicting observed phenomena, despite ignoring the quantum nature of electron transitions. However, it cannot account for the probabilistic nature of absorption or nonlinear optical events (Masters and So, 2008, p.114). These interactions are discussed in Sections 1.1.3 and 1.1.4

1.1.2 Scattering and anisotropy

Non-uniformities in media cause light to scatter and change its propagation direction. Scattering can be caused by a range of different non-uniformities, and the type of scattering that occurs can be classified by the size of the particle causing the scatter relative to the wavelength of the light, λ (de Grauw et al., 2002).

- Rayleigh scattering: Scattering particle small compared to λ
- Mie scattering: Scattering particle about the same size as λ
- Geometric scattering: Scattering particle much larger than λ

In biological samples, all three types of scattering occur. Geometric scattering is also called refraction, occurring when light passes into a section with different dispersive properties. Refraction is particularly important to take into account when observing samples through glass or water, two materials that have very different indices of refraction than air. Smaller particles like cells and organelles also cause scattering and are described using Rayleigh and Mie theories.

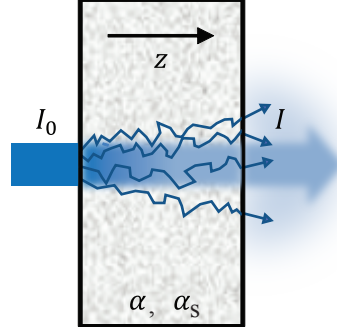


Figure 1.4: Light changes direction as it travels through scattering media. The scattering increases the distance the light travels, and therefore the amount it is attenuated.

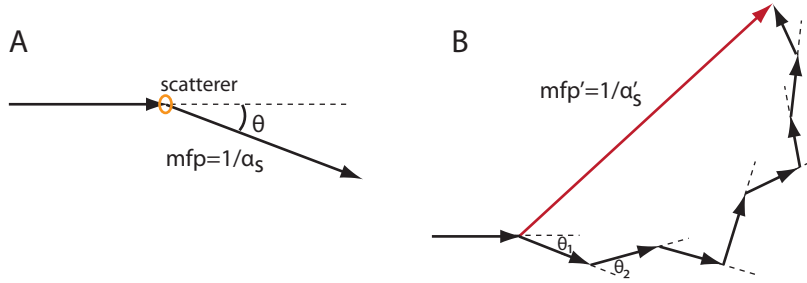


Figure 1.5: A. The mean free path, mfp , is the length a photon travels between scattering events. The anisotropy of the scattering event is given by the angle θ . B. The reduced mean free path, mfp' , describes a series of scattering events with the anisotropy g taken into account.

Analogous to the absorption coefficient, the scattering coefficient, α_s , is a measure of the scattering properties of tissue. Models of light propagation use this to predict possible photon paths. It is important to note that the scattering length of tissues is longer with increasing wavelength. There is no analytical equation to describe the wavelength dependence of the scattering coefficient, but much documentation exists that characterizes scattering coefficients for biological tissues. The mean free path, mfp , is the length travelled by a photon between scattering events, shown in Figure 1.5 (Jacques and Prahl, 1998). It is related to the scattering coefficient by

$$mfp = 1/\alpha_s. \quad (1.21)$$

The anisotropy of the scattering medium is a measure of the directionality of the scattering events, and is given by g , where θ is the angle identified in Figure 1.5.

$$g = \langle \cos\theta \rangle \quad (1.22)$$

The brackets in equation 1.22 indicate averaging over many scattering events. Therefore, if the scattering direction is random, $g = 0$ and the photon propagation is isotropic. For perfectly forward scattering events, $g = 1$, and for backward scattering, $g = -1$. To account for this anisotropy, the reduced scattering coefficient is often given for materials

$$\alpha'_s = \alpha_s(1 - g) \quad (1.23)$$

As shown by Figure 1.5B, the reduced scattering coefficient, and by extension the reduced mean free path, mfp' , can be used to describe many small anisotropic steps. This is particularly useful for describing media which have less absorption than scattering, such as biological tissues in the near-infrared region. A sum of the reduced mean free path over many scattering events can be used in the Beer-Lambert equation as the distance traveled by photons in order to estimate the light attenuation in scattering media.

1.1.3 Fluorescence

Fluorescence occurs when a molecule transitions to an excited state through the absorption of electromagnetic radiation, and subsequently releases energy in the form of light as it returns to its ground state. Typically, molecules that exhibit fluorescence have aromatic rings; bound electrons in these configurations can exist in many states since they are shared between bonds (Lakowicz, 2006, Chapter 1). Chemical structures of several common fluorophores are shown in Figure 1.6.

When a fluorophore absorbs light of sufficient energy, electrons can transition to an

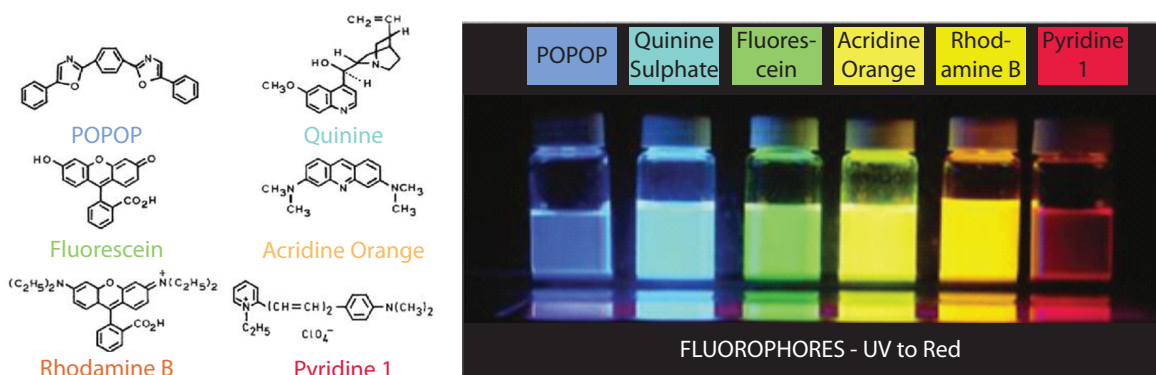


Figure 1.6: Chemical structures of example fluorophores that range in emission from ultra-violet to red. Revised and reproduced from (Lakowicz, 2006)

excited singlet state. The electron can exist in many energetic states within a singlet state, each corresponding to a particular vibrational energy. As the electron transitions back to the ground state, energy can be released either radiatively as light, or non-radiatively, as heat, vibration, or energy transfer. These transitions are often illustrated using a Jablonski diagram (Figure 1.7). The horizontal lines in the Jablonski diagram represent energy levels an electron can occupy. Singlet states are denoted by S_1 , S_2 , etc, and the horizontal lines within each singlet state represent the various vibrational energies a molecule can have. Radiative transitions between energy states are indicated by solid arrows, and non-radiative transitions are indicated by wavy arrows.

As shown by the length of the arrows in Figure 1.7, the energy required for absorption is usually greater than the energy released during emission. Therefore, excitation light has higher energy and shorter wavelength than emission light, with a range of possible excitation and emission energies resulting from vibrational modes within a molecule. These excitation and fluorescence emission spectra are often used to describe a fluorophore, as in Figure 1.8. The difference between the peak emission and peak excitation wavelengths is known as the Stokes shift. For standard fluorescence, the Stokes shift is always positive. The Jablonski diagram illustrates the reason for this: absorption can excite a molecule into any number of vibrational modes, however the extra energy dissipates very quickly through

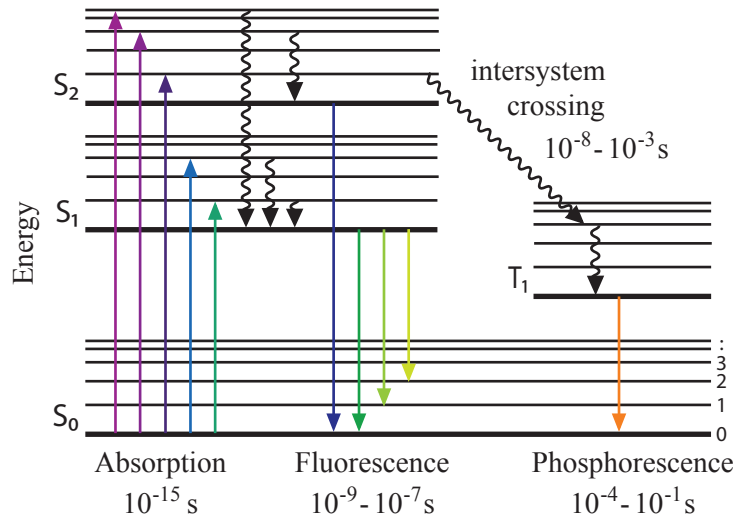


Figure 1.7: Jablonski diagram for an example molecule. S_0 is the ground state, which contains different vibrational energy levels labeled on the far right by 0,1,2,... Radiative transitions between the ground state and excited singlet states (S_1 , S_2) are shown as solid vertical lines. Vibrational relaxation and internal conversion are non-radiative transitions depicted as wavy lines. Transitions may also occur between excited singlet and triplet states, called an intersystem crossing. Radiative decay from a triplet state is called phosphorescence, and occurs on longer time scales and is typically less energetic than fluorescence. (Note that the $S_2 \rightarrow S_0$ transition is rare.)

vibrational relaxation and internal conversion, leaving the electron at the lowest vibrational level in a singlet state. In fact, with few exceptions, most fluorescence is generated from the $S_1 \rightarrow S_0$ transition. As a result, fluorescence emission is independent of the excitation wavelength. Figure 1.8 illustrates this property. Different excitation wavelengths produce identical spectra, however the overall amplitude of emission depends on the wavelength-dependent excitation efficiency.

The timescales noted in Figure 1.7 are related to the rate constants for each respective process. These timescales can be described mathematically using a rate-equation for a population of excited electrons, $N(t)$. Taking the rate constants of radiative relaxation as k_r and non-radiative relaxation as k_{nr} , the rate equation is:

$$\frac{dN(t)}{dt} = -(k_r + k_{nr})N(t) \quad (1.24)$$

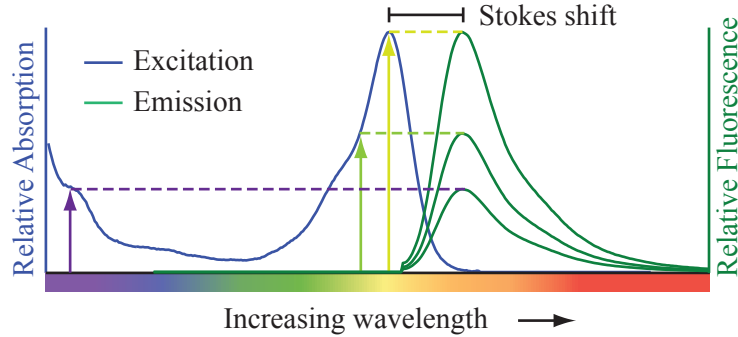


Figure 1.8: Fluorescence excitation and emission spectra of a typical fluorophore. While the distribution of emission light is independent of excitation wavelength, the amplitude does change, as indicated with horizontal dotted lines.

at time t after excitation. Solving gives

$$N(t) = N_0 e^{-t/\tau} \quad (1.25)$$

where τ is called the lifetime of a radiative process (e.g., fluorescence and phosphorescence) and is defined as

$$\tau = \frac{1}{k_r + k_{nr}} \quad (1.26)$$

Equation 1.24 describes a population of excited electrons, and thus the lifetime defined by Equation 1.26 is an average value of the time an electron spends in an excited state. Lifetime is a characteristic property of a fluorophore, and is independent of the signal brightness or fluorophore concentration. Fluorophores with overlapping emission wavelengths but distinct lifetimes can be resolved by measuring the lifetime. Further, lifetimes are sensitive to local environmental factors and can therefore be measured to determine properties such as pH, viscosity, proximity to molecules that can quench fluorescence, and binding to macromolecules (Lakowicz, 2006, Chapter 4).

Not every photon that is absorbed fluoresces. The ratio of the emitted photons to the absorbed photons is another characteristic property of a fluorophore called the quantum yield. The quantum yield, Q , is related to the radiative and non-radiative relaxation rates

by:

$$Q = \frac{k_r}{k_r + k_{nr}} \quad (1.27)$$

Measured fluorescence intensity depends the absorption and emission processes previously described, as well as on the collection efficiency of the measurement system. The total fluorescence signal is given as a function of time t by

$$F(t) = \Phi Q N_{abs}(t) \quad (1.28)$$

where Φ is the collection efficiency of the detection system and N_{abs} is the number of photons absorbed, given by

$$N_{abs}(t) = C\sigma I(t) \int d\vec{r} S(\vec{r}) \quad (1.29)$$

Equation 1.29 gives the probability of photon absorption based on the concentration of the fluorophore, C , and its absorption cross-section, σ (see Equation 1.20). The incident light intensity is split into its temporal component, $I(t)$ and spatial component $S(\vec{r})$, which is integrated over the illumination area. This area is determined by instrumentation geometry.

Fluorescence spectra in vitro and in vivo

Fluorescence emission spectra are generally considered to be characteristic of a fluorophore. As explained by Figure 1.8, the distribution of emission light is independent of excitation. However, the emission properties of a fluorophore can be altered by a variety of environmental factors. From equations 1.28 and 1.29, the emission depends on the fluorophore properties quantum yield and absorption cross-section. Changes in the decay rates of radiative and non-radiative transitions, and thus the quantum yield, can result from varied solvent polarity and viscosity for certain fluorescent molecules. Emission spectra typically become red-shifted for fluorophores that are affected by increased solvent polarity and viscosity (Haidekker et al., 2005). Additionally, the presence of molecules that can quench fluorescence by providing

an alternate decay pathway can alter the quantum yield of a fluorophore. It has been long known that oxygen is an efficient quencher, which certainly can affect *in vivo* fluorescence measurements (Ware, 1962; Lakowicz and Weber, 1973). Finally, fluorophore binding to other molecules can change both absorption ability and quantum yield. In some cases, fluorescent shifts can be used as a probe for binding events.

These dependencies on environmental factors can make spectroscopic measurements of *in vivo* fluorescence difficult to correlate with *ex vivo* references. Certainly, direct measurement of fluorophore concentration *in vivo* is difficult since the quantum yield can change. Strategies for measuring and quantifying *in vivo* fluorescence will be discussed further in Chapter 2.

Fluorophores

Generally, fluorescent molecules can be classified into two groups: intrinsic, or endogenous, biological fluorophores, and extrinsic, or exogenous, fluorescent molecules. Fluorophores exist with a very wide range of absorption and emission properties, quantum yields and lifetimes, and the diversity of available fluorophores is continually growing. Through conjugation of fluorescent probes with antibodies, DNA, and proteins, fluorescence provides specificity in biological experiments. Transgenic labeling can be used to tag virtually any gene using fluorescent proteins (FPs) that have been engineered to fluoresce in a variety of colors (Chalfie et al., 1994; Tsien et al., 1998; Shaner et al., 2005). Several extrinsic dyes are used in this thesis to provide contrast and functional capability for brain imaging.

Intrinsic fluorescence results from a wide range of biomolecules including coenzymes, lipids, and structural proteins. The use of endogenous fluorescence to provide contrast and biochemical information about tissues is a focus of this thesis, and will be discussed in Chapter 2.

1.1.4 Nonlinear interactions

Discussions on nonlinear photon interactions with materials typically begin by expanding the induced polarization P equation (see eq. 1.6) to include its higher order terms:

$$P = \epsilon_0[\chi^{(1)}E^1 + \chi^{(2)}E^2 + \chi^{(3)}E^3 + \dots] \quad (1.30)$$

where $\chi^{(n)}$ is the n^{th} order nonlinear susceptibility, and E is the electric field vector. For most materials, these nonlinear susceptibilities are small. As they are proportional to n^{th} order electric field, nonlinear effects were not observed until lasers were introduced, providing high-energy photon sources. The first term of Equation 1.30 describes linear absorption, scattering, and reflection of light. Second harmonic generation, and sum and difference frequency generation are described by the second term. The third term describes two- and three-photon absorption, third harmonic generation, and stimulated Raman processes. A few of these nonlinear interactions are discussed in greater detail here.

Two-photon excited fluorescence (TPEF)

An electron can transition to an excited molecular state if two simultaneously arriving photons have enough cumulative energy to facilitate the transition. The phenomenon was first predicted in 1931 by Maria Göppert-Mayer in her Ph.D. thesis, but was not verified experimentally until the invention of the laser provided sufficient photon flux for the measurement.

Figure 1.9 illustrates the energy configuration for two-photon excited fluorescence (TPEF). The combined energy of two photons causes an equivalent electronic transition to one that occurs for single photon fluorescence. The two photons each have lower energy than their single photon counterpart. Once the electron is excited, it can return to the ground state radiatively or non-radiatively, as before. Since lower energy photons are used to excite fluorescence, the Stokes shift is negative for TPEF (Figure 1.9B). Additionally, the Stokes

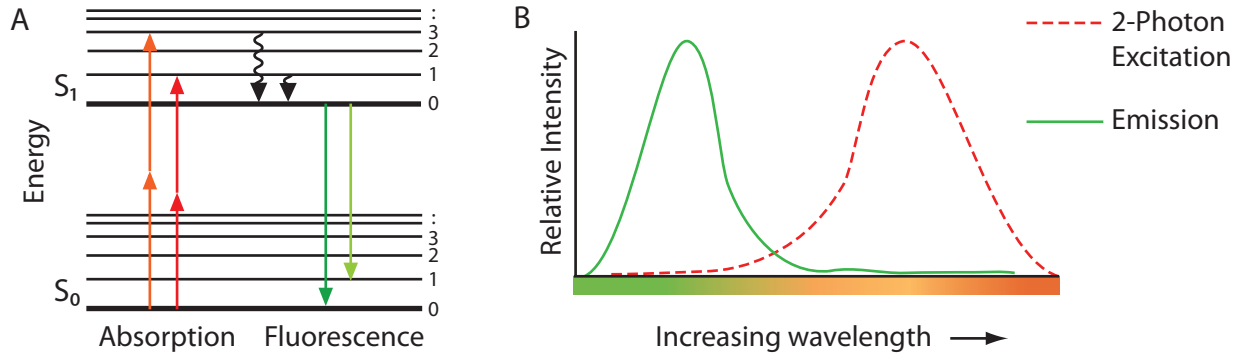


Figure 1.9: Energy diagram and excitation-emission spectrum for two-photon excited fluorescence. A. Jablonski diagram shows that two low-energy photons can cause a molecular transition to an excited state. The combined energy of the two photons is the same as that of one photon for single photon fluorescence. B. In the excitation-emission spectrum for TPEF, the excitation band is red-shifted with respect to the emission range. The Stokes shift is usually much larger than seen in single photon fluorescence.

shift is much larger than typically seen for single-photon fluorescence.

Following (Diaspro and Sheppard, 2002), the probability of a n -photon absorption event is proportional to the probability of finding n photons within the volume a molecule occupies at an instantaneous moment in time. A small cubic volume with side length s and even illumination at wavelength λ has an energy corresponding to the mean number of photons, \bar{n} , at any time within the volume given by

$$E = \bar{n}hc/\lambda \quad (1.31)$$

The intensity, I , within that volume is given by the power transferred per unit area. Since cross-sectional area of the cubic volume is s^2 and the time required for a photon to cross the volume is s/c , the intensity is

$$I = \frac{E}{s^2 \cdot s/c} = \frac{\bar{n}hc^2}{\lambda \cdot s^3} \quad (1.32)$$

Equating the volume s^3 to the mean molar volume V_m divided by Avogadro's number ($N_a = 6.022 \times 10^{23} \text{ mol}^{-1}$) allows solving for the mean number of photons in a molecular volume

in terms of known (or measurable) quantities:

$$\bar{n} = \frac{IV_m\lambda}{N_a hc^2} \quad (1.33)$$

The probability p_n of finding n photons within the molecular volume at any given time is a Poisson distribution based on the calculated mean value obtained in Equation 1.33:

$$p_n = \frac{\bar{n}^n}{n!} \exp(-\bar{n}) \quad (1.34)$$

The probability can be estimated using the first term of a Taylor series expansion since \bar{n} is small, and so the exponential decay term goes to 1. For TPEF, $n = 2$, and the probability is given by

$$p_2 = \frac{1}{2} \bar{n}^2 = \left[\frac{V_m \lambda}{\sqrt{2} N_a hc^2} \right]^2 I^2 \quad (1.35)$$

From Equation 1.35, the probability of two-photon absorption is proportional to the square of the incident photon intensity. For higher order multiphoton absorption events, the intensity scales exponentially with the number of photons absorbed.

Given the quadratic dependence of two-photon absorption on intensity, the emitted fluorescence is also proportional to I^2 . Equation 1.28 can be generalized to include n -photon absorption for an expression of the fluorescence collected as a function of time (Xu, 2002):

$$F(t) = \frac{1}{n} \Phi Q C \sigma_n I^n(t) \int d\vec{r} S^n(\vec{r}) \quad (1.36)$$

Again, Φ is the collection efficiency of the detection system, Q is the quantum efficiency of the fluorophore, C is its concentration, and $I(t)$ and $S(r)$ are the temporal and spatial components of the incident light, respectively. These distributions are dependent on the illumination source and the geometry of the illumination volume, and will be discussed in terms of geometries and laser sources typically used for microscopy in section 1.2.3.

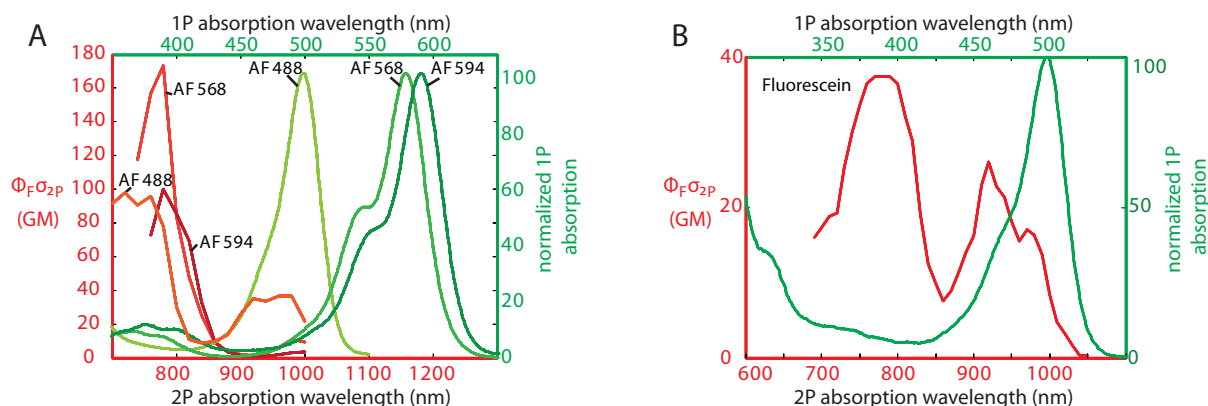


Figure 1.10: Comparison of one-photon (green) and two-photon (red) excitation spectra for A. AlexaFluor dyes and B. fluorescein. Single photon data obtained from Invitrogen and two-photon cross-sections available online from Cornell University DRBIO

The n -photon molecular cross-section, σ_n is a measure of the likelihood that a multi-photon absorption event will occur, and like the single photon absorption coefficient, depends on the energy, or wavelength, of the incident photons. The two-photon cross-section, σ_2 is often reported for molecular probes suitable for TPEF in Göppert-Mayer units (GM), where 1 GM is $10^{-58} \text{ m}^4 \text{ s photons}^{-1}$. The unit choice is convenient since it avoids using large exponentials for most dyes.

A wide range of molecular probes are available for use with TPEF. Many probes that are intended for single photon fluorescence also exhibit TPEF, however the efficiency of a fluorophore for single-photon excitation does not necessarily correlate to two-photon excitation efficiency. Probes have been introduced specifically designed to have high two-photon absorption cross sections (Albota, 1998). A comparison of the absorption cross-sections with single photon absorption peaks for a few AlexaFluor dyes and for Fluorescein is shown in Figure 1.10. As highlighted in the figure, the maximum two-photon cross section does not necessarily correspond to twice the single photon absorption peaks. While the two-photon excitation spectra tend to be blue-shifted with respect to the twice the single photon absorption peaks, emission profiles are the same for one- and two-photon excitation (Xu, 2002).

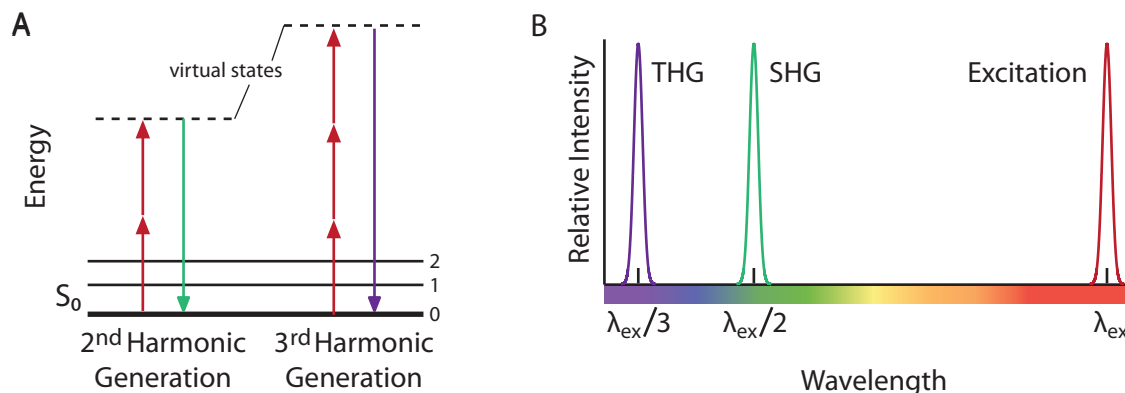


Figure 1.11: Energy diagram and excitation-emission spectra for second and third harmonic generation. Electrons transition to virtual states rather than actual energetic levels, and the energy of the combined photons is conserved.

Second and third harmonic generation (SHG/THG)

Harmonic generation is a nonlinear effect that is very different from fluorescence in that it does not involve an excited state. Instead, multiple photons combine to a virtual energy level and their combined energy is converted to create a new photon with energy equal to that of the combined incident photons. This scatter-like event is energy conserving, and it preserves the coherence of laser light (Campagnola, 2008).

Figure 1.11 shows the energy diagram for the harmonic generated when two photons combine (second harmonic generation, SHG) and when three photons combine (third harmonic generation, THG). No vibrational relaxation occurs, therefore there is not a frequency distribution of generated photons as in fluorescence emission. The narrow peaks Figure 1.11B show that SHG and THG are primarily dependent on the incident wavelength. Since SHG does not involve an excited state and is energy conserving, it largely propagates in the forward direction (Mertz, 2004). Because of this, many SHG measurement setups include detection for transmission geometries. However, the propagation direction of SHG is dependent on the size of the structure, and structures smaller than the wavelength of the second harmonic (biological proteins, for example) exhibit backscattered SHG signal (Mertz and Moreaux, 2001).

SHG occurs only in materials with highly ordered, or noncentrosymmetric, molecular organization (Campagnola and Loew, 2003). It is sensitive to molecular orientation and shows specificity for membranes. In biological tissues, endogenous sources of SHG include collagen, microtubules, muscular myosin, and mitotic spindles.

1.2 Optical microscopy

1.2.1 Basic concepts in optical microscopy

Geometric optics

Light propagation can be modeled as straight rays that change direction only when passing from one medium into another with a different refractive index. This description of light behavior is called ray optics or geometric optics. While many books go into great detail on the topic of ray optics (Hecht, 2002, Ch. 5-6), a few simple rules and definitions are important to mention to preface the remainder of the discussion here (So and Kim, 2008).

First, collimated light has all rays parallel to the optical axis, and when incident on a lens that light is focused at the focal point of the lens, as in Figure 1.12A. Rays incident on a lens on an angle focus along the focal plane perpendicular to the optical axis, as shown in Figure 1.12B. Light originating from a spot on the focal plane becomes collimated after the lens, and the angle that the light makes with the optical axis depends on location of the source on the back focal plane (1.12C and D).

The microscope designs presented in this thesis use a combination of these rules. The most complicated part of the optical design has to do with the objective lens, since it contains many lenses to allow near ideal behavior. Ray models are used in sections 3.3 and 3.4 to predict the system behavior when ideal conditions are disturbed.

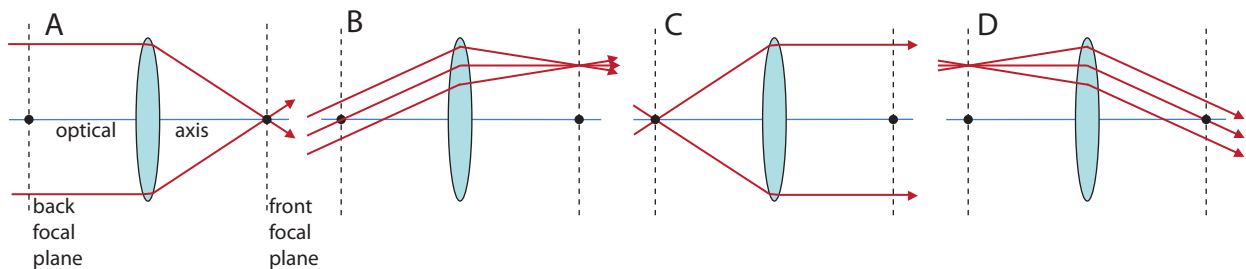


Figure 1.12: Basic rules for ray tracing. The optical axis is labeled in A. Light rays are arrowed red lines, and the back and front focal planes are shown as dashed lines perpendicular to the optical axis.

Numerical aperture

The numerical aperture (NA) of an optical system is a measure of the range of angles over which it can collect light or that are contained in its focused cone. In microscopy, the NA of the objective and condenser lenses determines the focusing power and resolution of the system. The NA is given by

$$NA = n \sin\theta \quad (1.37)$$

where n is the index of refraction of the medium in which light is focused, and θ is the half angle of the cone of light made by the focus spot. The geometry is illustrated in Figure 1.13.

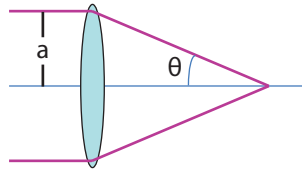


Figure 1.13: The NA of a lens is defined by the half angle, θ , of the cone of light made by the focus spot and the index of refraction of the medium in which light is focused.

Resolution

Lateral resolution. Light is shown in Figure 1.13 focusing down to a point. However, the focused spot is actually a diffraction pattern created as light passes through a circular aperture, such as a pinhole or a lens. The pattern generated is called an Airy disk. The Airy disk consists of a bright central spot surrounded by alternating dark and bright rings as shown in Figure 1.14.

The irradiance I of one ‘slice’ of the Airy disk is also known as the point spread function (PSF) of a point object and is plotted in Figure 1.14A. The analytical expression for the PSF is given in terms of the first order Bessel function, J_1 , the wavenumber k , the

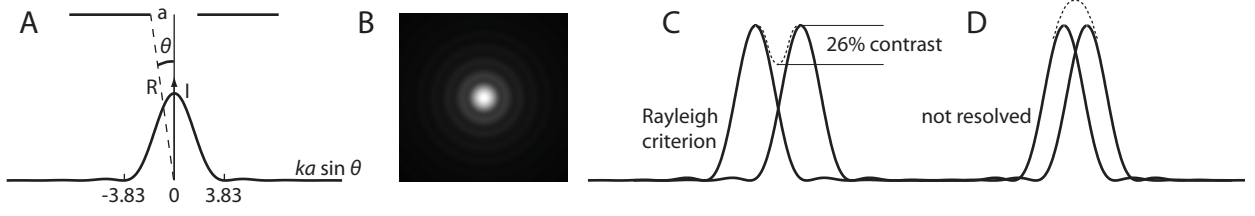


Figure 1.14: A. The Airy pattern for diffraction through a circular aperture. k , wavenumber; a , radius of the aperture; θ , ray angle. B. 2D irradiance pattern, Airy disk. C. The minimum separation between two point sources, represented with Airy patterns, is defined by the Rayleigh criterion. D. Points closer than the Rayleigh limit cannot be resolved.

radius of the aperture a , and the ray angle θ :

$$I = I_0 \left(\frac{2J_1(ka \sin \theta)}{ka \sin \theta} \right)^2 \quad (1.38)$$

Two point objects are considered to be resolved when the maximum of one PSF overlaps with the first dark band of the next PSF (Figure 1.14C). This resolution limit can be calculated by finding the distance from the center of the PSF to its first minimum. From Equation 1.38, the first zero occurs when $J_1(ka \sin \theta) = 0$, or when $ka \sin \theta = 3.83$. Using $k = 2\pi/\lambda$ where λ is the wavelength of the light, and the geometric distances defined in Figure 1.14, this resolution limit is

$$r = 1.22 \frac{R\lambda}{2a} \quad (1.39)$$

For a lens, this resolution limit is usually given in terms of NA, and is known as the Rayleigh criterion for spatial resolution:

$$r = 0.61 \frac{\lambda}{NA} \quad (1.40)$$

An optical system is called diffraction limited when the measured resolution matches the theoretical limit defined by the Rayleigh criterion. Many systems optimize resolution by using shorter wavelength illumination light or objective lenses with high NA.

Axial resolution. A similar approach is used to determine the axial resolution for point objects separated along the optical axis (z-dimension). Two points are considered to be just resolved when the maximum of the axial component of the first PSF overlaps the first minimum of the second. From (Jonkman and Stelzer, 2002), the axial resolution is defined as:

$$r_z = \frac{2\lambda n}{NA^2} \quad (1.41)$$

As an example, an optical system using light with $\lambda = 800\text{nm}$ and a water-immersion ($n = 1.33$) objective lens with a NA of 0.95 has a theoretical axial resolution of $2.36\text{ }\mu\text{m}$. The lateral resolution for the same example would be $0.51\text{ }\mu\text{m}$. Generally, the axial resolution of a system is worse than the lateral resolution.

The axial resolution of a system also defines its depth of field. The depth of field of a system describes the range of positions along the object side of the optical axis that can be clearly resolved by at a fixed image plane. Systems with large NA have short depth of field, and vice versa.

Aberrations

The diffraction limited spot as defined above can be formed only if the wavefront exiting the optical system is not distorted. However, as light passes through a system of optical elements, it inevitably picks up distortions, or aberrations, along the way. Optical aberrations can be classified into two groups: chromatic or monochromatic. Chromatic aberrations are a result of the dependence of refractive index on the frequency or color of light. Monochromatic aberrations are caused by the geometry of lens construction. There are five main types of monochromatic aberrations: spherical, coma, astigmatism, curvature of field, and distortion. In a real optical system, all these aberrations add together for complex image problems.

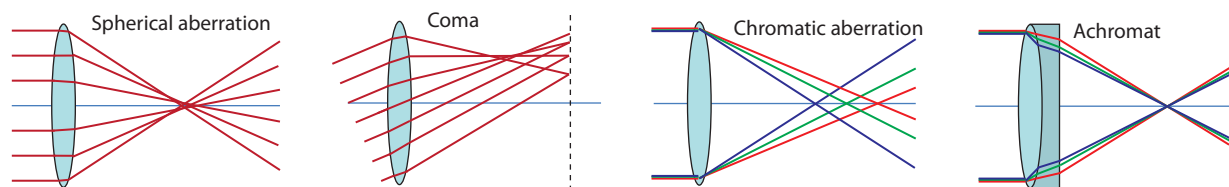


Figure 1.15: Spherical aberration causes a blurred focus because of the radial dependence of the focusing power of a spherical lens. Coma is an off-axis aberration that produces asymmetric spots. Chromatic aberration causes shorter wavelength light to focus closer to the lens along the optical axis.

Monochromatic aberrations. Spherical aberration is common in the vast majority of singlet lenses because most of these lenses are constructed with a spherical shape for one or both sides of the lens. Because of the spherical lens shape, marginal rays are focused closer along the optical axis than paraxial rays, causing a blurred focal spot (Figure 1.15). This is the only monochromatic aberration that occurs regardless of position on or off the optical axis. As the NA increases, the blurring effect from spherical aberration worsens ($\propto \text{NA}^3$). It is possible to specially shape lenses to reduce spherical aberrations, but this drives up the cost of manufacturing enough to make this impractical for most applications.

Coma is an off-axis aberration that gets its name from the comet-like spots it produces at angled image spots. Coma increases with distance from the optical axis along the focal plane. Curvature of field, astigmatism, and distortion likewise worsen for focal spots away from the optical axis. All of these off-axis aberrations are more noticeable for large fields of view.

Chromatic aberration. As discussed in section 1.1.1, the index of refraction for dielectric materials (e.g., materials used for lenses) is dependent on the wavelength of the light. Therefore, as polychromatic light passes through a lens, shorter wavelengths are bent more and have shorter effective focal lengths than longer wavelengths. This effect introduces longitudinal chromatic aberration and is illustrated in Figure 1.15C. Longitudinal chromatic aberrations are proportional to the NA of the lens. Chromatic aberrations can also manifest

in the lateral plane, with shorter wavelengths focusing further away from the optical axis.

Lens correction. Lenses can be designed to correct for many of these aberrations. Achromatic doublets are designed to correct for chromatic and spherical aberrations using two lens materials fused together. Figure 1.15D shows an achromat that is designed to focus the three colors shown to the same point. Typical achromats are designed to for ~ 2 wavelengths, and it is assumed that this correction will result in good performance for the range of wavelengths between the ones for which it was designed.

High NA objective lenses are common in microscopy because they improve resolution. However, because many of these aberrations are proportional to the NA, high NA objective lenses must be carefully designed to compensate for these aberrations. Because of this, objective lenses contain a series of carefully designed lenses, allowing high resolution imaging while minimizing all aberrations mentioned above.

1.2.2 Confocal laser scanning microscopy

Conventional optical microscopes use carefully chosen lens combinations to provide sample magnification with even light illumination, and image the sample to either an eyepiece or camera. The entire sample is illuminated, which allows for simple implementation and efficient detection. However, optical sectioning is poor, and resolution degrades if the sample is highly scattering or thicker than about $5\text{ }\mu\text{m}$ because light from outside the focal plane can reach the eyepiece or detector. The degradation in image quality for thick samples acquired with a conventional microscope is illustrated by Figure 1.16A. The blur seen in the figure is a result of fluorescence from above and below the focal plane contributing to the image.

The confocal microscope was introduced as a way to provide optical sectioning in thicker samples (Pawley, 2006). The improvement is illustrated in Figure 1.16B. Confocal microscopy is fundamentally different from conventional microscopy. First, the illumination source is usually a laser beam and is focused into a spot, as shown in Figure 1.17. The

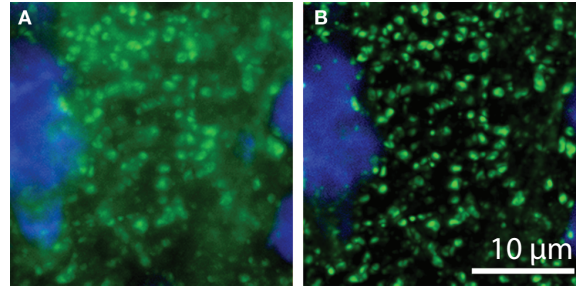


Figure 1.16: Comparison of contrast achieved using (A) wide-field fluorescence microscopy and (B) confocal microscopy. The optical sectioning capability of confocal allows rejection of out-of-focus background for sharper images with better contrast and resolution. Images are of axon boutons labeled for GAD67 (green) and a pyramidal cell stained for Nissl substance (blue). Reproduced from (Sweet et al., 2010).

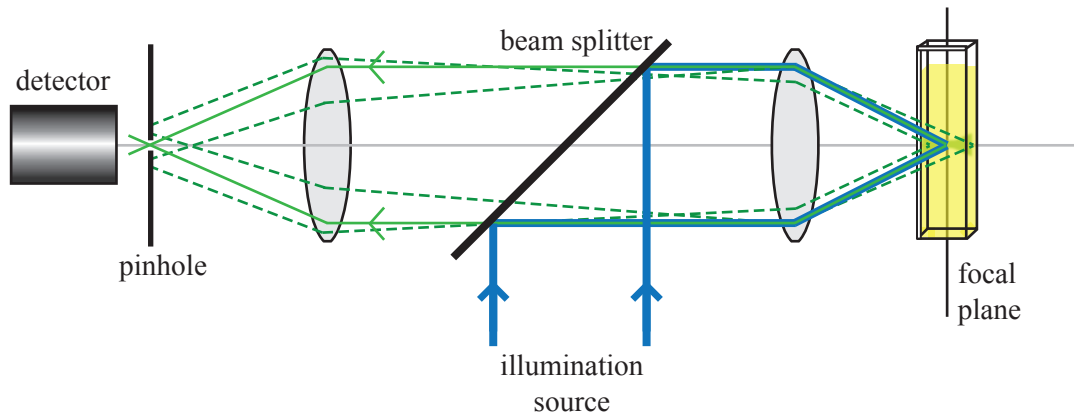


Figure 1.17: Principle of confocal microscopy. Out-of-focus light is rejected from the detector using a pinhole that is conjugate to the focus of the illumination source. The confocal optical system provides optical sectioning for fluorescence and reflection microscopes.

focal spot is mapped back to the detector and a pinhole is used to block fluorescence (or reflectance) signal that does not originate from the focus. The pinhole must be exactly conjugate to the focus for the system to be confocal.

In addition to eliminating out-of-plane fluorescence, the pinhole improves lateral and axial resolution with respect to conventional systems by 30% (Jonkman and Stelzer, 2002). The actual PSF of the confocal imaging system is the convolution of the PSF of the pinhole with that of the focused spot. Therefore, a smaller pinhole will produce an image with higher resolution, however the improvement comes at the expense of signal loss. Taking the improvement into account, the expressions for lateral and axial resolution for confocal

microscopes are

$$r_{xy,confocal} \approx \frac{0.4\lambda}{NA} \quad (1.42)$$

and

$$r_{z,confocal} \approx \frac{1.4\lambda n}{NA^2} \quad (1.43)$$

Samples as thick as a few hundred micrometers can be imaged using confocal microscopy. Optical sections are imaged by moving the objective relative to the sample, or vice versa, as shown in Figure 1.18. By using scan mirrors to produce a raster pattern in the sample, the laser beam excites all points within a 2D field of view (FOV). In the scanned system, the fluorescence emission light must be detected after it is descanned in order for the pinhole to be properly conjugate with the detector. The pinhole enables imaging at depth, but greatly reduces collection efficiency since 1) it only allows ballistic (non-scattered) photons to contribute to the signal and 2) the need for descanning requires the already weak fluorescence signal to pass through many optical components, each one contributing to loss. Because spatial locations in the sample are scanned sequentially, an image viewable by eye or camera is never formed. Fluorescence signal is collected as a time-series and the image is reconstructed using a computer. The need for a computer is another fundamental difference between conventional and laser-scanning microscopy techniques. Since the image is built up in discrete samples, the object must be sampled every $r_{xy,confocal}/2.3$ to get an image with diffraction-limited resolution.

The imaging frame rate of confocal microscopy is ultimately limited because of the need for point-by-point scanning and the limited collection efficiency. Imaging penetration depth is limited because visible excitation light is scattered in the sample, degrading the focused spot. The fluorescence emission is also scattered, and therefore the detected signal is reduced with depth. Note that fluorescence excitation occurs above and below the focus for each scan point, therefore, exposure of the sample to potentially damaging excitation light is generally high, particularly if the entire 3D volume needs to be scanned.

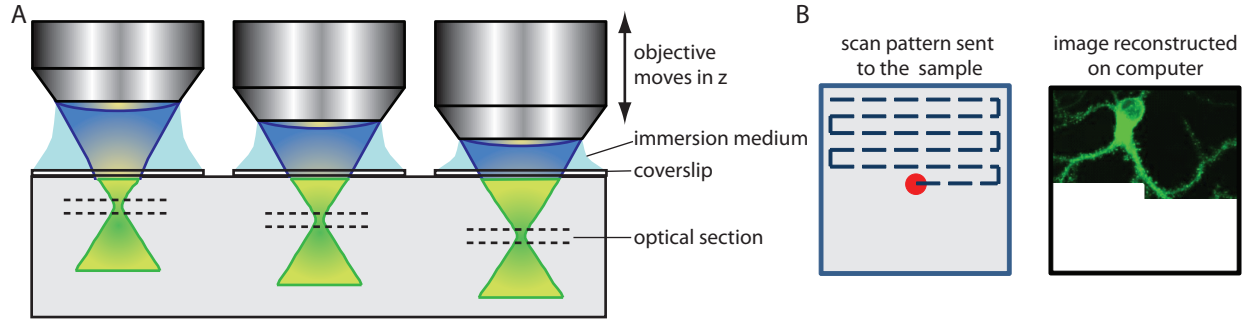


Figure 1.18: A. Axial focusing combined with confocal pinhole detection provides optical sectioning to depths of several hundred micrometers in scattering tissue. B. The scan pattern sent to the sample sequentially excites fluorescence. Images are reconstructed using a computer by mapping the fluorescence signal to the spatial position of the beam at the time the fluorescence was acquired.

1.2.3 Nonlinear laser scanning microscopy

Nonlinear microscopy describes any microscopy technique based on nonlinear optical processes. Examples of nonlinear phenomena that have inspired valuable microscopy tools include two- and three-photon absorption, frequency doubling, sum and difference frequency generation, coherent anti-Stokes Raman scattering, and stimulated Raman scattering. The term ‘multiphoton microscopy’ is often used as a synonym to nonlinear microscopy, as it encompasses all processes that require multiple photon interactions to occur. Two of these methods, two-photon microscopy and second harmonic generation microscopy, are described here.

Two-photon laser scanning microscopy

Two-photon laser scanning fluorescence microscopy (TPLSM) was first demonstrated by Denk et al. in 1990 (Denk et al., 1990). It is similar to confocal microscopy in that it uses a scanning focused laser beam to generate fluorescence. However, instead of using a single photon with energy E to excite fluorescence, it uses 2 simultaneously arriving, lower energy ($E/2$) photons to excite the same fluorophore.

Since the time-varying n -photon fluorescence, given by Equation 1.36, is a nonlinear

function of the spatial and the temporal distributions of the intensity of excitation photons, it is clear that the probability of fluorescence is greatly increased if photons are 1) spatially close together and 2) there is a high photon flux in the excitation volume. Using the paraxial form of the normalized intensity PSF, the intensity at the geometric focal point for a diffraction limited lens is (Diaspro, 2002):

$$I(t) = I_0(t) \int d\vec{r} S(\vec{r}) = \frac{\pi NA^2}{hc\lambda} P(t) \quad (1.44)$$

where P is the power of the excitation source. Since the TPEF intensity is proportional to the square of $I(t)$, we have

$$F(t) \propto \sigma_2 P(t)^2 \left[\frac{\pi(NA)^2}{hc\lambda} \right]^2 \quad (1.45)$$

From this proportionality, it is clear that the probability of two-photon fluorescence is greatly influenced by the excitation power. Therefore, pulsed lasers are used for TPLSM (and other nonlinear microscopy) to maximize the peak power. The power of a pulsed laser with average power P_{avg} , pulse width τ_p , and repetition frequency f_p is given by

$$P(t) = \begin{cases} \frac{P_{avg}}{\tau_p f_p} & \text{for } 0 < t < \tau_p \\ 0 & \text{for } \tau_p < t < \frac{1}{f_p} \end{cases} \quad (1.46)$$

Using Equation 1.46, an expression for the time-averaged fluorescence signal over T =one laser repetition period ($1/f_p$) can be found:

$$\langle F(t) \rangle \propto \sigma_2 \left[\frac{\pi(NA)^2}{hc\lambda} \right]^2 \frac{1}{T} \int_0^T P(t)^2 dt = \sigma_2 \left[\frac{\pi(NA)^2}{hc\lambda} \right]^2 \frac{P_{avg}^2}{\tau_p f_p} \quad (1.47)$$

This leads directly to the probability of two-photon absorption for many repetition periods given by (Denk et al., 1990) for the optics and lasers used for TPLSM:

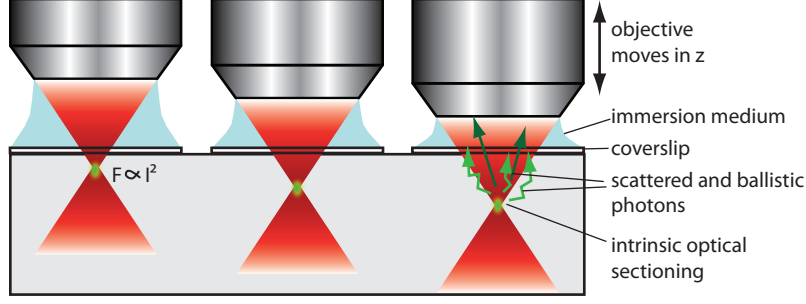


Figure 1.19: Two-photon fluorescence excitation in scattering tissue has intrinsic optical sectioning because the fluorescence only occurs at the focus of the excitation beam. Both scattered and ballistic photons contribute to the detected fluorescence signal.

$$n_a \propto \frac{\sigma_2 P_{ave}^2}{\tau_p f_p^2} \left(\frac{\pi (NA)^2}{hc\lambda} \right)^2 \quad (1.48)$$

The strong dependence on NA requires the use of high-NA objective lenses for best performance, coupled with high-powered, short-pulse laser sources.

Since excitation scales nonlinearly with laser power, fluorescence is significantly more likely to occur at the focus of the laser beam. Therefore, images obtained with a two-photon microscope are optically sectioned without needing to exclude any emission light, allowing very efficient fluorescence collection. Even emission light that has been scattered can be assumed to originate from the focal spot. This concept is illustrated in Figure 1.19. Note that, although the figure depicts only scattered and ballistic fluorescence photons that are within the detection cone of the objective, the fluorescence emits isotropically.

The real advance of TPLSM over earlier techniques is its ability to excite fluorescence in highly scattering tissues to typical depths of 200-600 microns (Helmchen and Denk, 2005; McCaslin et al., 2011) and, by using specialized excitation sources, to depths greater than 1 mm (Theer et al., 2003; Kobat et al., 2011). Since the wavelength of light is inversely proportional to its energy, the wavelengths used for TPEF scale up by 2 from those used for single-photon excitation. These longer wavelengths used to excite fluorescence can penetrate further into turbid media because they have longer scattering lengths than light used for

single photon absorption.

The penetration depth is ultimately limited by the ability of the excitation laser to form a focus in a sample (Theer and Denk, 2006). Since longer excitation wavelengths also correspond to lower energy, TPEF reduces photodamage to tissue outside the focal plane. Reduced photodamage is another advantage of TPLSM over confocal microscopy, which is more susceptible to damage because excitation occurs above and below the focal spot.

Some of the advantages and requirements for using TPLSM over confocal microscopy for deep tissue biological imaging are summarized below:

- Intrinsic optical sectioning due to small volume of signal generation
- Increased depth penetration because of long wavelength excitation sources
- Simplified detection optics; better SNR than confocal
- Reduced photodamage of live cells and tissues
- Most fluorophores have broader TPE bands, allowing the use of a single excitation wavelength to activate multiple fluorophores
- Large Stokes shift means that multiple dyes can be used with simpler filter selection

These advantages are gained at the cost of reduced resolution due to the longer wavelength excitation light in TPLSM. Resolution can be improved by using a confocal pinhole and descanned detection, though this in turn reduces available signal. Additionally, the high cost of pulsed lasers required for TPLSM is a drawback compared to confocal.

Second harmonic generation microscopy

SHG microscopy images of biological tissues were first demonstrated several years before TPLSM microscopy was developed (Freund and Deutsch, 1986). The signal measured is a second harmonic of the input light, meaning that it has exactly double the frequency (half

the wavelength) of the light entering the sample. Like two-photon absorption, SHG is a nonlinear effect that depends on the square of the intensity of the input beam, and therefore it provides inherent optical sectioning.

The SHG signal intensity scales with the peak power of a pulsed laser, given by the average power P_{avg} divided by the pulse repetition frequency f_p and the area of the focused spot, a

$$SHG_{sig} \propto \left(\frac{P_{avg}}{f_p a} \right)^2 \tau [\chi^{(2)}]^2 a \quad (1.49)$$

Like two-photon excited fluorescence, the SHG signal scales with the square of the incident laser power. The signal is also proportional to the square of the second-order nonlinear susceptibility of the structure, $\chi^{(2)}$, which is wavelength-independent except for when the incident wavelength is at a resonance frequency of the molecule. SHG signal is higher on resonance, but it is more similar to fluorescence, which is also a resonant process. As an example, collagen is a structure that exhibits strong SHG that is also fluorescent. It has an SHG peak near its fluorescence peak. $\chi^{(2)}$ is a bulk property measured experimentally. The molecular basis of the susceptibility (and therefore of SHG contrast) is called the hyperpolarizability β , and is related to $\chi^{(2)}$ by

$$\chi^{(2)} = S \langle \beta \rangle \quad (1.50)$$

where S is the density of molecules contributing to the signal. The brackets indicate averaging over the directions that the molecules are oriented. Therefore, randomly oriented molecules produce a vanishing term, as do molecules that are symmetric. The orientational alignment of molecules is crucial for SHG signal to occur, and the generation is a result of combined contribution from all aligned molecules. The importance of the collective properties of the materials is reflected in the quadratic dependence of SHG signal on the concentration contributing molecules, S (Campagnola, 2008).

SHG imaging can be readily combined with TPLSM imaging since both technologies can use the same laser source, detection geometry, and means of optical sectioning (Moreaux

et al., 2000). SHG can be detected in a reflection geometry because 1) forward-propagating photons are scattered within tissue and can come back to the detector 2) small structures have a lot of back-propagated SHG.

Dyes or contrast agents can be used to enhance signal from SHG, and have been used for imaging membrane potential in neurons (Nemet et al., 2004; Nuriya et al., 2006). Membrane imaging using SHG instead of fluorescence is advantageous since there is little background SHG signal from non-membrane structures. It is also possible to add SHG contrast using crystalline nanoparticles (Hsieh et al., 2010; Pantazis et al., 2010) for in vivo imaging applications. Because signal from these nanoparticles does not arise from absorption, they do not photobleach or saturate with increasing laser intensity.

1.3 Applications of nonlinear microscopy

1.3.1 Imaging in research

Nonlinear microscopy, in particular two-photon fluorescence microscopy, can be used in research virtually everywhere confocal microscopy is used. However, its utility is especially valuable for in vivo imaging for all the reasons cited in section 1.2.3. Because of these advantages, TPLSM has been used to track the progression of diseases, such as cancer, in rodent models using chronic windows (Brown et al., 2001; Jain et al., 2002). Typically, long term tumor growth studies are performed on many mice, and tumors are examined using histology at various points in the study. The number of mice required for such a study is quite large because the progression of a tumor cannot be tracked in a single mouse. Using a chronic window, TPLSM ‘intravital imaging’ can be used to track the growth of vascular networks and lymphatic vessels, monitor cell adhesion and migration, show tissue viability and morphological changes, and provide insight into gene expression and metabolic markers simultaneously, in a single mouse over the course of the tumor progression in the mouse. This ability reduces the number of animals needed for statistically relevant results. Additionally, the use of such a window allows direct measurements of the efficacy of drug delivery strategies, as well as the efficacy of drugs themselves. Chronic imaging studies with multiphoton microscopy have also been done to study spinal cord injury (Farrar et al., 2012), wound healing (Deka et al., 2013), and lymphocyte tracking (Miller et al., 2002, 2003; Cahalan and Parker, 2008).

Besides chronic imaging in rodents, nonlinear microscopy has become an important tool in embryology, since it permits repeat imaging of developing embryos without inducing photodamage (Squirrell et al., 1999). Embryos are very sensitive to light, and so imaging with confocal microscopy can cause abnormal development or no development at all past the imaging studies. Obviously, such an experimental influence is undesirable since it makes it

difficult to draw developmental conclusions. Aside from the reduced photodamage aspect, nonlinear microscopy is well-suited for imaging embryos because it can exploit contrast from TPEF, as well as from SHG, THG, and the nonlinear effects coherent anti-Stokes Raman scattering (CARS) and stimulated Raman scattering (SRS) (Olivier et al., 2010; Supatto et al., 2011). A real advantage of using such nonlinear contrast mechanisms is that they do not require exogenous labels, and can give additional information on the chemical makeup of the sample.

Nonlinear microscopy has also become useful for ‘interventional’ microscopy approaches, meaning that it is used to impart some change in the sample rather than to form an image. The laser beam is held at a particular location in the sample until the desired event occurs. Examples of such approaches include photolysis of caged compounds, acute injury by ablation, and the transfection of single cells by causing small holes in membranes (Lei et al., 2008). By using nonlinear mechanisms and laser sources to do this, the specificity is very good and general injury to surrounding regions is reduced.

1.3.2 Clinical relevance

Nonlinear microscopy can provide detailed images of living tissues using only endogenous sources of contrast (Zipfel et al., 2003). This application has prompted work to characterize the morphology of many tissues using TPLSM, since the images can be as informative as histology and can be acquired in a fraction of the time. Chapter 2 of this thesis is focused on the information that can be gained from tissues using TPLSM. The widespread use of nonlinear microscopy for this application has prompted discussion on the benefits of nonlinear microscopy in the clinic. Possible target applications include skin imaging, intra- or post-operative assessment of tumor margins in vivo, endoscopic applications, or for ‘bedside’ histological examination. The ability to rapidly evaluate fresh tissue biopsies for neoplastic changes at the bedside could reduce the cost and time associated with conventional histology,

while also providing immediate diagnoses.

Currently, nonlinear imaging in human subjects is not FDA approved, due primarily the unknown effect of light induced DNA damage in biological tissues. However, studies have shown that at low laser intensities, mutations are rare and therefore the future use of two-photon microscopes for human diagnostics is feasible (Dela Cruz et al., 2010). There have already been several demonstrations of its usefulness for diagnosis in vivo in human skin (Konig and Riemann, 2003). For the case of GI diseases, screening and diagnosis generally requires endoscopy, which often require lengthy procedure preparation and anesthesia. The ability to quickly determine whether suspicious lesions are malignant or benign could shorten or alter the course of the diagnostic procedure, as well as reduce the need for repeat endoscopic examination if disease is found.

Technical challenges for clinical translation include the determination of safe levels of laser excitation and how to optimize collection of relatively weak optical signals. For endoscopic applications, the miniturization of devices is an active research area (Jung et al., 2008; Chia et al., 2010; Saar et al., 2011; Rivera et al., 2012). Although feasibility studies are currently in the early stages, there are several research groups and small companies actively pursuing this aim, indicating that there is current interest and an active push for clinical translation.

1.3.3 Neuroscience

In neuroscience, the use of TPLSM for in vivo imaging and for the imaging of thick brain tissue in slices is ubiquitous. Deep tissue imaging capability coupled with high spatial resolution make TPLSM an invaluable tool for investigations of the living brain. Imaging in the intact, living rodent brain preserves the vascular structure, circulation, and the neural connections, allowing direct measurement of cellular morphology and interactions, calcium dynamics, and the mechanisms of blood flow (Svoboda and Yasuda, 2006; Hillman et al.,

Table 1.1: Selected fluorescent labels used for TPLSM in the brain

Fluorophore	Excitation	Emission	Application	Reference
Fluorescein (FITC-dx)	780 nm	515 nm	Vascular tracer	(Kleinfeld et al., 1998)
Texas Dextran Red (TDR)	850 nm	615 nm	Vascular tracer	(Chaigneau et al., 2007)
Alexa Fluor 633	810 nm	647 nm	Labels the elastin in arterial walls	(Shen et al., 2012)
Oregon green 488 BAPTA-1	810 nm	525 nm	Imaging Ca^{2+} signals among cell populations in cortex	(Kerr et al., 2005)
GCaMP	930 nm	520 nm	Genetically encoded Ca^{2+} indicator	(Tian et al., 2009a)
Sulforhodamine 101	830 nm	590 nm	Labels astrocytes	(McCaslin et al., 2010)

2007). Further, all these parameters can be measured in both normal and diseased states to better understand the underlying features of neural pathologies.

The maximum penetration depth of TPLSM is almost large enough to image throughout the thickness of the rodent neocortex, the outer layer of the cerebral cortex (see Figure 1.20). This region of the brain is interesting to study since it is thought to control mammalian cognitive functions including memory and voluntary movement, and neurons are thought to be locally interacting (Belgard et al., 2011). The experimental setup for imaging brain activity with TPLSM using a cranial window is shown in Figure 1.20A-B.

Fluorescent labels. Fluorophores used in conjunction with multiphoton microscopy to study the brain include vascular tracers, cell-specific dyes, and activity dependent indicators. Fluorophores designed for brain research with TPLSM are increasingly available, and a few such dyes are listed in Table 1.1. Vascular tracers, typically fluorescent molecules conjugated to large dextran molecules that do not cross the blood brain barrier, label blood plasma and allow dynamic measurements of vessel diameter and red blood cell speed (Kle-

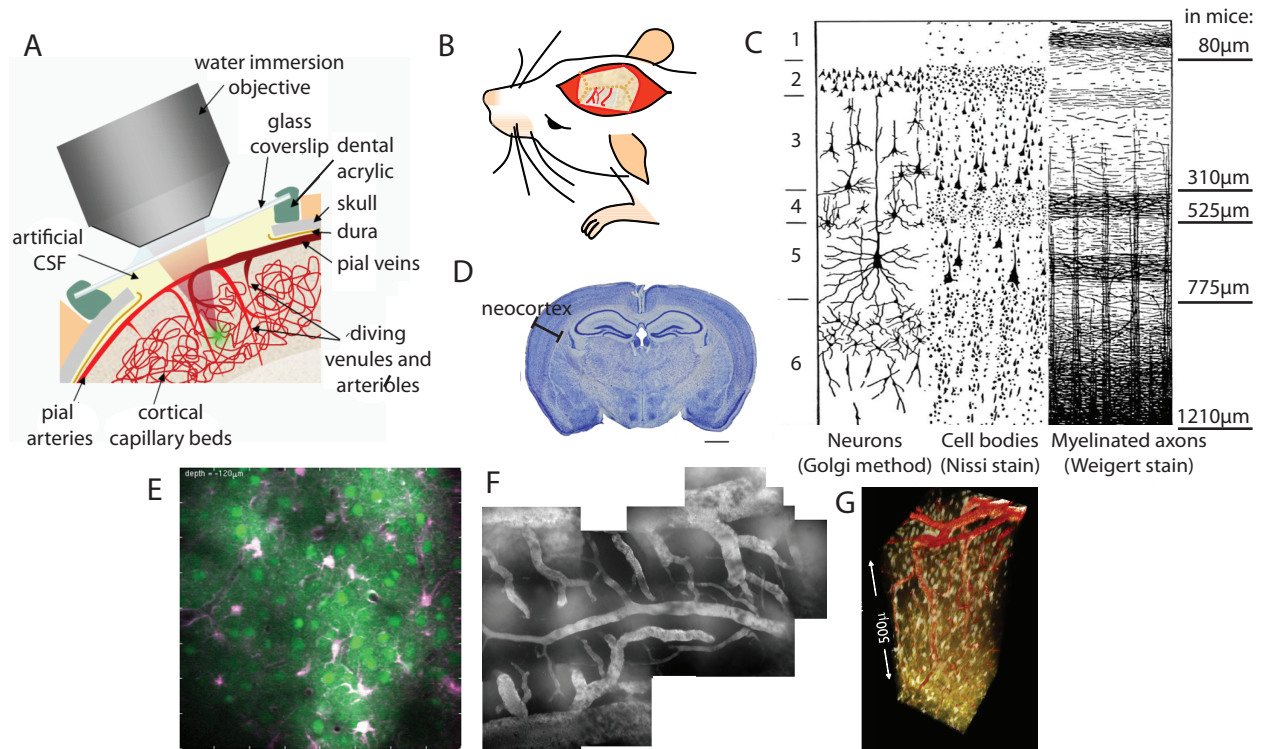


Figure 1.20: Two-photon microscopy in neuroscience. A-B. Experimental setup for in vivo microscopic imaging of the brain using a cranial window, from (Hillman et al., 2007). In A, large blood vessels are near the surface of the brain, and smaller vessels dive down to a dense capillary network. C. Drawings from Ramon y Cajal identifying the layered structure of the brain in human brain tissue (Ramon y Cajal, 1899). The thickness of each layer is given for mice (Defelipe, 2011). Note that the relative thickness of each layer for mouse cortex is not the same as for human tissue. D. Cross-sectional histology of a whole mouse brain shows the location and thickness of the neocortex, the region of the brain that is usually studied with TPLSM. Scale, 1 mm; from (Defelipe, 2011). E-G. Images acquired in living brain using TPLSM. The green Oregon green dye labels neuronal cell bodies and astrocytes are pink from SR101 in E. FITC-dx allows vascular imaging in F, and a 3D rendering of vessels labeled with FITC-dx and astrocytes labeled with SR101 is shown in G. G from (McCaslin et al., 2010).

infeld et al., 1998). FITC-dx is used for vascular labeling in Figure 1.20F, and is used for studies presented in Chapter 3. Cell-specific labels, like SR101 which targets astrocytes (1.20E,G), can be used to study complex relationships between different cell types. Calcium sensitive dyes, like Oregon green BAPTA-1 (Figure 1.20E) can be used to optically sense calcium transients associated with action potentials in neurons. Recent advances in genetically encoded calcium indicators have led to the ability to produce mice with neurons of any particular type that can express changes in fluorescence when are activated (Tian et al., 2009b; Akerboom et al., 2012), and have are used in Chapter 3.

High-speed imaging is needed to capture dynamic events such as intracellular calcium influxes, changes in vessel diameter, and blood flow. In addition, since intracellular interactions rarely occur in one plane, acquisition of 3D volumes is necessary to truly resolve dynamic neural activity. The push for faster 3D imaging speeds to study questions in neuroscience was a primary motivation for the work presented in Chapter 3

Chapter 2

Hyperspectral nonlinear microscopy

For most fluorescence microscopy techniques, contrast comes from exogenous sources, and autofluorescence must be minimized. However, removing intrinsic signals can throw away valuable, readily available information about the chemical makeup of the specimen, without adding large fluorescent indicators or disrupting homeostasis. Furthermore, the use of intrinsic contrast for microscopic imaging allows the visualization of tissue morphology, spatially-localized metabolic activity, and changes associated with disease states, which is exactly what is required for many clinically relevant *in vivo* applications. Moreover, the use of exogenous dyes is often limited or impractical for such clinical applications, due to challenges for dye delivery and regulatory issues.

Nonlinear microscopy is an ideal tool for studying intrinsic fluorescence and SHG in fresh tissues because it can excite endogenous fluorophores in the ultraviolet-to-blue range (where their cross-section is often highest), using lower energy light than conventional fluorescence techniques. Numerous studies have used nonlinear microscopy with endogenous fluorescence for morphological examination of biological tissues, including skin, lung, bladder, gastric, and brain (Zipfel et al., 2003; Paoli et al., 2008; Pavlova et al., 2010; Mukherjee et al., 2009; Rogart et al., 2008). However, these studies do not carefully and quantitatively examine the molecular contributors to the signal.

This chapter is focused on the establishment of hyperspectral two-photon and second harmonic generation microscopy as a tool for imaging of intact fresh or living tissue, without the need for histological processing, fixing, slicing or staining. By measuring spectrally-resolved fluorescence signal from multiple excitation wavelengths, rich ‘hyperspectral’ data sets containing morphological and biochemical information about tissues can be acquired. Linear unmixing can be used on these spectroscopic data sets for image segmentation and analysis of the origin of fluorescence or SHG. This chapter is organized into four sections:

Section 2.1 provides information on the most common molecules thought to contribute to autofluorescence and SHG imaging of biological tissues. These fluorescent biomolecules are discussed in the context of cell or tissue functionality that can be inferred from their presence. Measurable changes in intrinsic contrast in diseased states are also discussed from an imaging perspective.

In **Section 2.2**, technical aspects and challenges associated with spectral imaging are discussed, which motivated the development of our hyperspectral imaging microscope. The design of the multiphoton microscope used throughout this thesis is given with emphasis on design choices that make our instrument well-suited for in vivo imaging. Finally, software requirements for hyperspectral imaging and resulting data sets are mentioned.

Section 2.3 demonstrates the capability of hyperspectral two-photon microscopy for imaging freshly excised tissues with minimum sample preparation. Linear unmixing strategies for data analysis are explained.

Section 2.4 is the detailed study of healthy and diseased lower gastrointestinal (GI) tissues using hyperspectral microscopy. Our technique is used to visualize morphology of fresh tissue, characterize the intrinsic contrast within the gastric mucosa, and determine the spectral signatures of the major tissue components that make up GI tissues.

2.1 Intrinsic contrast imaging.

In this section, sources of endogenous fluorescence and harmonic generation, along with changes in the distribution of these biomarkers that can be indicative of disease states, are described.

2.1.1 Endogenous fluorescence

Many naturally occurring biomolecules exhibit fluorescence, including amino acids, the structural proteins collagen and elastin, enzymes and co-enzymes, vitamins, lipids, and porphyrins (Ramanujam, 2000). Endogenous fluorophores excite with ultraviolet (UV) and visible light, and as a group have a broad emission range from the UV (amino acids) to red (lipids and porphyrins). Table 2.1 provides excitation and emission information for several of the brightest common endogenous fluorophores that are found in bulk tissues.

Table 2.1: One and two-photon fluorescence excitation and emission properties for endogenous fluorophores. 1PE, 1 photon excitation; 2PE, 2 photon excitation

Fluorophore	Excitation range (nm)	Emission maxima (nm)	Reference
NADH	700-780 (2PE)	460	(Huang et al., 2002)
FAD	700-950 (2PE)	530	(Huang et al., 2002)
Collagen	750-850 770 (2PE peak) 810 (SHG peak)	470	(Zoumi et al., 2002; Chen et al., 2009)
Elastin	750-850 <750 (2PE peak) 290,325 (1PE peak)	460,340,400	(Chen et al., 2009; Ramanujam, 2000)
Phospholipids	436 (1PE peak)	540, 690	(Ramanujam, 2000)
Porphyrins	400-450 (1PE)	630, 690	(Ramanujam, 2000)
Keratin	700-900 <700 (2PE peak)	450	(Pena et al., 2005)

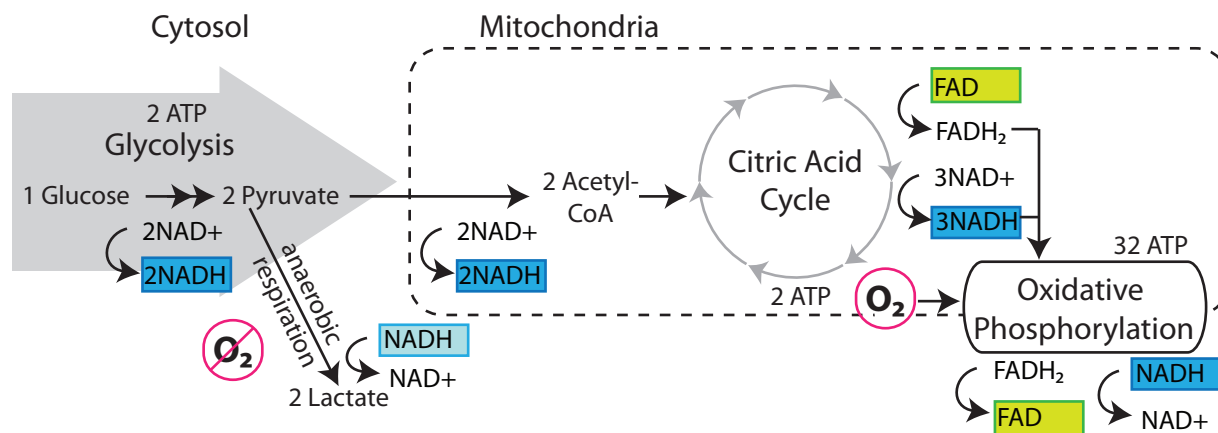


Figure 2.1: Diagram showing cellular metabolic pathways glycolysis, the citric acid cycle, and oxidative phosphorylation. Fluorescent coenzymes NADH and FAD are highlighted in blue and green, respectively. The highlight color choice is deliberate; fluorescence from NADH is blue-shifted with respect to fluorescence from FAD. Since FAD is only produced during oxidative respiration but NADH is active in both aerobic and anaerobic pathways, the relative fluorescent signal from these species can be used to measure the favored metabolic pathway of a cell or tissue.

NADH and FAD. Nicotinamide adenine dinucleotide is a coenzyme that acts as an electron carrier for oxidation and reduction reactions in glycolysis and oxidative cellular respiration pathways. It therefore exists in both an oxidized (NAD⁺) and a reduced (NADH) form. Since NADH is fluorescent but NAD⁺ is not, it is possible to monitor metabolic activity in cells based on the fluorescence of NADH (Chance, 1954). Similarly, flavin adenine nucleotide is an electron carrying coenzyme that is fluorescent in its oxidized form (FAD) but not in its reduced form (FADH₂). The redox ratio is the ratio of fluorescence from FAD to NADH, and can provide a better indicator of metabolic activity (Chance et al., 1979).

Figure 2.1 shows a schematic representation of the coenzyme involvement in metabolism. During glycolysis, NADH is generated in the cytoplasm. When oxygen is available, pyruvate is further oxidized in the mitochondria for maximal energy production. NADH is generated and then used to maintain the electric gradient in the electron transport chain. Under hypoxic conditions, the electron transport chain is put on hold because there is insufficient oxygen to accept electrons. The buildup of NADH inhibits the citric acid cycle, leading to

lactic acid fermentation, in which pyruvate is converted to lactate in a reaction that converts NADH back to NAD⁺. The regeneration of NAD⁺ allows glycolysis to continue in the absence of oxygen (Berg et al., 2007). This accumulation of NADH levels during anaerobic respiration was first observed using fluorescence spectroscopy in 1962 (Chance et al., 1962). A shift to anaerobic respiration even in the presence of oxygen is characteristic of cancer.

Collagen and Elastin. Collagen and elastin are structural proteins that are found in connective tissues. Collagen is a major component of the extracellular matrix, and provides support to link cells. Collagen is an intrinsically fluorescent molecule; however, SHG signal dominates under nonlinear excitation. Images with SHG from collagen provide a wealth of structural information about the extracellular matrix, and structural membranes separating tissue types (Williams et al., 2005). Elastin is a connective tissue with elastic properties, which allows tissues (especially skin) to stretch and return to their original shape. Unlike collagen, elastin does not typically exhibit SHG and its signal is derived from autofluorescence (Zoumi et al., 2004).

Porphyrins. Porphyrins are one of the few sources of endogenous fluorescence that exhibit fluorescence most strongly in the red. Porphyrins are important in the synthesis of heme-containing enzymes (Ramanujam, 2000), which are found in blood. Highly vascularized tissues exhibit red fluorescence, along with signal from elastin which is found in a subset of vascular walls.

2.1.2 Changes in intrinsic contrast through the onset of cancer

Observable changes undergone by tissues during the onset of disease can be used in research to help elucidate mechanisms that are disrupted during disease progression, and to track the efficacy of potential treatments. This section will describe some changes associated with cancer and pre-cancer that can be detected using imaging techniques.

A cell becomes cancerous through mutation and deregulation of normal signaling pathways. Changes in tissues containing cancerous cells manifest in several measurable ways. Some of these changes in tissues associated with cancer or pre-cancer are

- Morphological changes, including unregulated cell growth
- Shift from normal metabolic pathways toward anaerobic respiration
- Restructuring of the extracellular matrix
- Angiogenesis and lymphangiogenesis

A tumor is made up of cancerous cells, that are able to survive and proliferate because of the normal and mutated cells surrounding it that actively support the tumor and its capacity for invasion and metastasis (Fukumura and Jain, 2007). This support network, made up of endothelial cells, fibroblasts, myofibroblasts, inflammatory cells, pericytes, and altered extracellular matrix, is collectively called the tumor microenvironment (Hu and Polyak, 2008; Polyak et al., 2009; Weinberg, 2008). Cancer associated fibroblasts have been shown to enhance angiogenesis by secreting growth factors and cytokines. This recruitment is aided by the release of vascular endothelial growth factors (VEGFs) and a number of other factors (Weinberg, 2006). Similarly, lymphangiogenesis (i.e., the growth of the lymphatic vascular network) is increased in tumors by the activation of homologous VEGFs. Other changes in the microenvironment, such as hypoxia or acidosis, can lead to cell recruitment (for example, for fibroblast proliferation and extracellular matrix remodeling) in the tumor. Because these changes in the tumor microenvironment are integrally related to the proliferation of tumors themselves, they can be used as markers of cancer progression and its response to therapies.

From an imaging perspective, many of the changes mentioned above are visible using endogenous sources. For example, the restructuring of the extracellular matrix is associated with changes in the distribution of fibrillar collagen, which is distinctly visible using SHG microscopy. (Brown et al., 2003) were able to track the changes in structural collagen during

tumor progression using SHG. This study was instrumental in basic understanding of tumor growth, but also was the first to demonstrate that such endogenous sources of contrast could provide clinically relevant measures.

In (Skala et al., 2007), the authors used multiphoton microscopy and fluorescence lifetime imaging to observe and quantify the metabolic changes associated with cancer. Again, the study is focused on using only endogenous molecules to provide an analytical measure of the disease state of tissues. The fluorescence from NADH and FAD was used to quantify the progression of cancer in vivo using a cheek pouch model for oral cancer in hamsters. This study showed that the nuclear to cytoplasmic ratio and ratio of fluorescence of FAD to that of NADH varied spatially only in normal tissues, which indicates that the absence of these features could be used for identifying abnormal metabolic activity in precancers. Although the shift towards glycolytic metabolism in some cancers was already known, the methods in this paper could be clinically relevant, particularly if applied to fast bedside diagnostic applications.

2.2 Hyperspectral imaging system

One way to extract more information from images of endogenous contrast is to use spectroscopic imaging. In this section, techniques for spectral imaging with microscopic resolution are discussed, including spectral imaging strategies that target excitation or emission data. The description of our microscope, which was used for imaging throughout this thesis, is given in the context of its use for hyperspectral microscopy.

2.2.1 Considerations for spectral imaging

The majority of studies that use spectral imaging combined with nonlinear microscopy do so by using a single wavelength to excite fluorescence combined with multiple spectrally resolved detection channels (Lansford et al., 2001; Laiho et al., 2005; Palero et al., 2007). The main difficulty with such imaging schemes lies in the detection: fluorescence signals are relatively weak and only become more difficult to detect after splitting them into their wavelength components. Emission light can be spectrally resolved using spectral filters or gratings in combination with sensitive detectors. Spectral data sets can be acquired either by separating the emission light as it is acquired, or by acquiring a sequence of images and using gratings or filter sets to detect a small spectral range for each image in the sequence.

An alternate approach used in this chapter obtains spectral images by scanning the excitation wavelength and acquiring image sequences (Dickinson et al., 2003; Radosevich et al., 2008). Through these excitation sweeps, the excitation spectrum of a dye is acquired, which is as descriptive of a fluorophore as its emission spectrum. As tunable wavelength laser sources are common, most nonlinear microscopic systems are capable of implementing this technique with no additional required hardware. A drawback of both emission- or excitation-based spectral imaging strategies is the long acquisition time typically needed to build up a spectral data set.

An advantage to using excitation-based spectral imaging in biological tissues is the

reduced dependence on imaging depth. Absorption properties in tissues are highly dependent on wavelength. Therefore, when collecting emission spectra in biological tissues at depth, bluer fluorescence components will be absorbed more than red, leading to emission intensity data that is skewed toward the red side of the visible spectrum. Such data is difficult to correlate with known emission data, and also depends on sample properties and imaging depth. Another advantage for excitation-based spectral imaging is that all fluorescence emission is collected to produce an excitation spectrum, unlike emission spectra which need to use long integration times to get enough photons for strong signals in each desired detection band. However, if there is sufficient signal, the combination of excitation- and emission-based spectral imaging can be even more powerful.

2.2.2 Instrument design for hyperspectral two-photon microscopy

This section describes the instrument design and features of our custom built hyperspectral two-photon microscope that make it an effective tool for in vivo studies. Key features include a pulsed source with tunable excitation, large field of view imaging, spectrally-resolved detection for improved spectral analytics, and a large area between the objective and stage for animal positioning.

Excitation source. A Ti:Sapphire pulsed laser (Mai Tai XF-1, Spectra Physics) provides the excitation for our microscope. The output wavelength can be tuned between 710 nm and 920 nm by turning a diffraction grating to allow only the desired wavelength band to enter the lasing cavity. Tuning the output wavelength of the laser is fully automated and can be controlled from a computer using serial port communication. This capability allows versatile imaging with excitation wavelengths that can efficiently excite a wide range of fluorophores. Short output pulses (<70 fs) are generated at repetition rate of 80 MHz with an average power close to 1W, providing high peak power for efficient two-photon excitation. To control the laser power output, we use a half wave plate on a rotation mount in combination

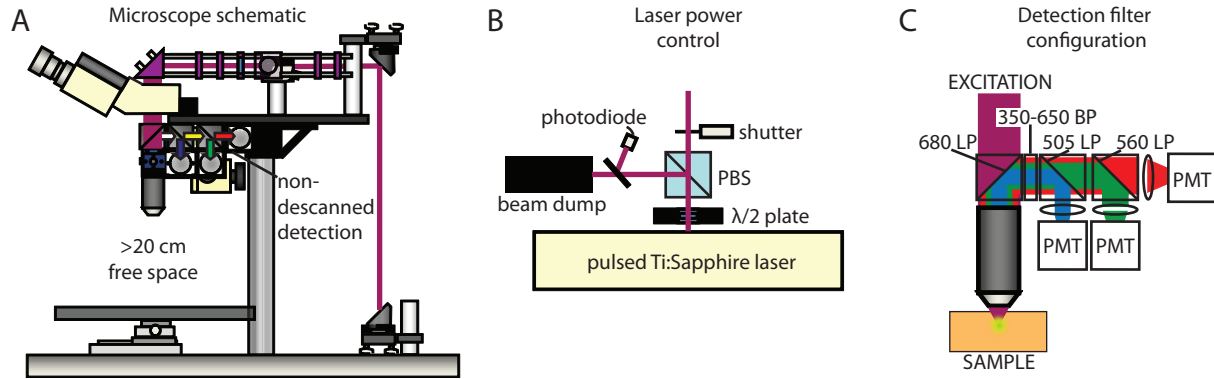


Figure 2.2: Custom built microscope design for in vivo two-photon microscopy. A. Schematic highlighting available space for animal positioning beneath the objective and efficient fluorescence collection using detectors positioned immediately behind the objective lens. B. Power control of the excitation laser. A half-wave ($\lambda/2$) plate on a motorized rotation stage rotates the linear polarization of the laser to vary the percentage of total laser power that can pass through the polarizing beam splitter cube (PBS). C. Three channel detection channel configuration. Filters can be easily swapped for custom detection bands. LP, long-pass filter; BP, band-pass filter; PMT, photomultiplier tube.

with a polarizing beamsplitter (PBS) cube (Figure 2.2B). The power is monitored with a photodiode that measures the intensity of the unused arm of the PBS cube. Alternate power control systems (like using a Pockels cell) introduce more glass into the system, which causes dispersion that broadens the temporal profile of the pulse. This simple power configuration minimizes the overall amount of glass in the beampath, in order to better maintain the ultra-short pulse.

Imaging in a sample. The laser beam is expanded using a lens telescope and then directed towards two galvanometric mirrors from Cambridge Technologies that are used to steer the beam in an x-y raster scan. The galvo mirrors have maximum scan rates of 3500 lines/s for drive amplitudes typically used for imaging ($\sim 2V$, corresponding to a 500 μm square field of view). Larger drive amplitudes increase the deviation angle of the mirrors, and therefore the field of view in the sample, but decrease the maximum line rate of the scan mirrors (Burgess, 2011, p.44). The line rate of the scanner is a determining factor for imaging frame rate. For example, if 200 lines are included in one image frame, the maximum achievable frame rate

is $17.5 \text{ frames/s} \left(\frac{3500 \text{ lines/s}}{200 \text{ lines/frame}} \right)$. Further discussion on factors that influence imaging speed is included in Section 3.4.1.

Light is focused with an Olympus XLUMPlanFl 20x/0.95W objective mounted on a motorized z-translation stage (M-112.1DG, PI) that can be positioned in steps of 50 nm for accurate axial scanning. The objective lens is specially designed for nonlinear scanning microscopy, with features including high NA, correction for chromatic aberration for a wide range of wavelengths, and correction for aberrations induced by angled entry of the beam into the objective for scanning purposes. Lateral translation is achieved by moving the sample stage using two linear translation stages for the x and y directions (Newport, MFA-CC). A key design element for in vivo imaging is the upright configuration with ~ 20 cm of free space between the objective and the translation stage to allow flexible animal positioning (Figure 2.2A).

Fluorescence collection. Three spectrally resolved detection channels are located immediately behind the objective for efficient fluorescence collection. The detection channels use photomultiplier tubes (PMTs) from Hamamatsu (R3896) to convert fluorescence signal to measurable current. The configuration of the detectors is detailed in Figure 2.2. A dichroic filter (Semrock FF685-Di02-25x36) is used to separate the fluorescence from the excitation light, and a bandpass clean-up filter (transmits wavelengths 350-650 nm; Semrock FF01-680/SP) is used before the detectors to minimize the bleed-through from the excitation light. Since the excitation light is orders of magnitude more intense than the fluorescence, the quality of these filters is very important. Two more long pass dichroic mirrors with cutoff wavelengths of 505 nm (Semrock FF506-Di03-25x36) and 560 nm (Semrock FF560-Di01-25x36) split the fluorescence emission into blue and yellow, then green and red, respectively. The resulting detection bands from these filter choices are referred to as blue (350-505 nm), green (505-560 nm), and red (560-650 nm) throughout this thesis. The spectral response of the PMT detectors is fairly flat over our detection range, though the sen-

sitivity is slightly decreased in the red channel. Achromat lenses with anti-reflection coating for visible wavelengths focus emission light into the active area of the PMTs for maximum collection efficiency.

The specific bands were chosen to maximize performance for typical experiments. For example, the green channel could be used to measure signal from the calcium indicator Oregon green or vascular label FITC-dextran, while the red channel could be used for cell specific labeling with sulfarhodamine (see Section 1.3.3 for more information on this dye combination). A design feature of our detection configuration is that the filters can be swapped easily for others that could enable cleaner separation of fluorescence for other dye combinations. There is space for additional detectors if necessary, as well as a wide-field imaging port to enable camera imaging.

Image acquisition Current from each of the three PMTs is converted to a voltage and amplified using transimpedance amplifiers (TIAs) from Stanford Research Systems (Model SR570). The data from the three fluorescence channels is simultaneously acquired along with the scan position feedback signal using an analog input data acquisition card from National Instruments (PCI-6133). The maximum data acquisition rate of the card is 2.5 MHz, however the maximum data rate is ultimately limited by the bandwidth of the TIAs, which is 1 MHz. In the example above, a frame rate limited by the maximum scan speed of the galvanometer mirror was 17.5 frames/s, with 200 lines/frame. The number of lines/frame corresponds to y pixels, so the maximum number of x pixels we could acquire at this example frame rate is 285 pixels/line ($1 \text{ MS} \cdot \text{s}^{-1} / 17.5 \text{ frames} \cdot \text{s}^{-1} / 200 \text{ lines} \cdot \text{frame}^{-1}$). However, the fastest frame rates we typically use are acquired at 16.6 frames/s with 300×200 x and y pixels, at a rate of 1 MHz (limited by the TIA bandwidth).

The scan position feedback signal from the x-scanner is used to map the acquired fluorescence signal to its correct spatial position in an image. For basic visualization of acquired images, red-green-blue (RGB) merges are created using data from the three cor-

responding emission channels, with each channel scaled to its maximum after thresholding out the highest 0.06% of pixels. The threshold cutoff is somewhat arbitrary; its purpose is for best contrast for displaying images. The underlying voltages that are the basis for the signal remain unchanged.

Custom control software. Custom software, written as a MATLAB graphical user interface, controls the laser power and wavelength, as well as all translational motion, image acquisition, gain and amplifier settings, image display, and on line processing. The software ensures that fluorescence detection is properly synchronized with the mirror scan position, so that images can be reconstructed. Our control software allows great versatility in the types of images that can be acquired. We have defined several scan types, including long, high frame-rate time-series images to record functional data, volumetric stack scans which are series of images obtained at sequential axial positions, and wavelength scans, which are series that acquired with multiple excitation wavelengths.

For the acquisition of hyperspectral data sets, our software is configured to synchronously tune the excitation of the laser while recording three-color images in series. More information regarding the display and analysis of hyperspectral data sets is presented in subsequent sections.

Summary

The versatility afforded by this instrument is superior to commercial systems, since it is optimized for fast in vivo imaging. Many research groups that use advanced techniques in nonlinear microscopy must use home-built systems as well, since commercial systems cannot be modified to suit specific experimental needs. An advantage of our open platform is that additional components and features can be incorporated with relative ease. Several additions and modifications are described in Chapter 3.

2.3 Hyperspectral nonlinear imaging of freshly excised tissues

In this section, hyperspectral TPLSM is used to image a range of murine tissues either in vivo or perimortem. These samples include tissue from the kidney, spleen, heart, and pancreas. In all of these tissues, intrinsic contrast revealed detailed 3D morphology to depths of 200-500 μm without sectioning artifacts or the need for computational co-registration. Comparative histology of the same samples revealed good agreement between the structures visualized using the two techniques.

2.3.1 Morphological examination

Sample preparation. For images shown in this section, rodents were euthanized using an overdose injection of sodium pentobarbital (200 mg/kg, IP) after preceding in vivo imaging experiments. Imaging was performed on fresh tissue within 4 hours of dissection. Tissues were gently rinsed in saline, then immersed in saline on a slide, covered with a coverslip, and imaged using our hyperspectral microscope.

After imaging using TPLSM, samples were prepared for histology. First, they were submerged in vials containing a solution of 4% formalin for 24 hours, fixing the tissues. At the 24 hour time point, samples were rinsed with saline, then bathed in solutions with increasing ethanol concentrations (50, 70, 90, 100%) for 1-3 hours in each solution. Tissues cleared in this way could then be embedded in wax blocks. Tissues were embedded so that they were similarly oriented as they were during TPLSM imaging. Slices were obtained using a vibratome, then were placed on slides, stained using hematoxylin and eosin (H&E), and finally sealed using coverslips. H&E are general-purpose dyes that stain nuclei purple (hematoxylin) and the cytoplasm, muscle, and connective tissue pink (eosin). The process of fixing and histologically preparing samples takes 1-3 days, compared to minutes required

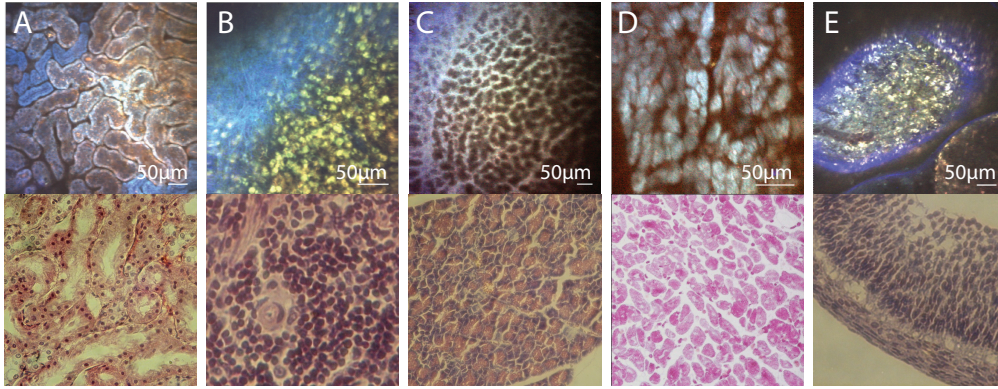


Figure 2.3: TPEF and SHG imaging of freshly excised tissues with intrinsic contrast (top row) with comparative histology (bottom row). A. Kidney B. Spleen C. Pancreas D. Heart E. Ovary

to image using nonlinear microscopy.

Intrinsic signal imaging. Images of intact tissues acquired by harnessing intrinsic contrast from second harmonic generation (SHG) as well as fluorescence from collagen, keratin, elastin, NADH, and FAD are shown in Figure 2.3. In 2.3A, whole kidneys were excised from rats and images shown are from a plane parallel to the surface of the kidney. The winding profiles of proximal and distal convoluted tubules are apparent in both the two-photon image and the classical histology. Densely packed white blood cells, which comprise the immunologic blood filter of the spleen, appear yellow in the TPEF image in 2.3B. Part of the collagenous capsule that contains the spleen appears blue. In the comparative histology, only lymphatic cells are visible; however, special staining could be used to visualize the collagen. The pancreas (2.3C) is divided into lobules bounded by autofluorescent connective tissue, shown in the TPEF image. Cardiac muscle cells are short and narrow, with diameters around 10-15 μm and lengths of 80-100 μm . The TPEF image (2.3D) shows a cross-sectional view of muscle fibers, which have rounded profiles similar to what can be seen in cross-sectional histology at 160x magnification, from (Ross and Pawlina, 2006). A TPEF image of a growing ovarian follicle found in the peripheral portion of the ovary is shown in 2.3E. The outer layer of connective tissue immediately surrounding the follicle appears blue and contains mainly

smooth muscle cells and bundles of collagen fibers, while the granulosa cells appear yellow. Comparative histology shows the outer layer of connective tissue and the granulosa cells.

Clearly, intrinsic contrast imaging with multiphoton microscopy is a powerful means of obtaining images of tissues with cellular resolution. Similar studies make a strong case that images like the ones shown in Figure 2.3 can be valuable in the clinic, particularly in settings where speed is important, such as during lesion excision or biopsy, or when there can be a benefit from visualizing key structures in 3D. The method also has the potential for clinical translation for endoscopic applications. In fact, confocal microendoscopy has already been proven useful and is currently being marketed for clinical use (Abrat and Masters, 2006; Becker et al., 2007).

2.3.2 Linear unmixing for fluorescence identification and image segmentation

The fluorescence contrast in Figure 2.3 can certainly be used to qualitatively compare the tissues to their histological counterparts. However, the true advantage of autofluorescence and SHG imaging is the biochemical information revealed in the signal. Through the use of hyperspectral imaging, we can get a better sense of the origin of the signals present in the images. Using that knowledge, we wanted to develop a technique that can reliably identify specific features in images, especially those features associated with morphological changes in disease states. In order to address this challenge, we can apply linear unmixing strategies to discriminate fluorophores based on their two-photon excitation properties.

Linear unmixing was applied to hyperspectral data sets containing a sequence of images acquired at multiple excitation wavelengths. The total fluorescence detected at each excitation wavelength is assumed to be a linear sum of the fluorescence emitted by each of n species and is given by Equation 2.1, where F_{mix} is the detected fluorescence, C is the concentration of that species, Q is its quantum efficiency, Φ is the collection efficiency of the

detector, and σ_2 is its two-photon absorption cross-section.

$$F_{mix} \approx K \sum_n \Phi_n Q_n \sigma_{2n} C_n \quad (2.1)$$

The constant K describes the excitation wavelength dependent multiplicative factor, which reproduced from Equations 1.36 and 1.48:

$$K(\lambda_{ex}) = \frac{P_{avg}^2 \pi^2 N A^4}{2 \tau_p f_p^2 h^2 c^2 \lambda_{ex}^2} \quad (2.2)$$

K is partially dependent on the arrangement of optical components within any two-photon instrument, where P_{avg} is the average laser power, τ_p is the pulse width of the laser, f_p is the laser pulse repetition rate, NA is the numerical aperture of the lens, h is Planck's constant, c is the speed of light, and λ_{ex} is the excitation wavelength. Signal from SHG adds to the total signal and is approximated by Equation 2.3 (Campagnola et al., 2001), where B represents the molecular hyperpolarizability, and S is the density of SHG activated molecules (see also 1.49).

$$SHG = \left(\frac{P^2}{\tau_p} \right) \sum_n B_n S_n^2 \quad (2.3)$$

As shown in Equations 2.1-2.3, in addition to the properties of the sample, variations in two-photon emission and second harmonic signal can result from wavelength-dependent changes in laser power and pulse width, dispersion through our system's optical elements, numerical aperture and the excitation wavelength itself. Since K does not depend on position or time, linear unmixing strategies are applied. The concentrations (C) of the fluorophores are calculated using a non-negative least squares fit.

In order to perform linear unmixing of hyperspectral data, the first step is to define basis spectra. We defined our basis spectra in one of two ways. 1) By choosing regions of interest in a data set and averaging the intensities of the pixels within the selection for each wavelength in the range. These basis spectra are specific to a given data set, and is used in

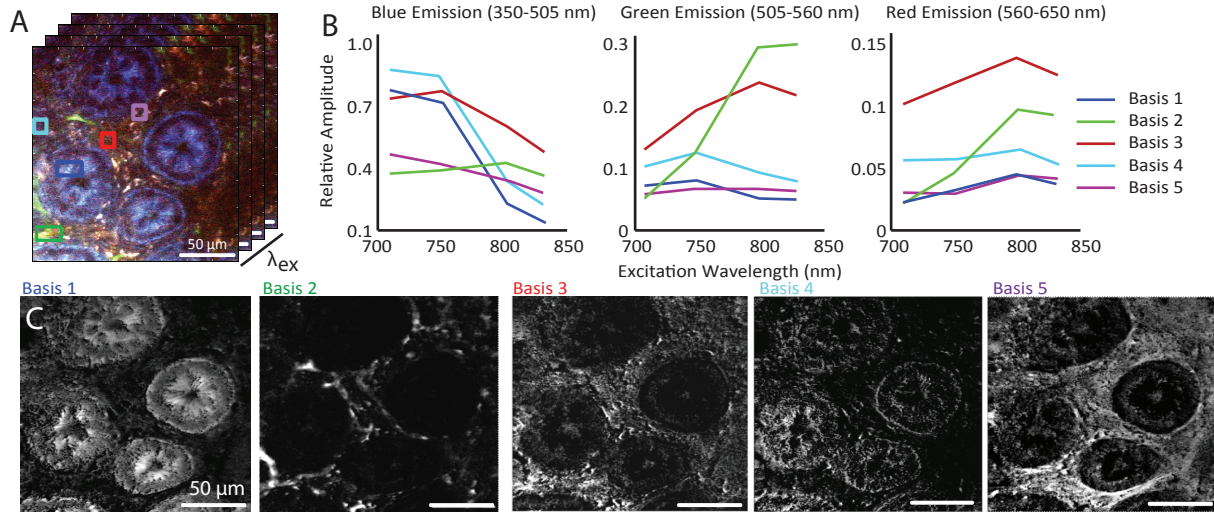


Figure 2.4: Demonstration of linear unmixing for hyperspectral data that was acquired using four excitation wavelengths in colon tissue from a rat. A. Images at multiple excitation wavelengths were acquired. B. Excitation spectra in the three emission channels for the user-selected regions shown in A. The color of each spectrum corresponds to the selection box in A. C. Images representing the concentrations of each basis spectrum. For each pixel, a non-negative least squares fit was performed to obtain the concentration of each species.

Figure 2.4. 2) By averaging the spectra of various tissue types taken from many different mice, the same basis spectra can be used for analysis of all data sets, which provides a ‘spectral signature’ for differentiating tissue types.

In Figure 2.4, every pixel in the hyperspectral data set contains a value for each of the four excitation wavelengths in three emission channels. The data from the three emission channels is used for linear unmixing, so that the shape of the excitation pattern is considered in the least squares fit, as well as the relative emission in the blue, green, and red channels. For a single imaging plane, such as the one in Figure 2.4, this method is advantageous because the three color emission pattern for each excitation wavelength adds to the total spectral information. However, since one of the main advantages of two-photon microscopy is imaging deep into turbid media, hyperspectral unmixing with a predetermined or standard set of basis spectra is often used for planes at different depths. The amount of tissue between the imaging plane and the detector affects the absorption and scattering of the emission light (both of which are wavelength dependent), and therefore the overall relative amplitude of

the three emission channels will vary significantly at different depths. These cases need to be considered more carefully, either by unmixing with only one emission channel or by allowing the relative amplitude of each emission channel to be a free parameter to allow inclusion of excitation spectra from all three emission channels.

The main advantages of this image segmentation technique are illustrated by the component images in Figure 2.4. These component images isolate particular features in the images that were identified in section 2.1.2 as relevant measures for disease states. The signal from the glands (basis 1) is probably coming from NADH, based on the excitation spectrum and known presence of NADH in epithelial tissues that make up the glands shown in the figure. In basis 5, the structural ‘backbone’ of the colon tissue is apparent. Blood vessels are visible in basis 2, since this particular animal had FITC in the vasculature. All these structures are features that could be used to monitor cancer, and our ability to identify them prompted the study presented in section 2.4.

2.4 Application: hyperspectral nonlinear microscopy in normal and diseased gastrointestinal tissues

The purpose of this study was to apply hyperspectral microscopy to healthy and diseased gastrointestinal (GI) tissues in order to visualize morphology of fresh tissue, characterize the intrinsic contrast within the gastric mucosa, and determine the spectral signatures of the major tissue components that make up GI tissues. Spectroscopic studies in bulk tissues have suggested that the most common sources of fluorescence in GI tissues are reduced nicotinamide adenine dinucleotide (NADH), flavin adenine dinucleotide (FAD), collagen, porphyrins, tryptophan and phospholipids (Wallace and Kiesslich, 2010). However, bulk tissue studies capture all of these fluorescent emissions together, with no knowledge of the cellular compartments from which they originate, making measured spectra difficult to separate and interpret (Bohorfoush, 1996; Cothren et al., 1990).

Our combined high-resolution and spectroscopic technique is useful because it uses knowledge about the structure of tissue to isolate the fluorescence signal from small volumes that contain fewer fluorescent species than bulk tissue. Our results demonstrate the value of hyperspectral two-photon microscopy for imaging gastric mucosa and also affirm that the technique is well suited to resolving subcellular morphology in fresh GI tissues using only endogenous contrast (Rogart et al., 2008).

2.4.1 Animal models

Freshly excised tissues from a total of 15 (10 normal and 5 transgenic) recently euthanized mice were used for imaging and spectral analysis. The animals were euthanized with an overdose of isoflurane, dissected, and then selected GI tissues were dissected and imaged. Tissue was bathed in saline prior to imaging, and all imaging occurred within four hours of euthanasia. In some cases, images were acquired from the outside of the gastric lumen, with

the tissue still intact in the body. In other cases, a piece of GI tissue was removed, opened flat, gently rinsed with saline and imaged on a recessed microscope slide. Tissues were then processed, sectioned and stained with hematoxylin and eosin (H&E) for comparative histology.

Cancer model. A transgenic mouse model (Male C57BL/6J-APC Min/+) that spontaneously develops malignant polyps in the small intestine was used for comparison of neoplastic to normal tissue. A total of 5 transgenic mice were imaged at 15-20 weeks of age, a stage at which adenomas should be developed. Data from one of these mice is shown.

2.4.2 Morphology of the lower gastrointestinal tract

The gastric mucosa collectively includes the epithelium, lamina propria, and muscularis mucosa. Figure 2.5 shows a schematic diagram of the general organization of the small intestine and colon. In the small intestine, villi increase surface area for more efficient digestion and nutrient absorption. The lamina propria extends to form the core of the villi, and a continuous layer of epithelium forms a barrier between this core and the contents of the intestinal lumen (Figure 2.5E). Epithelial tissue is comprised of a single layer of columnar epithelial cells, which generally function to absorb nutrients and fluid. Specialized goblet cells within the epithelium secrete mucin as a lubricant and chemical barrier. At the base of the villi, epithelial tissue dives into the lamina propria layer to form crypts of Lieberkühn, which are intestinal glands located throughout the GI tract. The lamina propria of the small intestine is made up of loose connective tissue including lymphocytes, fibroblasts, plasma cells, other lymphatic tissue, and a network of blood capillaries (Ross and Pawlina, 2006). Smooth muscles cells are present in the villi alongside central lymphatic capillaries called lacteals. In the colon (Figure 2.5J), lamina propria is much the same as in the small intestine except for the absence of lymphatic vessels and better developed lymphoid tissue. In addition, there are no villi but a larger number of secreting goblet cells. Crypts of Lieberkühn

are more densely packed. Lymphoid aggregates, or Peyer's patches, are present in both the small and large intestines and are important for the GI's immune response (Figure 2.5L). Peyer's patches are comprised primarily of lymphocytes and contain a network of connective tissues including type-IV collagen, laminin, and fibronectin (Ohtsuka et al., 1992).

In Figure 2.5, two-photon microscopy of intrinsic contrast is used to visualize the morphology of normal small intestine and colon, and is shown alongside high magnification white light imaging and conventional histology. White light images were acquired from fresh tissue using a digital camera focused through the eyepiece and objective lens of our two-photon microscope. Although the white light images alone show contours of the tissue, they cannot resolve cellular morphology (Figure 2.5A&F). The two-photon images (acquired with an excitation wavelength of 740 nm) can distinguish not only individual cells, but subcellular structures such as nuclei, which appear as dark circles (Figure 2.5H). Figure 2.5B shows villi laying flat on the inner surface of the small intestine, while Figure 2.5C shows the deeper glandular level of the small intestine. Circular crypts at the base of the villi can be seen. Figure 2.5F shows the superficial epithelial layer of the colon, while Figure 2.5G shows a deeper layer with tightly packed crypts. Figure 2.5K shows a mosaic of images spanning a 2.5 mm wide piece of tissue that included a Peyer's patch. In the single images composing this mosaic, individual crypts can be clearly seen in the tissues surrounding the patch. At the ensemble scale, the undulations of the mucosa can be seen, along with the structural changes that the growing Peyer's patch has imposed on its surroundings. Corresponding histology images of Peyer's patches are shown in Figure 2.5L.

All of these images were acquired with an excitation wavelength of 740 nm, and images shown are red-green-blue merges of data from our three emission channels, scaled to the maximum in each channel for each image. However it is clear from these images, that the epithelial tissue composing the outer layers of the villi, and the crypts of both the small intestine and colon have a distinctive blue color. Another common feature are

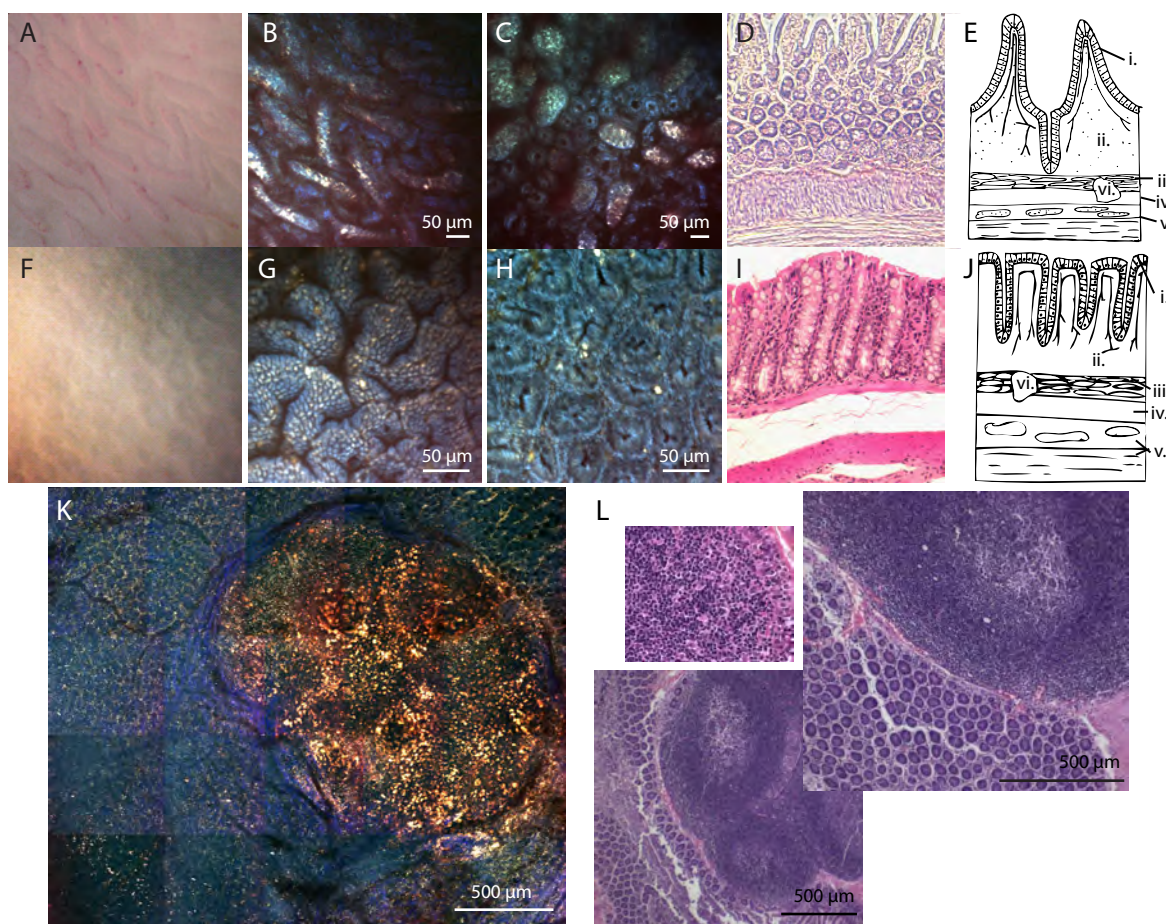


Figure 2.5: Comparison of small intestine and colon using white light imaging, two-photon microscopy and conventional H&E histology. A. White light image of fresh tissue from normal small intestine. B. The same field of view as in A acquired using two-photon microscopy with 740 nm excitation. C. A TPLSM image of a deeper layer of the small intestine reveals intestinal glands at the base of the villi. D. Cross-sectional H&E histology of the small intestine showing the layers of the mucosa. E. Schematic morphology of the small intestine. Epithelium (i.) covers the villi and forms the crypts. Lamina propria (ii.) extends into the core of the villi and contains a vascular network. The remaining layers are the muscularis mucosa (iii.) submucosa (iv) and the muscularis externa (v). Lymphoid aggregates or Peyer's patches of varying size (vi.) are found in the submucosal layers. F. White light image of fresh, normal colon tissue at 20x magnification. G. A two-photon image showing the folds in the superficial epithelial layer of the colon. H. Two-photon image of the same piece of colon tissue revealing densely packed crypts 80 μm below the epithelial layer shown in E. I. Cross-sectional H&E histology of the colon showing that the crypts extend through the full thickness of the lamina propria. J. Schematic morphology of the colon. Epithelium (i.) lines the mucosa and extends into the lamina propria (ii.) to form the crypts. The remaining layers are the muscularis mucosa (iii.) submucosa (iv) and the muscularis externa (v). As in the small intestine lymphoid aggregates or Peyer's patches of varying size (vi.) are found in the submucosal layers. K. Two photon image of a Peyer's patch found in the small intestine. L. H&E stained Peyer's patches.

yellow-white bright spots that can be observed within the villi cores and lamina propria. Particularly around the Peyer's patch, pure blue-colored filamentous structures can be seen. While these 'color codings' are relatively simple to pick out of the images, they are rather qualitative and subjective. They also raise many questions which we can directly address with our hyperspectral microscopy technique, namely; 1) what substances are causing these distinctive colors? and 2) can these colors be used to isolate and identify key structures in each image (such as crypts)?

The images in Figure 2.5 also highlight one of the additional major benefits of two-photon imaging on fresh tissue; 3D sectioning. Conventionally, histology is used to visualize morphology, which requires destructive physical slicing for sectioning, and often causes distortion and difficulty co-registering between slices. The fluorescence images in Figures 2.5G and H were acquired in the same piece of tissue, simply by moving the microscope objective along the z direction.

2.4.3 Image guided two-photon spectroscopy

As stated above, the two-photon fluorescence images shown in Figure 2.5 were acquired using an excitation wavelength of 740 nm, and while tissue components had fairly distinctive 'colors', the origins of these signals were difficult to quantify. However, if the excitation wavelength is varied, different structures within the image contribute varying amounts of signal to the red, green, and blue emission channels, thereby revealing different information about the origin of each tissue type's fluorescence. Figure 2.6 shows two-photon images acquired at the same location but with different excitation wavelengths. Figures 2.6A&B show a region of the small intestine in a plane that transects the villi. At 740 nm excitation, the outer layers of the villi appear blue like the crypts in the colon (Fig 2.6A). However, at 890 nm, the same region exhibits dark green fluorescence (Figure 2.6B). The epithelial surface of the colon in Figures 2.6C&D can be seen to be composed of individual cells which

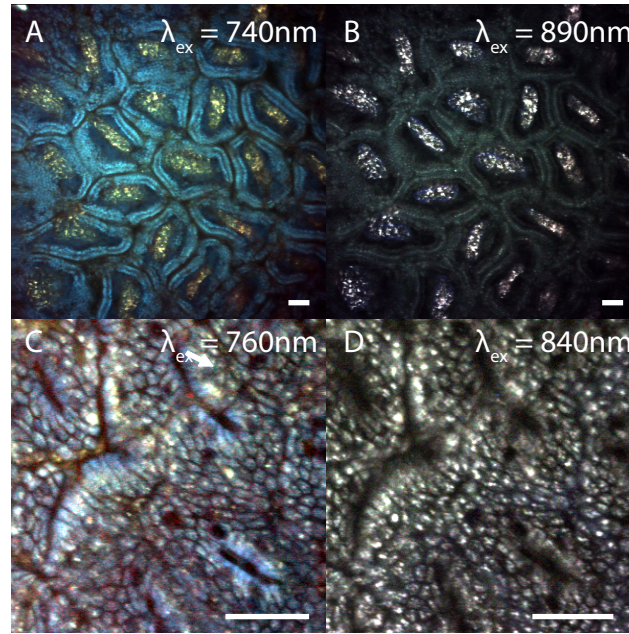


Figure 2.6: The effects of varying two-photon excitation wavelength. The structures visible in the same field of view depend on the excitation wavelength that is used. The images shown are averages over a 25 nm range at 5 nm steps with center wavelengths reported in the figure. (A) Image of the villi in the small intestine at 740 nm. The epithelial layer around the villi appears blue. (B) At $\lambda_{ex} = 890$ nm, the centers of the villi show the strongest contrast while the outer epithelial layer appears green. (C) Layer of epithelium closest to the lumen in the colon. Colon folds and individual cells are visible at 740 nm. (D) At higher excitation wavelengths, bright patches of fluorescence are more prominent within individual cells. Images are scaled RGB merges, so note that the relative color mix in each image is determined only by the particular structures in each image. Scale bars, 50 μ m.

have regions that appear blue at 740 nm, but which show different intracellular structures at 840 nm excitation.

We can harness these excitation-dependent spectral changes using hyperspectral wavelength scans, as described in Section 2.3.2, where images are acquired at a series of excitation wavelengths, generating an excitation spectrum (for our 3 emission bands) at every pixel in the image. Rather than qualitatively comparing the emission of different tissue types, we can then use this hyperspectral data to determine the specific excitation-emission spectral signatures of the major tissue types that we observe in our fluorescence images.

Spectral signatures were extracted from small regions within each data set that corresponded to particular common tissue types / species; epithelium, lamina propria, collagen

and lymphatic tissue. Choice of these regions was guided by our knowledge of the structures and organization of the colon and our ability to visualize common morphologies as shown in Figures 2.5 and 2.6. ‘Epithelium’ was chosen from the outer layers of the villi in the small intestine (blue in Figure 2.5B) and the regions making up the crypts in the colon (Figure 2.5G). ‘Lamina propria’ was most easily distinguishable beneath the epithelium in the villi, and was therefore chosen from small intestine only. We limited our definition of lamina propria to the small intestine for two reasons: segmentation was clearer and lamina propria in the large intestine contains additional connective tissue which we captured in the collagen component. ‘Collagen’ signatures were selected from regions that looked fibrous and exhibited bright blue SHG at longer excitation wavelengths. ‘Lymphatic tissue’ signatures were chosen from Peyer’s patches found in the small intestine, which are composed primarily of lymphocytes.

Basis spectra were calculated by averaging the values of the pixels in each selected region at each excitation wavelength and for all three emission channels. This process was repeated for 2-6 image sites within each of 2-4 different mice that were imaged in order to obtain the average ‘basis spectra’ for these specific tissues. The overall signal amplitude of extracted spectra varied depending on imaging depth; however, the shapes of the excitation spectra were consistent. Therefore, we normalized each basis spectrum set (corresponding to excitation spectra for the blue, green and red emission channels) to the maximum of the blue emission channel’s excitation spectrum prior to calculating the average basis spectra for each tissue type across mice. This normalization preserved the relative amplitudes of the blue, green, and red emission bands. These basis spectra are shown in Figure 2.7

Raw basis spectra extracted in this way are not calibrated to account for wavelength-dependent effects originating from our system. These effects are most easily visible in Figure 2.7 in the repeatable, jagged pattern seen for all tissue types. As described by Equations 2.1 and 2.2 in section 2.3.2, variations in two-photon emission result from properties of

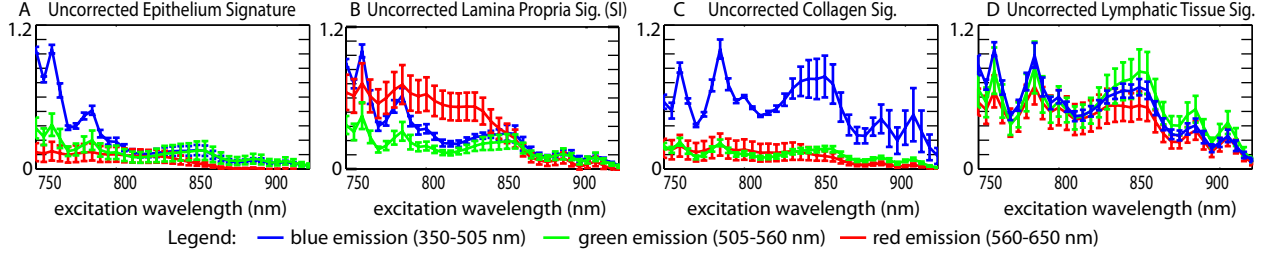


Figure 2.7: Mean spectral signatures of the four tissue components before FAD calibration. Error bars are one standard deviation above and below each data point. The excitation wavelength dependent envelope K is present in all data sets A.-D. Calibration to FAD was done in order to better identify the possible sources of contrast and to prevent confusion in interpreting the biochemical origin of these spectral signatures.

the sample, but also from wavelength-dependent changes in laser power and pulse width, dispersion through our system's optical elements, numerical aperture the and excitation wavelength itself. Based on those equations, K is a wavelength-dependent factor which is partially dependent on the arrangement of optical components within any two-photon instrument. Therefore, K is unique to each microscopy system.

Calibration. In order to more clearly visualize the extracted two-photon excitation-emission basis spectra of the selected tissues, and to better understand their composition, it was necessary to calibrate our spectra by removing the effect of K . In order to measure K , we needed a standard fluorophore either with a known two-photon excitation spectrum, or one with an approximately flat excitation spectrum across our excitation range. We chose to use a pure solution of FAD (Sigma Aldrich F6625) as this reference fluorophore, since the absolute one-photon and two-photon excitation cross sections of FAD have been reported as relatively flat for excitation wavelengths between 355-460 nm / 710-900nm, respectively (Radosevich et al., 2008; Huang et al., 2002).

To obtain an FAD reference spectrum, we measured the two-photon fluorescence from the green emission channel of our system (505-560nm) while scanning a small well beneath a cover glass filled with a 400 μ M solution of FAD (Sigma Aldrich F6625) in phosphate buffered saline (PBS). If we assume that Q , Φ and σ_2 for FAD are approximately excita-

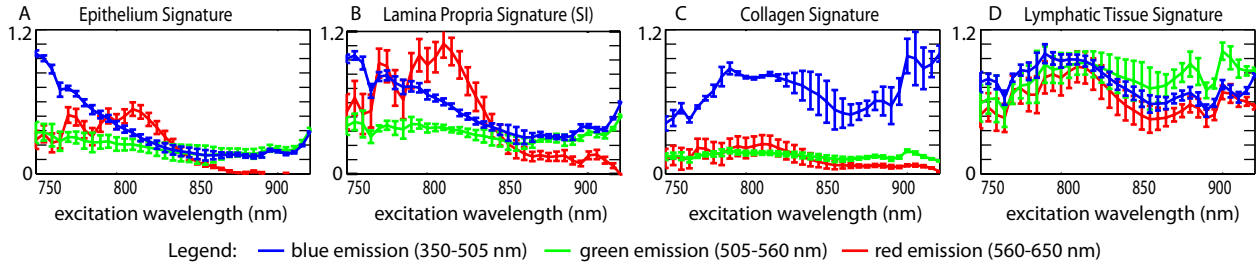


Figure 2.8: Mean spectral signatures extracted from four tissue types, after spectral calibration via normalization by in-vitro FAD spectra. Error bars are one standard deviation above and below each data point. (A) Epithelium: $n=6$ (4 mice, 6 sites) (B) Lamina propria: $n=3$ (2 mice, 3 sites) Lamina propria signatures were all taken from samples in the small intestine to minimize collagen overlap. (C) Collagen: $n=4$ (2 mice 4 sites) (D) Lymphatic tissue: $n=4$ (2 mice 4 sites).

tion wavelength-invariant, then the green emission channel measurement is equivalent to K multiplied by a single scalar value. Therefore, basis spectra extracted from our wavelength scans of GI tissues were divided by this measured FAD excitation spectrum to remove the effect of K from all three emission channels of our data. While this calibration approach adds the small effect of the excitation-wavelength dependence of FAD fluorescence to the spectra shown, the calibration removes the much larger envelope from systematic effects and allows comparison of our spectra to each other, and to one-photon excitation spectra from the literature. The calibration process is shown in Figure 2.9A.

In order to account for the wavelength-dependent spectral response of our PMT detectors, their gains, and emission filter efficiency and bandwidth differences between emission channels, scaling factors were also applied to the green and red channels. These scaling factors were determined using back-illumination of the system with 3 narrow-band filtered LEDs adjusted to have identical powers within the blue, green and red emission channels' bandwidths. Figure 2.8 shows the final extracted basis spectral signatures, after these spectral calibrations, corresponding to the four selected tissue types; epithelial tissue, lamina propria, collagen and lymphatic tissue.

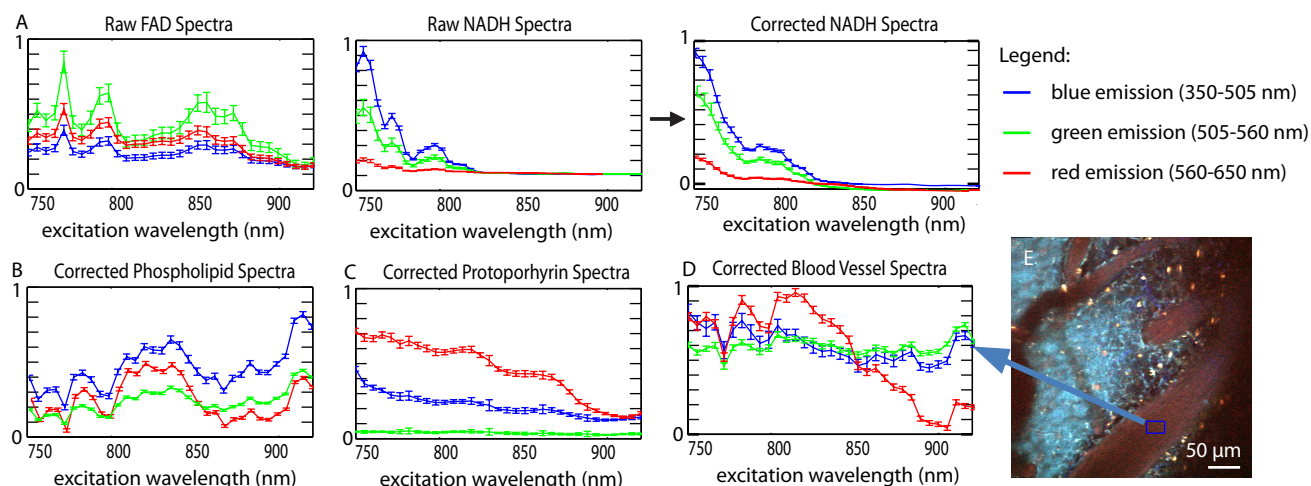


Figure 2.9: FAD spectral calibration, and corrected spectra of in vitro pure fluorophore samples. A. Left; excitation spectra for three emission bands (red, green and blue) acquired on a sample of pure FAD. Center; an uncorrected excitation spectrum of a pure sample of NADH, and Right; the corrected spectrum after dividing all three emission channels (red, green and blue) by the green-emission excitation spectrum of FAD. B. Wavelength-calibrated spectra of Zinc-protoporphyrin IX C. Wavelength-calibrated spectra of phospholipid D. Shows the excitation spectra extracted from the center of a large blood vessel imaged in the living brain of a rat as shown in E. No exogenous contrast is present in the image, and the blood vessel can be clearly discerned, making it clear that the red fluorescence signal observed is coming from whole blood. All error bars show one standard deviation above and below the mean.

Preparation of in vitro references. The reference spectra provided in Figure 2.9 were measured in solution in a small reservoir topped with a coverslip. The concentrations and lot numbers of the in vitro references are provided here. FAD: 400 μ M solution in phosphate buffered saline (PBS), Sigma Aldrich F6625. NADH: 400 μ M solution in PBS, Sigma Aldrich N6636. Zinc-protoporphyrin IX: 300 μ M solution dissolved in dimethylsulfoxide (DMSO), Sigma Aldrich P8293. Phospholipid mixture dissolved in chloroform, Sigma Aldrich P3817.

2.4.4 Origin of intrinsic contrast

These calibrated spectra allow interpretation of the biochemical constituents of each of the selected tissue types. Figure 2.9 includes two-photon excitation-emission spectra of a range of pure in vitro samples of known intrinsic fluorophores, specifically FAD, NADH, zinc proto-

porphyrin and phospholipid, as well as whole blood. Based on these spectra, and reported 1- and 2-photon spectra of intrinsic fluorophores (Table 2.1) we hypothesize that the primary contributor to the epithelial fluorescence signature is most likely NADH, given its strong emission in the blue channel when excited with wavelengths < 800 nm. The flat green emission for all excitation wavelengths suggests FAD also contributes to the epithelial signature. Epithelial cells are constantly regenerating, therefore it is reasonable to expect NADH and FAD will be major sources of autofluorescence (Wu and Qu, 2006). Lamina propria likely also contains NADH and FAD, however the different excitation patterns in each emission channel suggest there are multiple contributors to its spectral signature. Since the lamina propria contains the GI capillary network, we suspect that porphyrin fluorescence in blood is resulting in the peak in red emission at lower excitation wavelengths. The lymphatic tissue signal is similar in all three emission channels, suggesting that its origin is a single fluorophore with broad excitation and emission. Few intrinsic fluorophores have strong red emission, therefore we suspect the fluorescence originates from phospholipids, known to be a significant component of lymphocytes (Zakaryan et al., 2001). Almost the entire collagen signal is in the blue emission channel, since the major signal that we detect from collagen is due to SHG. SHG generates narrow-band light at half the excitation wavelength, with higher signal coming from longer wavelengths. At wavelengths lower than around 780 nm, the SHG light generated at < 390 nm will be heavily attenuated in tissue, and will not transmit well through our system's glass lenses and filters.

Hyperspectral two-photon microscopy can provide an enhanced analysis of the underlying composition of tissues based not only at their apparent emission colors in images using a single excitation wavelength, but also on their interesting and complex excitation and emission spectra.

2.4.5 Linear unmixing

Extracting spectra from small regions and averaging over multiple samples does not necessarily demonstrate that a given signature is wholly unique to a particular tissue type. Here, we applied linear unmixing to delineate regions of the images based on their spectral signatures, and to better visualize the hyperspectral data. The mathematical method for this analysis was described in section 2.3.2.

Using this unmixing strategy, we were able to derive four coefficients per pixel from the images shown in Figure 2.10, which corresponded to the relative contribution of each basis spectrum to the overall spectrum of the pixel. Visualizing each of these coefficients as an image reveals the relative amounts of each constituent within the image. As we showed in a previous study (Radosevich et al., 2008), it is not necessary to calibrate for the wavelength-dependent factor K during unmixing, since it should affect all basis spectra and measured hyperspectral data in the same way. We therefore did not perform spectral calibrations on the basis spectra before unmixing to avoid the introduction of unnecessary systematic effects or rounding errors. To demonstrate the robustness of our spectral signatures, basis spectra used for unmixing were not derived from these same data sets that underwent unmixing.

We used the blue and green emissions of the average uncalibrated versions of the basis spectra reported in Figure 2.7 to spectrally unmix five hyperspectral data sets acquired on fresh GI tissues as shown in Figure 2.10. Prior to unmixing, each basis spectrum was normalized to the maximum of its blue emission, and for display, each set of unmixed components was normalized to make the maximum of the epithelium image equal to 1. This means that the relative intensity scale on each image represents the amount of each unmixed tissue type relative to the amount of epithelial tissue present. Figure 2.10A-C show normal tissues at the glandular level of the colon (A), within the villi in the small intestine (B), and at the glandular level of the small intestine (C). Figure 2.10D shows the central part of a Peyer's patch, and Figure 2.10E shows a neoplastic lesion from the small intestine of

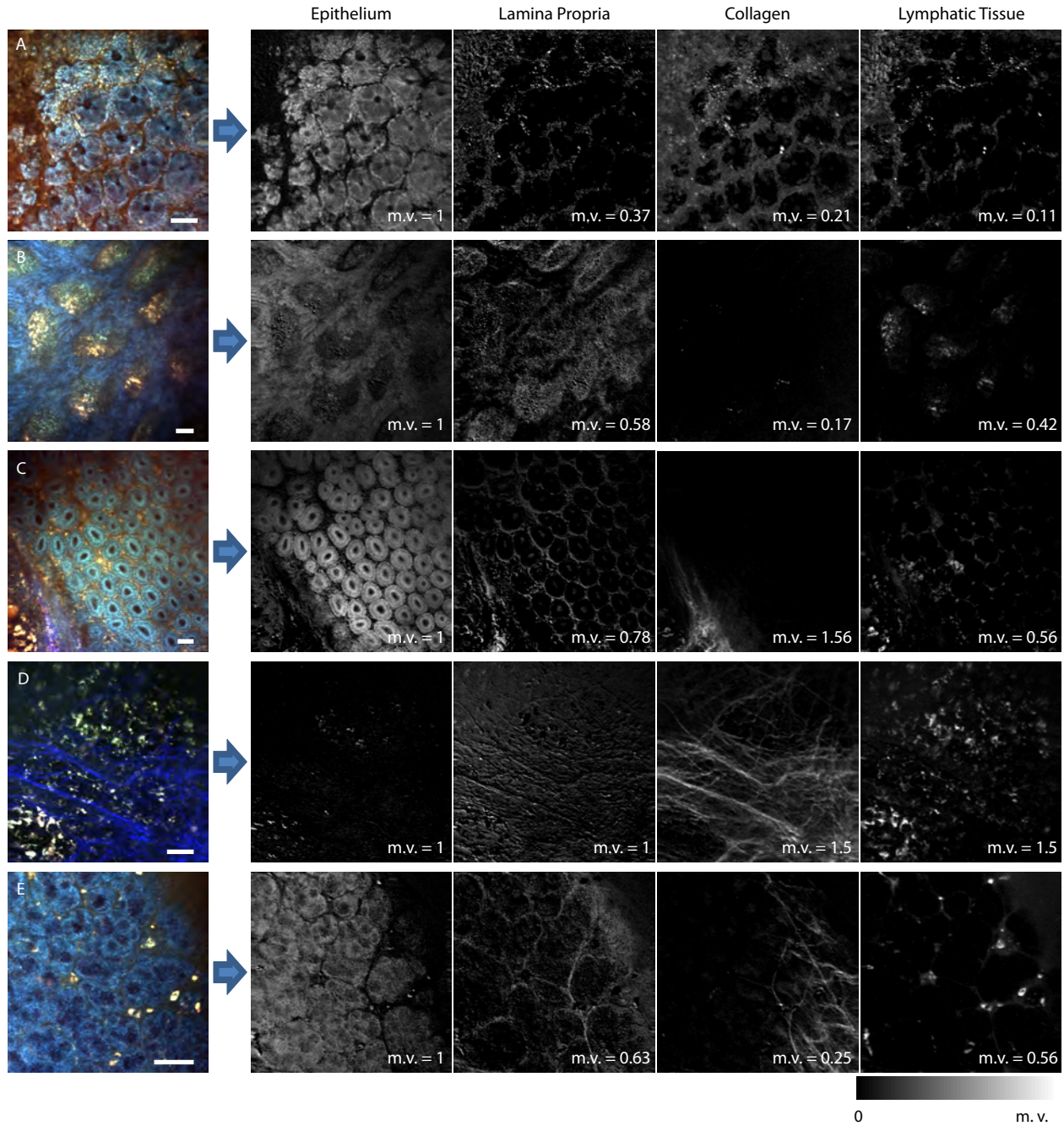


Figure 2.10: Hyperspectral data unmixing of images of gastric tissues using averaged basis spectra. RGB images are at 740 nm excitation, except for D is at 890nm. Grayscale images are scaled from 0 to the maximum value (m.v.) reported in each image. Scale bars are all 50 μm . A. Glandular level of normal colon B. Villi in the small intestine. C. Glandular level of the small intestine, with the edge of a Peyer's patch in the lower left hand corner. This image was acquired in situ, through the muscularis externa and serosa. D. A Peyer's patch in the small intestine. (E) A cancerous lesion in the small intestine of an APCmin+/- mouse. The epithelial structure is very different to that seen in normal tissues, and the presence of collagen is a feature of neoplasia.

an APC Min/+ mouse. Conventional RGB merges of these regions, acquired at 740 nm are shown in the left column, while the grayscale images shown in the other columns are images of the coefficients corresponding to the fit of each pixel to each of the four respective spectral signatures shown in Figure 2.7. Images that correspond to epithelial tissue components show either crypts (Figure 2.10A, C) or the epithelial tissue that covers the villi (Figure 2.10B). Collagen is represented strongly in the scaffold surrounding the glands of the colon tissue (Figure 2.10A), but not in the tissues from the small intestine (Figure 2.10B, C). Lymphatic tissue is present in all of the data sets, particularly in the Peyer’s patch (Figure 2.10D), which is expected since it is a lymphoid aggregate. The Peyer’s patch can also be seen to include almost no epithelial tissue and a significant network of collagen filaments. Changes associated with neoplasia are shown in Figure 2.10E. Abnormal epithelial overgrowth is apparent, as well as pockets of lymphatic tissue. The collagen image shows structure which is also different compared to the normal tissues, suggesting overproduction of extracellular matrix as is commonly associated with neoplasia (Liotta and Rao, 1985). Based on the possibility that our lamina propria basis spectrum may include porphyrin, it is interesting to note that the lamina propria components for all the samples reveal structures that correspond well to the likely locations of blood vessels (e.g. between crypts and in the center of villi). Noting this, we suspect that the disordered network revealed in the lamina propria image of the neoplastic lesion could correspond to excessive and abnormal vascularization within and around the tumor.

Visualization of hyperspectral data. Visualization of hyperspectral data can be challenging, since the data set contains more information than a single fluorescence image shows. In Figure 2.11, we show the component images presented in Figure 2.10 false-color composite merges. Representative H&E histology of these GI tissue types are shown alongside to these merges to demonstrate the parallel information that can be obtained by our image segmentation technique. Because the merges can be made with any colors, the images pro-

vide more contrast than is possible using the pink and purple colors common to histology. The color-coding for the merges is shown in 2.11A, and is consistent for the figure. At the crypt level of colon (2.11B), the epithelial tissue is surrounded by a mixture of the three other components: lamina propria, collagen, and lymphatic tissue. Corresponding histology (2.11G) shows connective tissue around the crypts (black arrow) as well as a few dark staining lymphatic cells (red arrow). In the small intestine (2.11C), the main components of the cores of the villi are lymphatic tissue and lamina propria. Histology (2.11H) shows epithelium surrounding each villus and loose connective tissue forming the core of the villi. At the boundary of a Peyer's patch and the crypt level of small intestine (2.11D), all four components are visible. Lamina propria signal is particularly strong along the blood vessel at the boundary (arrow) (2.11I) Histology of the Peyer's patch boundary. (E) Close up of the lymphatic cells that comprise a Peyer's patch. The strong signal from lymphatic tissue and collagen 'co-stain' this false color merge. Peyer's patch histology (2.11J) shows the darkly staining nuclei of lymphatic cells, but without special staining cannot identify the connective tissue. (2.11F) Merge shows the spatial registration of the four components in a neoplastic region of an APC^{min}/+ mouse. Histology of a lesion (2.11K) shows a thickened and irregular epithelium which is characteristic of neoplasia.

Discussion. Overall, these hyperspectral unmixing results support the uniqueness of the basis spectra extracted from small representative regions of epithelium, lamina propria, collagen and lymphatic tissue, demonstrating that they are consistently able to identify these tissue types throughout a range of samples, mice and GI tissue types. The fact that the basis spectra chosen were averages from different samples than those that underwent unmixing further underscores the robustness of the signatures, as well as the promise of this approach for blind tissue delineation and identification.

It should be noted that for these hyperspectral unmixing results, data acquired in the red channel of our system was excluded. We chose to do this because, although the

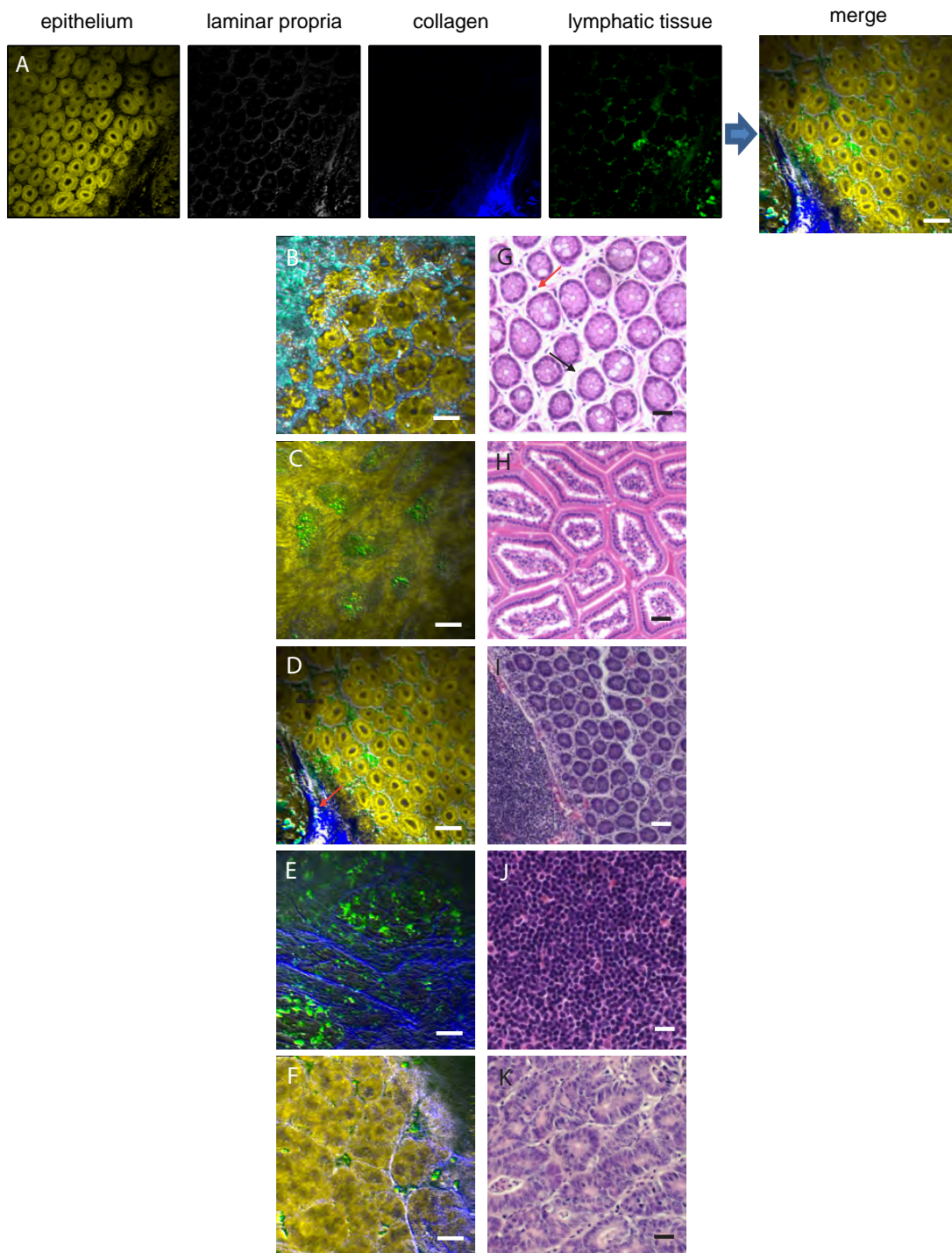


Figure 2.11: False color merges of component images. In A., component images are shown with false color with the merge at right. The color scheme used is consistent for all the unmixed images in B-F, with yellow corresponding to epithelium, white to lamina propria, blue to collagen, and green to lymphocytes. Scale bars for all images are 50 μm .

shape of excitation spectra extracted from hyperspectral data matched the basis spectra, the overall relative amplitude of the blue, green and red emission channels varied due to variation in imaging depths. The red channel differed most significantly from the blue and green detection channels. Since we include the relative intensity amplitudes of the emission channels in our algorithm, we found that inclusion of the red channel often led to poor fits and large residuals. We believe that this effect may be due to the substantial and different levels of attenuation of visible (blue, green and red) light within tissue, such that images acquired at different depths would have different relative levels of attenuation for each emission channel. We particularly note that hemoglobin absorption, although large, is actually quite similar in the blue/green range, but dramatically different (much less) for the red emission range. Therefore, the presence of blood could be one cause of the relative amplitude variations between the detection channels that we have observed. Since most of the intrinsic fluorophores of interest emit in the lower blue-green spectral regions, and since the blue and green emission bands were found to have less variance relative to each other, we chose to exclude the red channel. However, we note that approaches such as allowing the relative amplitude of each emission channel to be a free parameter could feasibly have allowed inclusion of information from the red excitation spectrum.

This difficulty highlights the advantage of spectral unmixing combining excitation-scanning with emission spectra detection. Tissue absorption and scattering over the near infrared range vary less than in the visible range of 350-650 nm. Researchers acquiring spectral two-photon data consisting of only emission spectra (visible light) face many challenges compensating for the effects of depth and tissue-dependent variations in attenuation, and have not typically be able to perform spectral fitting or unmixing (Laiho et al., 2005; Palero et al., 2007; Chen et al., 2007).

2.4.6 Goodness of fit

The basis spectra used for the spectral unmixing described above were deliberately selected from data sets other than those that were unmixed to test how well our approach can provide blind identification of tissue types. To quantify the performance of this hyperspectral unmixing strategy, we report the residuals of the non-negative least squares fits to our hyperspectral data in Figure 2.12. The value of each pixel in the images shown in Figure 2.12A-E represents the squared Euclidian norm of the residuals calculated for each excitation wavelength (the error output of the `lsqnonneg` function in MATLAB). We chose to present the error in this way because the normalized residual represents the error for the entire fit across all excitation wavelengths and both emission bands. For each data set, we also compare measured spectra with corresponding spectral fits for regions of each image with high or low residual values. Selections outlined by red boxes in Figure 2.12 correspond to low error regions and show good agreement between the fit and the measured data in both the blue and green emission channels. Regions of the image with relatively high error, outlined by cyan boxes, can be seen to generally underestimate the real data for lower λ_{ex} and overestimate for higher λ_{ex} , particularly in the blue emission channel. The error tends to be highest for structures that appear to be collagen. We suspect that the orientation dependence of SHG contributes to these errors, although these high residual regions could also imply that there is an additional spectral component (tissue constituent) that is not being accounted for by our four basis sets. Slight movement of the sample during a wavelength scan could also account for some of the fitting errors. Overall, however the fitting performance shown is fairly good, supporting our earlier conclusions that the extracted basis spectra well represent, and are capable of identifying the chosen basic tissue types within GI tissues.

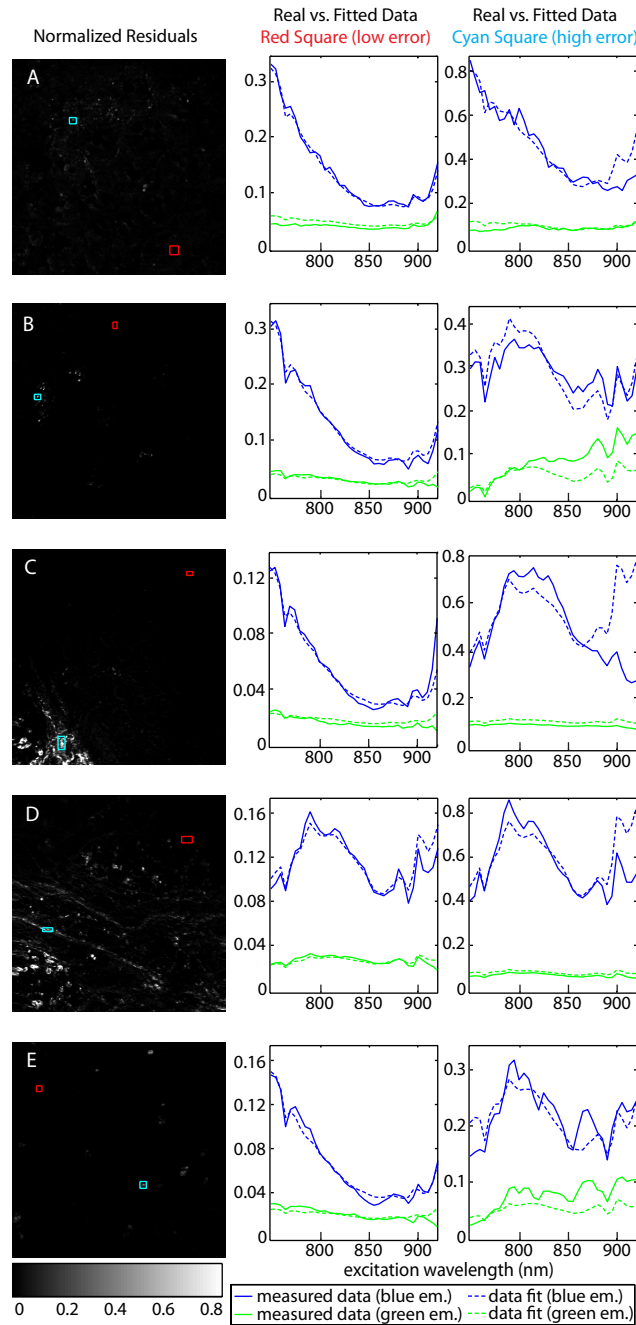


Figure 2.12: Residuals for the non-negative least squares fits of hyperspectral data that correspond to analysis shown in Figure 2.10. Images (left column) show the square of the Euclidean norm of the residuals from all excitation wavelengths. Plots (right) compare the measured spectra to the fitted data in selected areas of the images for a well matched region (red box) and a region with relatively high error (cyan box). A. Glandular level in the colon. B. Villi in the small intestine. C. Glandular level of the small intestine. D. Peyer's patch in the small intestine. E. Lesion from the small intestine of an APCmin/+ mouse.

2.4.7 Summary

We have introduced a new method for microscopic examination of fresh gastric mucosa. By using hyperspectral two-photon microscopy, we showed that 3D morphology can not only be visualized, but that different structures have unique spectral signatures. We demonstrated that these signatures can allow automated image segmentation, while also providing information regarding the identity of the fluorescence species composing different sub-tissue types.

Improved understanding of the intrinsic contrast of GI tissues, and the subcellular origins of specific spectral components, could provide guidance for enhanced wide-field endoscopic screening and imaging technologies. Our approach is not only able to delineate the different spectral components of these complex tissues, but can also assign these spectra to their cellular-level origins and, in principle, quantify their likely contributions to bulk tissue spectroscopy measurements or wide-field fluorescence imaging. Furthermore, in future experiments we hope to explore the hyperspectral intrinsic contrast of *in vivo* GI tissues in various stages of neoplasia, since there is substantial evidence that the metabolic and protein-binding state of tumor cells will exhibit distinctive spectral signatures to which hyperspectral two-photon microscopy could be sensitive (Skala et al., 2007; Georgakoudi et al., 2002). We expect that such microscopic hyperspectral studies could allow the design of more specific wide-field screening configurations that would target the key intrinsic spectral signatures of early disease.

The main benefit of applying hyperspectral unmixing techniques to spectral two-photon data is that it captures more detail than looking at a single morphological image alone. For example, an image acquired at 740 nm can be examined to see that the endothelium is abnormal based on morphology; however, an image at 800 nm would need to be compared to view the overlying collagen structure of this region. Inspecting the complete image stack could allow someone to visualize a range of structures that are present in dif-

ferent emission channels as excitation is varied. However, this would be painstaking and would require significant training and experience to do in practice. By applying automated unmixing strategies, we are effectively transforming this spectrally-encoded information into a ‘tissue-specific’ space, such that the unique spectral characteristics of each tissue are used to extract their morphology from the entire spectral data set. This is analogous to specific histological staining of a particular species, with the substantial advantages that images can be acquired and analyzed rapidly and non-destructively, and can be visualized in multiple planes to detect structures spanning 200-400 μm in depth. The added benefit to this virtual ‘staining’ is that the regions provide a type of in situ chemical analysis of that structure. Fit residuals can be leveraged to determine if a fit is accurate, and to highlight regions in a hyperspectral image that were incorrectly identified.

Chapter 3

Development of techniques for fast 3D nonlinear microscopy

A significant research area in neuroscience is the study of neurovascular coupling, defined as the relationship between blood flow, cellular metabolism, and neuronal activity. Much of the knowledge gained towards the goal of better understanding this relationship has been achieved through the use of high-speed camera imaging (Hillman et al., 2007; Bouchard et al., 2009; Chen et al., 2011; Kozberg et al., 2013). For these experiments, a small window to the brain is created by performing a craniotomy and directly imaging the brain, using either intrinsic absorption or fluorescence as a contrast mechanism. The degree of light absorption in brain tissue as a function of tissue properties and illumination wavelength provides a wealth of information including morphology of the surface vasculature, blood oxygenation within vessels, the speed of blood flow, and vessel dilation. However, imaging the surface of the brain provides a flat view of dynamics. The visible layers are integrated together, and no depth differences in vasculature can be resolved, nor can individual cells be resolved. Two-photon microscopy provides 3D images with sub-micron spatial resolution, thereby resolving cells and their location deep inside scattering tissue. Further, it obtains contrast from a wide range of intrinsic and extrinsic dyes that can target particular cell

types. By imaging microscopic structure and function faster in 3D, we can ask questions like, what is the propagation direction of a vascular response to a stimulus? Additionally, with labeling techniques, we can look into the role of specific cell types and discover how neuronal firing influences the vascular response and which cell types are involved. Because it can record signals in the native environment, 3D microscopy is a tremendous tool to study how neuronal signals propagate in the living brain.

As more studies are performed to address these questions, it has become increasingly apparent that faster volumetric scan rates would greatly improve understanding of these complex relationships. Calcium transients indicative of neural activity can be studied using calcium sensitive dyes or genetic labeling. These transients occur throughout the brain at time scales on the order of milliseconds (Duemani Reddy and Saggau, 2013). In (Chen et al., 2011), the propagation velocity of vascular dilation at the surface of the motor cortex in response to a stimulus was reported to be 2-4 mm/s. Our microscope as described in Section 2.2.2 can perform two-dimensional scanning of fields of view as large as 750 μm at frame rates greater than 15 Hz, which is sufficient temporal resolution to study events on the time scale reported by (Chen et al., 2011; Duemani Reddy and Saggau, 2013). However, because three dimensional stacks are created by physically moving the objective lens, the volume acquisition rate is limited. Therefore, without faster volumetric imaging, the relationship of dynamic events in complex, 3D neurovascular networks is invisible.

This chapter describes techniques developed as part of this thesis work to address the need for increased temporal resolution in nonlinear microscopy. It is organized in the following sections:

Section 3.1. A review of high-speed 3D imaging techniques that have been applied to multi-photon microscopy is presented. Most of the methods discussed have been developed during the last five years, underscoring the recent push for faster microscopic imaging technology and the gains that have been made toward achieving this goal.

Section 3.2. A multiplexing technique is presented that draws on the spectral analysis and linear combination properties of fluorescence that were discussed in Chapter 2. Multiple excitation spots are scanned in a sample and their spatial locations are encoded in the color of the emerging fluorescence emission. We applied our new method to study vascular dynamics in the resting-state brain. A description of the method, characterization of the system, experimental results, and validation of the method are discussed in detail.

Section 3.3. The extension of our spectral multiplexing technique to second harmonic generation microscopy is discussed. Optical design software is used to model the spatial patterning of multiple excitation wavelengths at the focal plane, and results demonstrating the feasibility of this approach for further multiplexing are presented.

Section 3.4. Volumetric imaging is demonstrated using very fast 2D imaging with resonant scanning mirrors coupled with remote focusing for volumetric acquisition rates of several Hz. The development of the resonant scanning microscope is discussed, including the addition and characterization of a lens with an electrically controlled focal length to allow axial positioning. The volumetric scanning system is used to quantify the speed of arterial and capillary blood flow deep within a living mouse brain, and to measure calcium activity from neural networks.

3.1 Current state of the art for 3D nonlinear microscopy

The inherent optical sectioning capability of multiphoton microscopes allows deep tissue imaging, but also typically requires scanning to sequentially visit each point in a sample to build up an image (see Chapter 1.2.3). Therefore, the speed of scanning systems has been limited by either hardware (ie, physical scan rates, the speed of detection electronics, and data transfer rates), or the availability of fluorescent photons to detect without causing fluorophore saturation or photodamage. Volumetric microscopy methods intended for imaging 3D volumes at high speeds must trade-off temporal resolution with the size of the volume to be measured. Recent strategies for doing this have included selective excitation of a subset of spots within a volume, faster scanning, and wide-field approaches. Table 3.1 summarizes many of these methods, which are discussed below.

Fast modulation of objective. Standard laser scanning microscopy setups generally use scanning mirrors for lateral positioning and piezo-driven actuators for axial positioning. These systems can be quite fast in their own right. (Gobel et al., 2007) developed a technique that pushed the mechanical limits of their system by creating smart 3D scan trajectories to optically record signals from large cell populations in a 3D volume. The scanning trajectories were created using galvanometric scan mirrors coupled with a piezoelectric focusing device and optimized to visit a subset of the imaging region rather than to canvas the complete volume. With this approach, in vivo calcium recordings were acquired in cubic volumes 250 μm on a side at speeds up to 10Hz, allowing stunning 4D visualization of activity in neural networks. A drawback to this approach is that by sampling only a subset of regions within the volume, the digital reconstruction of the volume requires a priori knowledge about the location of the activated cells. Further, piezo-driven objective mounts have limited oscillation frequencies and ranges that depend on and are limited by the weight of the objective.

Table 3.1: Advanced techniques for fast 3D scanning nonlinear microscopy

Technique	Special equipment	Limitations	Speed	References
Fast modulation of objective lens	Piezo objective positioning system	Piezo-based drivers have limited load, focusing ranges, oscillation frequencies	10 Hz for volumes with 250 μm side length	(Gobel et al., 2007)
Random access sampling	Acousto-optic deflectors; spatial light modulators	High levels of dispersion, highly subject to motion artifacts	10 kHz with 5 sampled points per volume and 50 μm axial range	(Duemani Reddy et al., 2008; Anselmi et al., 2011)
Multifocal scanning	Microlens array; wide field detection	Significantly reduced penetration depth	640 Hz for 128x128-pixel 2D images	(Bahlmann et al., 2007; Kim et al., 2007)
Temporal multiplexing	Temporally precise detection electronics	Multiplexing limited by laser repetition rate and fluorescence lifetime	60 Hz for volumes with 4 planes and 90 μm axial range	(Hoover et al., 2010; Cheng et al., 2011)
Remote focusing	Electrically tunable lens or deformable mirror	Degraded point spread function and numerical aperture	66 Hz axial switching rate; 6 Hz for volumes with 2 planes separated by up to 300 μm	(Grewe et al., 2011; Amir et al., 2007)
	Multiple relay objectives	Limited by inertial scan rates	2.7 kHz axial scan rate; 500 Hz for subsampling volumes with 100 μm side length	(Botcherby et al., 2012)
Light sheet imaging	Cylindrical lenses, multiple objectives	Orthogonal illumination and imaging limits sample type	Complete embryo (>10 million voxels) imaged in 45s	(Truong et al., 2011; Planchon et al., 2011)
Spectral encoding	Multiple lasers or split sources, multichannel detection	Multiplexing limited by spectral uniqueness	6.4 Hz for volumes with 2 planes and 75 μm axial range	(Grosberg et al., 2012)

Random access sampling. Similarly, random access imaging uses excitation patterns to probe regions of interest rather than scanning a complete field of view. Regions of interest are selected from a 2D image or 3D volume, and the coordinates are fed to an algorithm that can direct a focused spot to the sample without moving the objective. Random access sampling is usually achieved using inertia-free beam positioning devices like acousto-optic deflectors (AODs) and spatial light modulators (SLMs), which can steer the beam by exploiting the diffractive properties of light (Bullen et al., 1997; Salomé et al., 2006; Anselmi et al., 2011). By using assemblies of such devices, 3D beam positioning can be achieved (Duemani Reddy et al., 2008; Kirkby et al., 2010). Random access sampling can dramatically increase scan rates since the number of points visited per volume is greatly reduced. Duemani Reddy et al. recorded information from a volume at rates up to 10 kHz, ultimately limited by the time required for spatial positioning and the dwell time required for adequate signal at each point. Additionally, since only a subset of the volume is sampled, photodamage to the sample in general is reduced. A disadvantage to using AOD scanning is the system complexity. AOD setups require spatial and temporal dispersion compensation that is technically challenging and greatly reduces available laser power and excitation efficiency. Specifying regions of interest can also impose experimental bias, since by necessity the complete picture is not recorded. Not only does this limit the potential for discovery, it can also make measurements highly sensitive to movement artifacts in vivo, and lead to data that is difficult to interpret and visualize.

Multifocal scanning and patterned illumination. Multipoint scanning is a logical way to improve 2D image acquisition rates, since speed is limited most by the need for sequential scanning. For n scanning spots, frame rates will increase by a factor of n . Faster 2D rates can be combined with standard axial translation or remote focusing to achieve improved volumetric imaging speeds. (Bewersdorf et al., 1998) implemented a multifocal multiphoton microscope (MMM) using a microlens array to generate multiple foci, allowing

scan rates exceeding 200 frames/s. Image acquisition rates were limited by the sensitivity and frame rate of the camera. Since multiple regions in a sample are excited simultaneously, the resulting fluorescence image could be viewed by eye or camera, without the need for computer reconstruction. Wide field detection is a necessary component of multifocal strategies since all the detected fluorescence cannot be assumed to originate from a single point. However, because wide field detection strategies rely on correct spatial mapping of photons from the sample to pixels on the detector, scattered photons will reduce image quality. As the number of scattered photons increases with imaging depth, the need for wide field detection severely limits the ability to image deep into tissue.

More recent implementations of MMM have demonstrated unprecedented speeds using electron-multiplying CCD cameras (Kurtz et al., 2006; Bahlmann et al., 2007) or strategies to mitigate the imaging depth degradation (Kim et al., 2007). Using a custom high-speed, high-sensitivity CCD camera, Bahlmann et al. demonstrate frame rates at 640Hz in cardiac myocytes, a rate that corresponds to only 10-15 photons per pixel. Kim et al. implemented a confocal detection scheme with a PMT array to better reject scattered photons, improving maximum imaging depth from 30 μm to 75 μm in excised brain tissue (Kim et al., 2007).

An alternative approach is to use wide field or patterned illumination with wide field detection to image a region of interest. This can be achieved using spatial light modulators (SLMs), which are capable of shaping pulsed laser beams into arbitrary 3D patterns for the purpose of fluorescence excitation or photoactivation with precise spatial control (Nikolenko et al., 2008; Papagiakoumou et al., 2008).

Light sheet imaging. Light sheet microscopy is a conceptual extension of multifocal techniques, in which the number of foci used to parallellize excitation is increased until the entire sample plane is illuminated. However, unlike multifocal illumination strategies, the light sheet and the fluorescence it generates are oriented orthogonally with respect to each other. The orthogonal geometry is advantageous for some applications, such as embryonic

imaging, since all illumination light is meant to excite fluorescence and out-of-plane photodamage is minimized. However, the orthogonal requirement on excitation and collection geometry limits the types of samples that can be imaged. Most of the development of light sheet microscopy has been for single-photon fluorescence, in large part because of the non-linear relationship between two-photon excited fluorescence emission and excitation power. Generation of light sheets requires the use of low-NA objectives. From Equation 1.48, the two-photon efficiency has a quadratic dependence on NA. Truong et al. got around this power restriction by quickly scanning an excitation 'line' to produce a two-photon excitation sheet within the time required for a single camera frame acquisition (Truong et al., 2011). Planchon et al. demonstrated the use of Bessel beams to produce light sheet that could excite two-photon fluorescence (Planchon et al., 2011). Both of these techniques were used to visualize the development of embryos at high resolution and at speeds much faster than those achievable using single point scanning microscopy (Supatto et al., 2011).

Remote focusing. 'Remote focusing' generally refers to any method that alters the axial position by conditioning the beam before the objective rather than by physically translating the objective or sample (Botcherby et al., 2008b). Remote focusing not only enables fast 3D scanning, but also the ability to image the x-z plane or arbitrary oblique planes (Göbel and Helmchen, 2007).

The basic premise of remote focusing is simple. The divergence of the excitation beam is modified before entering the objective to change the effective focal spot in the sample. This can be done without introducing aberrations by placing a second identical objective at a plane conjugate to the back aperture of the imaging objective. A mirror at the focus of the remote objective is adjusted to produce a beam that, after reflecting back through the remote objective, is exactly conditioned to focus at any desired axial position (Botcherby et al., 2007, 2008a). Alternately, a simpler and more cost-effective method for varying beam divergence can be achieved through the use of a lens telescope if the application

does not require diffraction limited resolution (Grewe et al., 2011; Grosberg et al., 2012). Grewe et al. recently demonstrated this latter method using a variable lens telescope with an electrically tunable lens (ETL) element that can be added to most existing microscopes. Their scheme demonstrated that the usable axial range with the ETL was limited more by the imaging capability in scattering samples than by the focusing power of the ETL.

Temporal multiplexing. A parallelization approach utilizing temporal encoding to extract information from multiple depth planes was recently demonstrated by (Hoover et al., 2010; Cheng et al., 2011). For temporal encoding, the imaging beams must be separated into beamlets and temporally delayed with respect to each other, as well as conditioned to focus at different locations within the sample. Since lasers used for two-photon microscopy are typically pulsed, these delays cause the pulses to arrive at their respective focal depths at different times, such that the emerging fluorescence from each depth is temporally delayed by the same phase shift. Lock-in amplifier detection electronics are required to then isolate these temporally shifted signals and extract images from each layer. The main parallelization limit of temporal encoding is the lifetime of the fluorophores being imaged with respect to the laser repetition rate. For example, an 80 MHz laser has a 12.5 ns inter-pulse interval, so as many as 3-4 beamlets could be used if the fluorophores being measured had a lifetime of <3 ns. The actual degree of multiplexing possible would depend on the acceptable amount of overlap in the decay profiles of the emission. Available laser power for each beamlet will also limit signal to noise, and both illumination optics and detection electronics for signal demultiplexing need to be modified to implement this technique.

Spectral encoding. Most of the multiplexing strategies described here achieve parallelization at the cost of depth sensitivity or resolution. We have demonstrated a new imaging method capable of parallelizing laser scanning microscopy without fundamentally affecting resolution or penetration depth using spectral encoding. By focusing two or more beams

of different wavelengths at different positions within a suitable tissue, fluorescence or harmonic generation emissions from these regions can be uniquely separated. The development, characterization, and demonstration of this technique is discussed in detail in section 3.2.

3.2 Multiplane imaging using spectral encoding

The trade-off between imaging depth and imaging speed with multiplexing is a significant challenge. For applications in neuroscience, the deep tissue imaging ability of multiphoton microscopy is a major advantage, since small animal experiments can be performed in vivo. At the same time, imaging faster in 3D would allow a more complete view of dynamic activity. Practical considerations for in vivo imaging make many of the techniques described above in Chapter 3.1 difficult to implement. During an in vivo experiment, significant effort is made to ensure the animal is still. The animal is anesthetized, its head is secured, the cranial window is strongly affixed, and agar is used to stabilize the brain with respect to the window. Still, breathing and natural expansion and contraction of the living brain can introduce motion artifacts into imaging data. Random access techniques that only sample a subset of cells are extremely sensitive to this artifact. Full frame imaging helps to differentiate artifact from true signal, and therefore the development of a parallelization technique was guided with this constraint in mind.

3.2.1 Spectral encoding and linear unmixing

In order to use two (or more) excitation spots without impairing resolution, the spatial origin of the emerging fluorescence must be encoded in some way. While a single fluorophore will produce the same emission spectrum for different excitation wavelengths, a fixed-ratio mixture of two or more fluorophores can produce uniquely different emissions for a range of excitation light. By exploiting the unique emission properties of mixtures of dyes, parallelization can be achieved by using two excitation beams tuned to different wavelengths simultaneously focused into a sample. In some cases, filters can be used to cleanly separate the emission from the different excitation sources. In others, cross-talk between fluorescence detection channels requires linear unmixing to ‘decode’ the fluorescence.

In cases where separation cannot be achieved using filters, we can assume that the

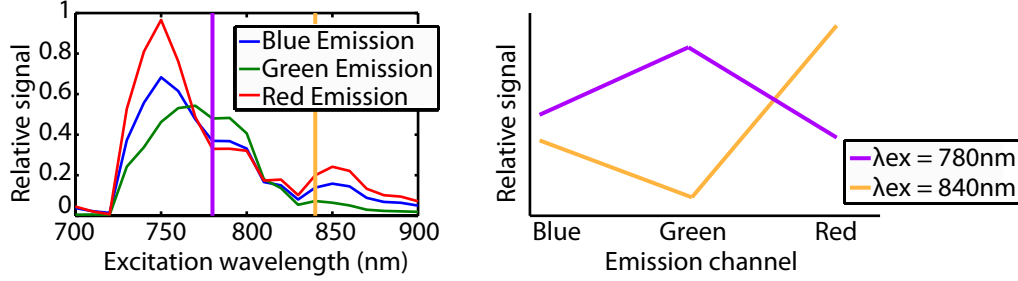


Figure 3.1: Left shows the excitation spectrum of a mixture of FITC-dextran and Texas red, dissolved in saline at a molar ratio of 1:18. Right shows the spectral signatures in the three channel detection of the dye combination at excitation wavelengths 780nm and 840nm.

measured signal in three different emission channels (M_B , M_G , and M_R) is equal to the linear combination of the emission signals of the fluorescent species excited by beams with excitation wavelengths λ_{ex1} and λ_{ex2} at positions $r_{\lambda_{ex1}}$ and $r_{\lambda_{ex2}}$. This relationship is given by Equation 3.1:

$$\begin{pmatrix} M_B(r_{\lambda_{ex1}} + r_{\lambda_{ex2}}) \\ M_G(r_{\lambda_{ex1}} + r_{\lambda_{ex2}}) \\ M_R(r_{\lambda_{ex1}} + r_{\lambda_{ex2}}) \end{pmatrix} = \begin{pmatrix} F_{\lambda_{ex1}B} & F_{\lambda_{ex2}B} \\ F_{\lambda_{ex1}G} & F_{\lambda_{ex2}G} \\ F_{\lambda_{ex1}R} & F_{\lambda_{ex2}R} \end{pmatrix} \begin{pmatrix} k(r_{\lambda_{ex1}}) \\ k(r_{\lambda_{ex2}}) \end{pmatrix} \quad (3.1)$$

where $F_{\lambda_{ex1}B,G,R}$ are the characteristic emission signals of the dye mixture measured with the laser at excitation wavelength λ_{ex1} , and $F_{\lambda_{ex2}B,G,R}$ are the dye mixture emission signals using the second laser at excitation wavelength λ_{ex2} . Coefficients $k(r_{\lambda_{ex1}})$ and $k(r_{\lambda_{ex2}})$ represent the relative weight of the detected signals originating from each excitation beam, for each scan location. Values for F can be extracted from initial scans acquired with only one of the lasers illuminating the sample. Figure 3.1 shows the excitation spectra of a combination of Texas Red and FITC-dextran. For dual beam imaging with spectral encoding, two excitation wavelengths λ_{ex} should be chosen so that the emission patterns from each respective wavelength differ, such as those shown in the right panel of Figure 3.1. These ‘spectral signatures’ represent $F_{\lambda_{ex1}B,G,R}$ and $F_{\lambda_{ex2}B,G,R}$ in Equation 3.1.

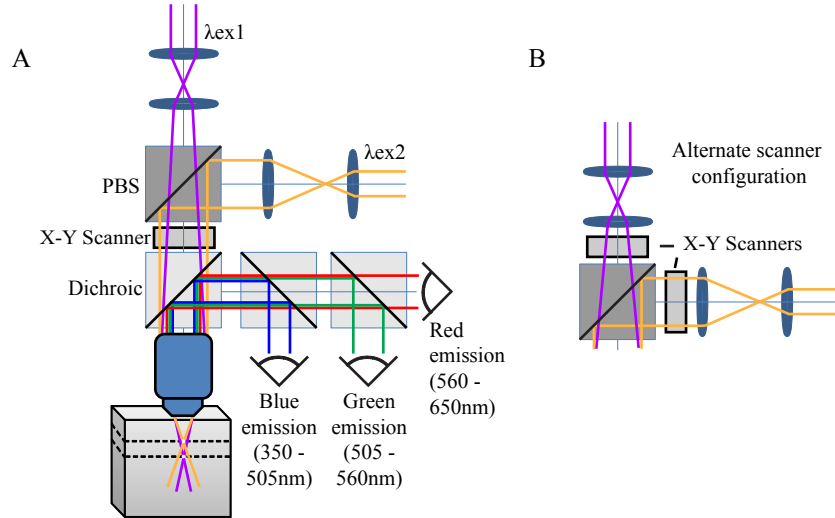


Figure 3.2: Optical layout for dual beam TPEF imaging. Two laser beams at different excitation wavelengths are focused simultaneously into the sample. Focus depth is controlled using lens telescopes to adjust beam divergence. The two excitation beams are combined before the scanning mirrors using a PBS cube. Three spectrally resolved detection channels measure fluorescence emission. A. A configuration where the beams are combined before raster scanning. B. The two beams can be scanned before combination to allow imaging at different speeds in addition to different spatial positions.

3.2.2 Instrument design for dual beam, dual plane imaging

The two-photon microscope described in section 2.2.2 was adapted to allow dual-beam imaging. A second tunable Ti:Sapphire laser (MaiTai HP, Spectra Physics) was added to the microscope. The second beam path has its own power monitoring and control, as well a lens telescope used to expand the beam and to facilitate remote focusing. The two beams were configured to have perpendicular polarizations, and were combined using a polarizing beam splitter (PBS) cube before galvanometric scanning mirrors, which were used to steer the beams in an x-y raster scan. Generated fluorescence was simultaneously collected by three spectrally resolved photomultiplier detectors, which were necessary in order to allow accurate linear unmixing. The remaining system components are described in Section 2.2.2. Average power at the sample was 50–100 mW, dependent on wavelength. The optical layout for dual beam imaging is shown in Figure 3.2.

With both lasers aligned through the objective, the collimation of each beam's tele-

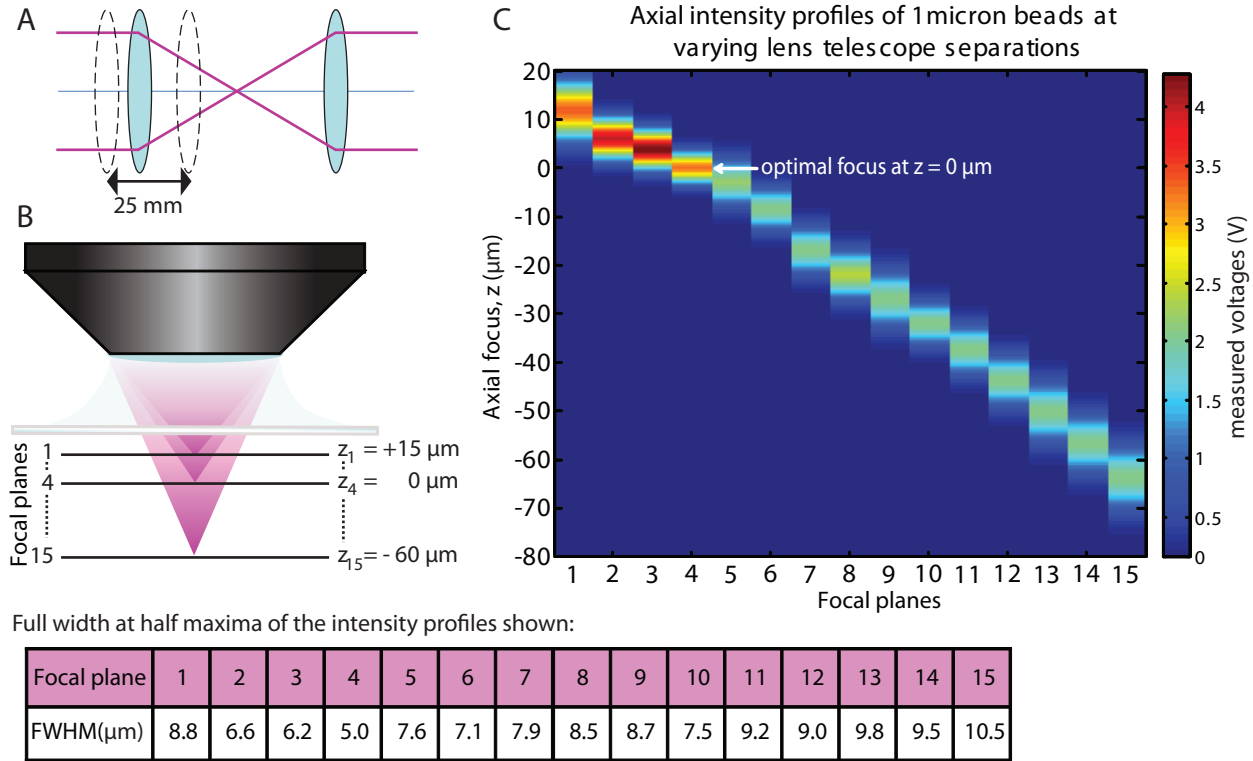


Figure 3.3: Characterization of axial resolution for remote focusing configuration. A. The first lens in the lens telescope located before beam combination was translated 25mm to create focal planes 1-15. The focal lengths of both lenses in the telescope were 30mm. B. Schematic of focal planes, separated by $75 \mu\text{m}$. Shallow (planes 1-3) and deep (planes 5-15) focal planes correspond to converging and diverging light entering the objective, respectively. C. Axial intensity profiles of $1 \mu\text{m}$ beads at each focal plane demonstrate the optimal focus and that intensity deteriorates for ‘negative’ focal planes.

scope was adjusted so that each laser would focus at a different point along the axial dimension. An infinity-corrected microscope objective is optimized for creating a focal spot with collimated light entering at the back aperture of the objective, but if the light entering the objective is slightly converging or diverging, the beam will focus at a closer or further distance from the sample surface, respectively. In this configuration, the maximum achievable axial separation of the two imaging planes was limited by deterioration in axial resolution as the light entering the back aperture of the objective became less collimated. Characterization of the axial resolution of this imaging configuration is shown in figure 3.3. Beam integrity could be better preserved using remote focusing via a second objective (Botcherby

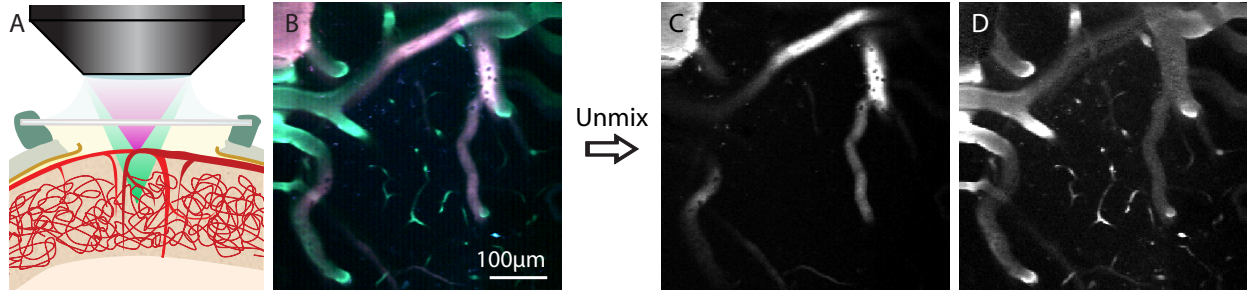


Figure 3.4: A. In vivo imaging configuration where one beam is focused in the plane of larger surface vessels while the second is focused in the plane of deeper diving vessels and capillaries. B. Raw RGB emission image seen when both planes are imaged simultaneously using two excitation wavelengths. C-D. Images after unmixing show that the fluorescence signal from the two planes can be separated using linear unmixing.

et al., 2007) or by using adaptive optics.

Figure 3.4 demonstrates how this technique can be used experimentally. In this example, the dye combination described by Figure 3.1 was injected into the tail vein of a rat to provide contrast for vascular imaging in vivo. The excitation wavelengths used were 780 nm and 840 nm, focused at independent planes in the intact brain, as shown in Figure 3.4A. These wavelengths were chosen based on the excitation-dependent emission spectra of the dye combination such that fluorescein fluorescence dominated blue and green emissions at 780 nm excitation, while Texas Red fluorescence dominated red emission at 840 nm excitation. Panel B shows the RGB emission image acquired when both planes were imaged simultaneously. Images of k are shown in Figure 3.4C and D. These values were extracted from data in 3.4B by solving equation 3.1 using a non-negative least squares fit for every pixel.

3.2.3 Application: resting-state hemodynamics

To demonstrate the benefits of our approach, we implemented this system for in vivo acquisition of high-speed vascular dynamics in the living rat brain.

Biological context and relevance. Blood flow changes in the brain underlie the signals detected by functional magnetic resonance imaging (fMRI). However, the mechanisms mediating stimulus-induced changes in blood flow remain poorly understood, making interpretation of fMRI signals in terms of underlying neuronal activity a significant challenge (Attwell et al., 2010). In addition to stimulus-evoked responses, the popularity of the fMRI technique of functional connectivity mapping (FCM) or ‘resting state analysis’ has increased in recent years. FCM harnesses baseline fluctuations in blood flow in the absence of deliberate stimulation to infer the connectivity of different brain regions based on the temporal synchrony of their hemodynamic fluctuations (Fox and Raichle, 2007; Fox et al., 2005). While this technique has revealed a surprising range of patterns or ‘networks’ in the resting brain, its underlying neurovascular basis has barely been explored. This is all the more important given the compelling changes in resting-state networks that have been observed in a host of pathologies including autism (Anderson et al., 2011; Noonan et al., 2009), schizophrenia and Alzheimer’s (Garritty et al., 2007; Sanz-Arigita et al., 2010; Supekar et al., 2008). One critical question is whether the changes in blood flow observed in the ‘resting brain’ are generated via the same mechanisms and pathways as stimulus-evoked changes in blood flow, or whether components of observed blood flow changes could result from innate fluctuations in the vasculature itself.

Several recent studies have explored propagation of vasodilation in the cortical vasculature during somatosensory stimulation, to determine the likely neurovascular mechanisms controlling evoked changes in blood flow (Chen et al., 2011; Tian et al., 2010). Tian et al. used two-photon microscopy to sequentially scan different vessel segments during repeated stimuli, concluding that dilation initiates in deeper layers and propagates retrograde towards the cortical surface. The difficulty with studying this effect in spontaneous dynamics is that the same dynamics cannot be reproduced for sequential measurements. It is necessary therefore, to be able to acquire signal simultaneously from two different depths with sufficient

signal to noise to determine the depth-resolved propagation dynamics within a single spontaneous fluctuation. Here, we demonstrate the use of our new method for acquiring in vivo two-photon data that captures two depths simultaneously, allowing two layers of the brain to be monitored in parallel with no trade-off between resolution and speed. We demonstrate this technique by imaging the depth-dependent vascular dynamics of spontaneous fluctuations in rodent cortex.

Animal preparation. Three Sprague Dawley rats (208-348g) were surgically prepared under isoflurane anesthesia as described in (Chen et al., 2011) to allow manual ventilation via tracheotomy, continual monitoring of intra-arterial blood pressure, and intravenous alphachloralose anesthesia during imaging ($40 \text{ mg kg}^{-1} \text{ h}^{-1}$). A cranial window was formed over the somatosensory cortex by removing the overlying skull and dura, adding a drop of 0.5% agar in artificial cerebrospinal fluid, and then rigidly securing a glass coverslip over the area using dental acrylic (Henry Schein). Around 0.3ml of a 2:5 dye combination of dextran-conjugated fluorescein (FD2000S, Sigma-Aldrich, 0.025 mM in saline) and dextran Texas Red (D1830, Invitrogen, 0.18 mM in saline) was injected via femoral cannula to provide vascular contrast. The animal’s head was affixed in a stereotaxic frame throughout cranial surgery and imaging.

TPLSM imaging parameters. Single frame images displayed are 400×400 pixels, and were acquired at 2.5 frames/s. For fast acquisitions, 300×200 pixel images were acquired at 16 frames/s, or 250×250 pixel images at 6.4 frames/s, both of which correspond to a $500 \times 500 \mu\text{m}$ field of view. Image sequences were acquired for 20-30 seconds. For basic visualization of acquired images, RGB merges were created using data acquired with the three emission channels, with each channel scaled to its maximum after thresholding out the highest 0.1% of pixels. Single-laser 3D stack images (400×400 pixels every $3 \mu\text{m}$ over $150 \mu\text{m}$ in z) of the same region were subsequently acquired to record the local vascular morphology, and volume

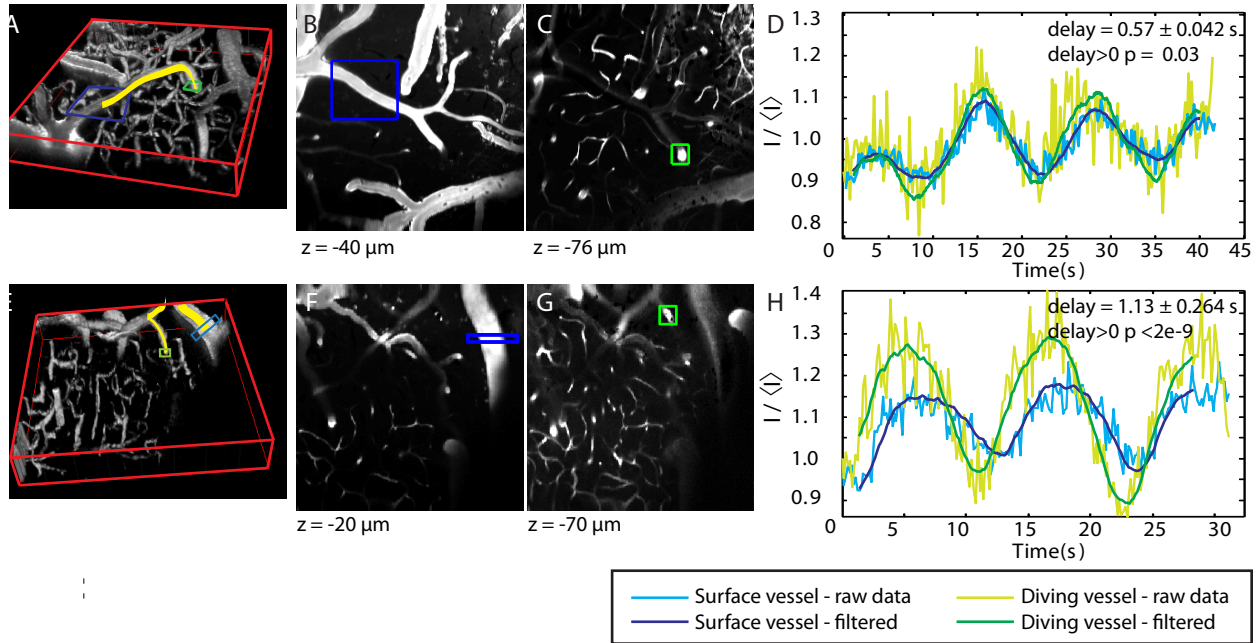


Figure 3.5: Vascular imaging in two planes shows that baseline fluctuations in vessel tone propagate towards the cortical surface. All fields of view are 500 μm across. (A) Volume rendering of the regions displayed in sections B-D. Yellow highlight shows the path along the vessel connecting the sampled regions. (B) Image corresponding to the shallower plane excited at 840 nm after spectral unmixing. The image area contained in the blue square was averaged at each time point to yield the intensity fluctuations shown in D. (C) Image corresponding to the deeper plane excited at 780 nm after unmixing. The image area contained in the green square was averaged at each time point to yield the intensity fluctuations are shown in D. The two planes in B & C were separated by 36 μm . (D) Oscillations in intensity of regions selected from unmixed data in B & C correspond to fluctuations in vessel diameter (temporally unfiltered and window-filtered data are both shown). (E-H) Data from a second rat showing similar oscillatory patterns in surface and diving vessels. The two planes sampled were separated by 50 μm .

renderings were made using ImageJ. Images of the two measured planes were also acquired with each of the excitation lasers individually to provide the spectral bases (F) for unmixing using Equation 3.1. Dynamic data sets were spectrally unmixed to generate separate image sequences the two simultaneously imaged planes.

Results. Our measurements simultaneously captured resting-state modulations in the diameters of surface and diving arterioles in the brain. By plotting intensity fluctuations averaged around selected vessels, we observed that both shallow and deep vessels exhibit similar variations, but with a marked phase delay. The delays reported were along the same vessel, which we verified by imaging depth stacks. Using cross-correlation analysis, we found that changes in tone in deeper vessels preceded changes at the surface in all cases ($n = 3$ rats, 38 runs, $p < 7 \times 10^{-7}$), suggesting deep-to-shallow propagation of a vasomodulatory signal. Since these fluctuations are spontaneous, the depth-dependent phase shifts observed in our measurements could not be studied with sequential scans, suggesting that our spectral encoding approach could be valuable for studying spontaneous dynamics in both vascular and neuronal cortical networks. Figure 3.5 shows results obtained in two different rats.

Since we can study dynamics anywhere within the two planes imaged, we further explored the timing of signals in many locations in the planes. Figure 3.6A and B show correlation maps that reveal the amplitude of the maximum correlation (for the optimal phase shift) between every pixel relative to the seed region indicated in the superficial plane, thresholded at a significance of $p < 0.01$. To calculate the phase delay of the time courses from different regions, extracted signals were window-filtered and then their cross-correlation with respect to each other was calculated. This approach gives correlation values for all positive and negative phase lags. The delay reported for each measurement is the phase shift value corresponding to the maximum point of the cross-correlation. Each calculation was done for a single trial, and phase delays over multiple runs were averaged for statistical analysis. For the correlation maps displayed in Figure 3.6, correlation coefficients were calculated

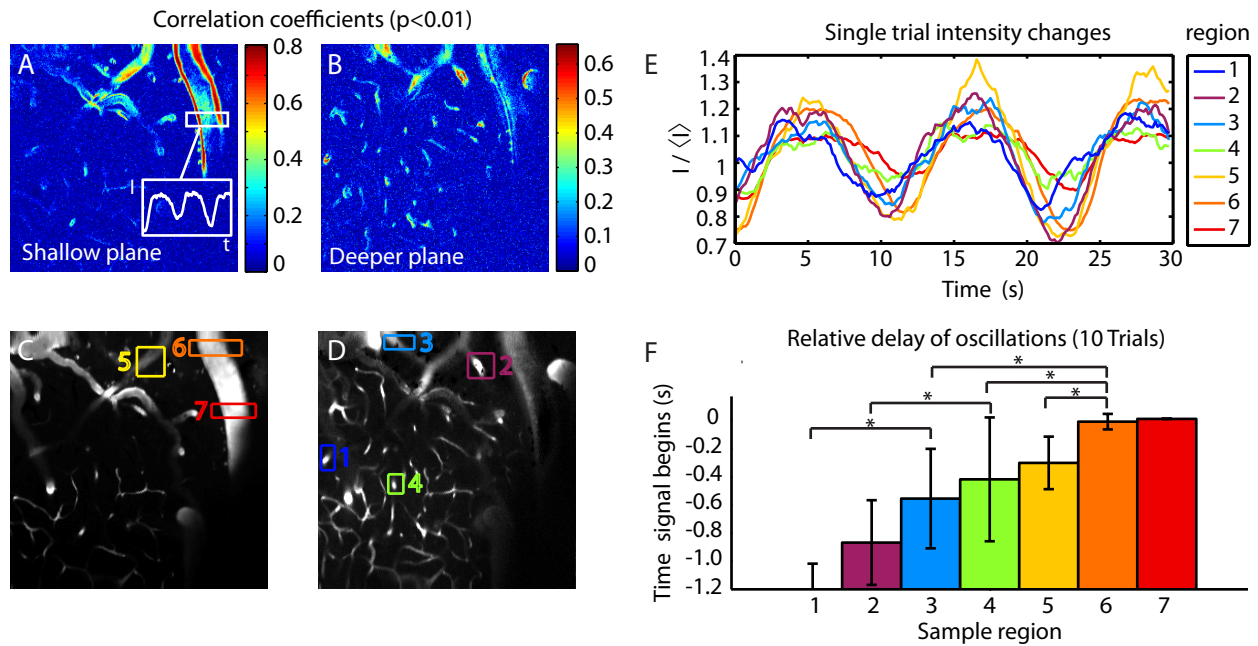


Figure 3.6: Multi-region timing analysis of different locations along a vessel branch. (A-B) Correlation maps of the time-course of each pixel in the shallow and deep planes with respect to the intensity time-course shown in the inset in A extracted from the superficial region indicated. Only significant correlation coefficients ($p < 0.01$) are displayed. Fields of view are $500 \mu\text{m}$ across. (C-D) Colored and numbered boxes indicate the regions analyzed in the shallow and deep planes, chosen based on the locations with strong correlation coefficients on correlation maps in A and B. (E) Intensity values over time of the seven regions shown in (C) and (D). (F) Temporal delays with respect to region 7, calculated from cross-correlation analysis (such that region 1 was the earliest to change). Values shown are the mean of 10 trials, with error bars showing one standard deviation above and below the mean. Region 7 has no error because for each trial, the delay to itself was necessarily zero. Groups with significantly different means ($p < 0.05$) are indicated by *.

after signals had been shifted by their estimated phase delay. Maps displayed are averaged correlation maps from 10 trials.

These maps indicate that the strongest correlations are seen in arteriolar segments, with only very small correlations observed in pixels corresponding to venules and capillaries, consistent with blood flow being modulated by active arteriolar dilation and constriction. Timecourses from the vessel segments with the highest correlation coefficients, as indicated in Figure 3.6C and D, were then extracted as shown in Figure 3.6E. From the phase lags between these different signals, it is possible to determine the order of dilation of vessels located in both layers measured, as indicated in Figure 3.6F. As before, all vessel segments in the deeper layers can be seen to precede changes in superficial vessels.

While the sequence of onsets is consistent with a wave of arteriolar dilation propagating from deeper to more superficial layers, analyzing data from multiple rats, runs and regions, we found that temporal delay was not linear with respect to either axial separation, or the 3D distance traveled along the vessel between sampled regions (for example, along the highlighted vessel path in Figure 3.5A,E). While we still expect that vasodilatory signals are propagating along the vascular network itself, this result suggests that signal propagation speeds could be affected by vessel diameter, or organization of the vascular tree between sampled regions.

Method validation. The quantified changes in vessel tone, as displayed above, are intensity fluctuations in pixels surrounding selected vessels that were averaged as a function of time. This approach is demonstrated to provide equivalent results to calculation of the full width half maximum of vessel segments in Figure 3.7. The relative delay between the superficial and deep regions was calculated for full width half maxima (FWHM) versus signal intensity to be 0.9374 s and 1.0938 s, respectively. We conclude that the two approaches give almost identical results, and therefore chose to use intensity-based analysis to avoid the confounds of calculating FWHM for all irregularly shaped vessel segments, and to enable

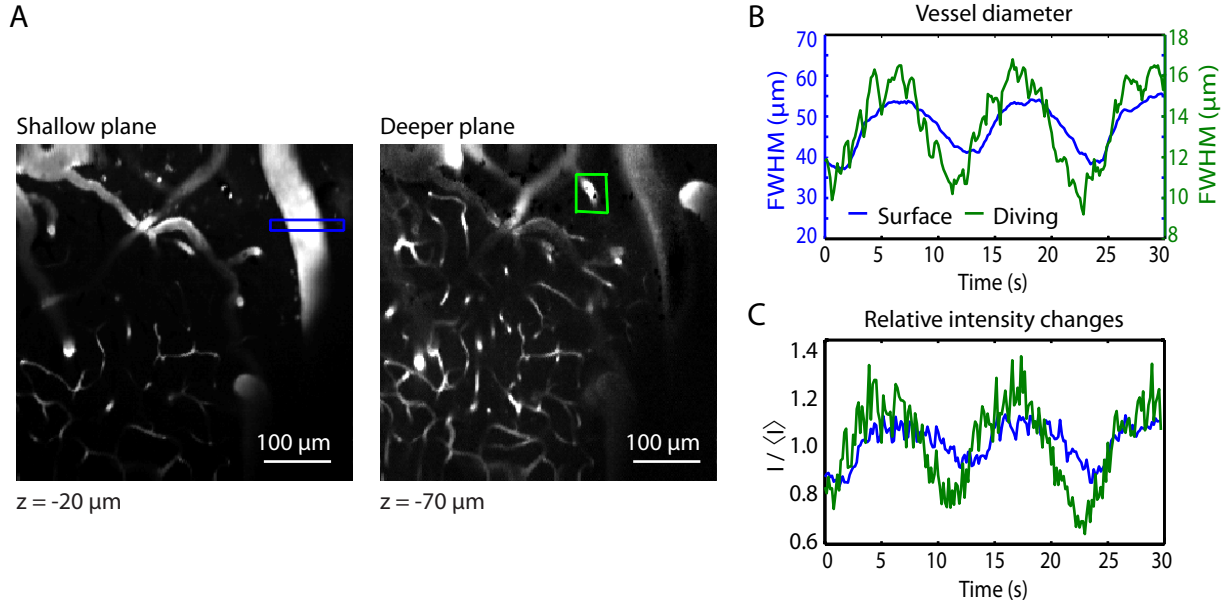


Figure 3.7: Comparison of calculation of vessel FWHM to intensity fluctuations. A. Images show the superficial and deep planes imaged simultaneously, and the two segments examined for this comparison. B. The time-course of the FWHM variation of these two segments. C. Shows equivalent fluctuations in the signal intensity extracted from the same regions as in B.

calculation of the correlation coefficients for each pixel as shown by the maps in Figure 3.6A and B.

To validate of the spectral unmixing, the residuals of the non-negative least squares fit were examined in two cases. Figure 3.8 shows results of the validation. The upper and lower panels show vessel sets that have been imaged at two planes simultaneously using spectral encoding and linear spectral unmixing. Measurements from three emission channels acquired using a single laser excitation source are shown in A and F. Values from these images are used to provide the basis spectra (F from Eq 3.1) in the linear unmixing. Raw data (M) acquired in 2 planes simultaneously is shown in images B and G, and the coefficients to the linear fit (k) are shown in C and H. The unmixed images were compared to single laser images to ensure cross-talk was minimized. I and J are the square roots of the sums of residuals for each measurement divided by the maximum raw data value in the image. Plots show the raw data and the computed linear fit for regions in the residual images that showed

error. The R-squared value for these example regions is given as a measure for the goodness of fit. The correlation between the real data and the fit is very good.

3.2.4 Summary

In summary, we have introduced a new imaging method capable of parallelizing laser scanning microscopy without cost to resolution or penetration depth using spectral encoding. This approach was applied to measure the relative timing of resting state vascular changes in the living rat brain, revealing that, as with stimulus-evoked changes in arteriolar tone, fluctuations initiate in deeper layers before propagating to superficial pial arterioles.

Our spectral encoding technique is ideal for studying vascular dynamics, since dye combinations compatible with the method can be readily introduced to the cardiovascular system. However, this approach could also be extended to applications that use calcium imaging through the use of multiple calcium sensitive dyes with different excitation-emission properties. This would allow monitoring of neuronal activity of multiple layers in parallel. It would also be possible to image the vasculature of the brain at a superficial depth, along with calcium activity in neurons at deeper depths, using two spectrally-distinct dyes (e.g Texas red dextran for vascular imaging and Oregon Green BAPTA-1 AM for calcium imaging). In this case, it would be necessary to choose appropriately different excitation wavelengths to excite Texas red superficially, and Oregon green at depth, such that the majority of signal acquired in the green emission channel would be from the deeper layer, while signal detected in the red channel would be from the more superficial vasculature.

This technique is limited in the number of regions it is able to image simultaneously by a number of factors. The first is the ability of dyes to produce unique emission spectra when excited at different wavelengths. Single fluorophores will typically generate the same emission spectrum irrespective of the wavelength used to excite the molecule; however this changes if the target fluorophore is composed of a mixture of two or more types of molecules.

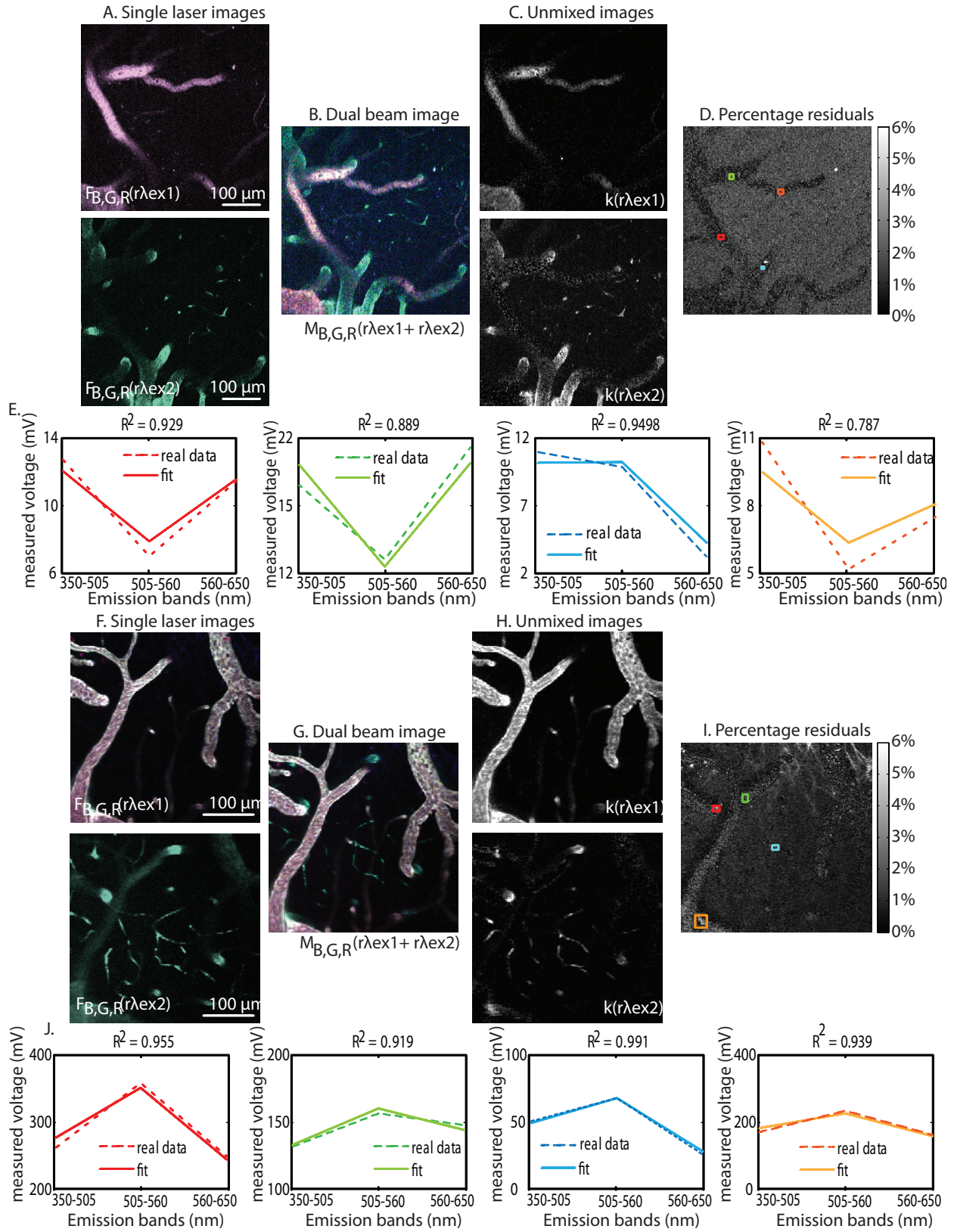


Figure 3.8: Validation of the dual plane unmixing method.

Parallelization could be improved by increasing the number of spectrally resolved detection channels, although dye combinations would still need to be carefully considered. Practical limitations on parallelization also include the availability of sufficient laser power at suitably different wavelengths for imaging.

Benefits of this approach include the ability to perform this technique using any system with dual laser sources, with almost no other required hardware changes. The two or more beams could be steered either together, e.g. via a single galvanometer mirror set, or independently (at the same, or different depths) to acquire data from arbitrarily different regions such as a single cell at high spatial resolution, as well as the full field of view at lower spatial resolution. In microscopy systems with sufficient sample rates, regions could even be sampled at different effective frame rates. Steering of one or both beams could also be performed by acousto-optic deflectors, digital mirror devices or spatial light modulators. Multibeam spectral encoding is compatible with two-photon imaging as well as with other nonlinear microscopy approaches (discussed in section 3.3), and could also be applied in confocal microscopy setups.

3.3 Multiplexed SHG microscopy with spectrally resolved detection

The narrow band signals generated by second and third harmonics make S/THG microscopy a natural application for our spectral multiplexing strategy. With the correct light sources and detectors, almost unlimited spectrally narrow harmonics could be generated and easily separated based on wavelength, without requiring spectral unmixing algorithms as was needed for multiplexed fluorescence microscopy. In this section, the direct extension of dual-plane imaging to SHG is presented. Methods to further parallelize SHG imaging are discussed in terms of the necessary excitation and detection sources, and proof of principle results are shown that were acquired with our current equipment.

Multiplexed SHG microscopy could allow very high-speed volumetric imaging. The development of exogenous SHG contrast enhancing dyes or markers would be particularly useful for this application, since intrinsic SHG contrast only comes from particular structures and can be weak. Voltage enhanced SHG signal has been used to measure membrane potentials using the styryl dye FM4-64 and retinal analog AM-4 (Theer et al., 2011; Jiang and Yuste, 2008). Nanocrystals displaying high SHG contrast can be used as *in vivo* probes (Pantazis et al., 2010) that do not photobleach. Recently, surface functionalization of such particles has been shown to allow molecular specificity (Ćulić Viskota et al., 2012; Hsieh et al., 2010). Coupled with multiplexed SHG, functionalized SHG probes could be powerful tools for volumetric imaging.

3.3.1 Extension of dual plane spectral encoding to SHG microscopy

As a first step, the dual plane imaging setup presented in Figure 3.2 was converted for SHG imaging by swapping out the filter set in front of the PMTs to isolate the narrow harmonics. The two detection channels had 10 nm bandpass filters with center wavelengths

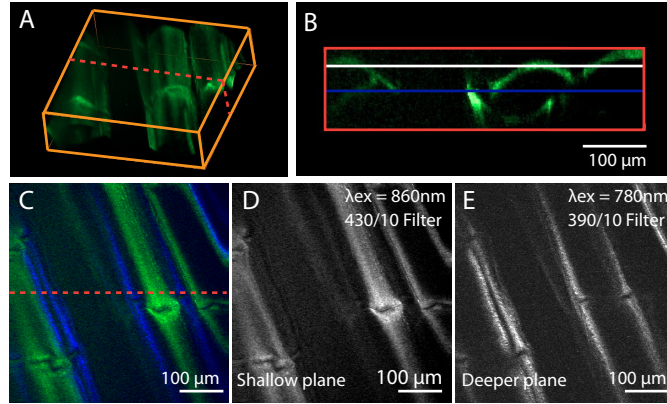


Figure 3.9: Dual plane SHG imaging. (A) 3D rendering of a post-mortem small fish tail, imaged using 860 nm excitation with a 430/10 filter for detection. (B) Cross-section of volume (at dotted line in A and C) shows the imaging planes of the two beams, positioned 36 μm apart. (C) Raw RGB image recorded with both lasers. Excitation wavelengths were 860 and 780 nm for the upper and lower planes, respectively. 390/10 emission is color coded blue, 430/10 emission is color coded green. (D) Channel containing SHG signal from upper level ($z = -30 \mu\text{m}$) and (E) channel containing SHG signal from lower level ($z = -66 \mu\text{m}$), both with no unmixing.

at 390 nm and 430 nm for SHG imaging at 780 nm and 860 nm, respectively. A dichroic mirror (Di01-R405-25x36, Semrock) was used to separate the harmonic signals from each excitation laser and direct to its respective PMT. Dual plane imaging of SHG contrast from the tail of a small first (post-mortem) is shown in Figure 3.9. Again, the separation of planes required no unmixing.

By functionalizing SHG probes to serve as vascular tracers, similar experiments to the ones done in the previous section could be achieved. SHG probes have the potential to be brighter and more stable than fluorophores (Cohen, 2010). Additionally, since the SHG signal is dependent only on the incident wavelength, a careful combination of fluorophores would not be needed and further multiplexing is much more feasible.

3.3.2 Parallelization of SHG microscopy to more than two foci

To further parallelize SHG imaging, multiple excitation wavelengths and spectrally resolved detection are required. Clearly, it is not reasonable to continue parallelization by adding laser

sources. Instead, we would like a single, pulsed source with multiple excitation wavelengths. Two ways to do this are to use a supercontinuum source or fiber or to leverage the spectral output of the pulsed Ti:Sapphire laser typically used for multiphoton excitation. Detection requirements include low-light sensitivity and the ability to spectrally separate the SHG signal. The spectral resolution required at the detector depends on the excitation source. For example, a spectral bandwidth of 40 nm would produce second harmonics with a range of 20 nm, since each incident wavelength doubles its frequency. Requirements for the excitation and detection side are discussed.

The pulse width of a laser is inversely proportional to its spectral bandwidth. Thus, narrow pulsed lasers contain a spread of wavelengths around a central wavelength. The spectral bandwidth of our Ti:Sapphire laser was measured to be 10 nm with a central wavelength of 800 nm. By spatially separating the available wavelengths in a single laser beam, we hypothesized that we could multiplex the SHG imaging.

In order spatially separate the wavelength components of the excitation beam, we inserted a blazed transmission grating into the beam path. Blazed transmission gratings are designed to efficiently direct for specific wavelengths into the first diffracted mode (Newport, 2011). The efficiency of blazed gratings drops off sharply for dense gratings (>600 grooves/mm), therefore we chose a grating with 300 grooves/mm, 31.7° Blaze angle (Thorlabs, GTI25-03A). For wavelengths 700-900 nm, above 65% of the light goes into the first diffracted mode with maximum efficiency at 800 nm. The diffracted angle after the grating is given by

$$d[\sin\theta_i + \sin\theta_m] = m\lambda \quad (3.2)$$

where d is the groove spacing in units of length^{-1} , θ_i and θ_m are the incident and diffracted angles, respectively, m is the diffracted mode, and λ is the wavelength. The maximum efficiencies quoted above occur when $\theta_i = 0$, but this results in a minimum for the angular diffraction. Therefore, there is a trade-off between the efficiency of the optical setup and the

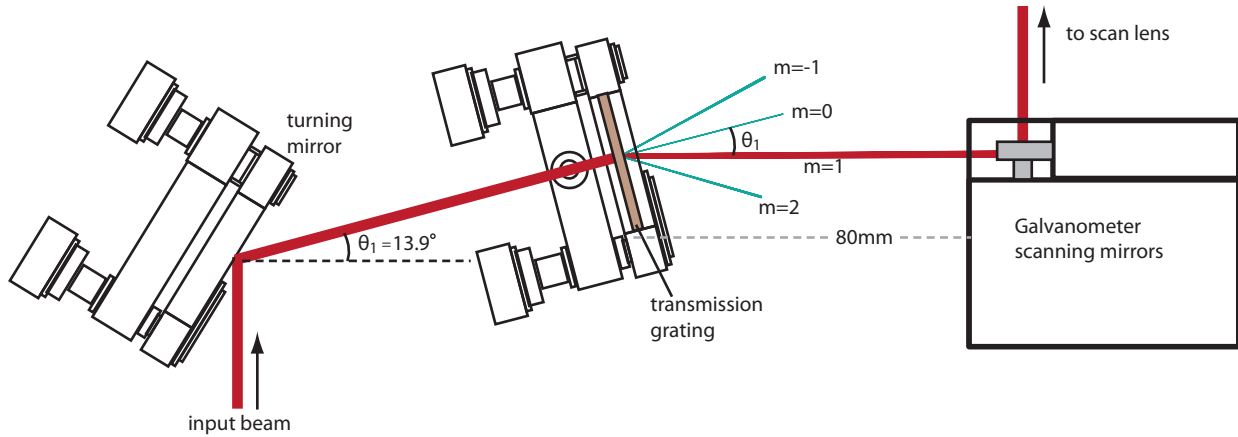


Figure 3.10: Optical layout for the spatial separation of excitation wavelengths using a transmission grating.

amount of spatial separation we could expect at the focal plane.

Figure 3.10 shows the optical layout that was implemented to achieve spatial separation of wavelengths at the focal plane. The red lines represent the excitation laser beam as it travels through the transmission grating, the scanning mirrors, and then through the remaining optical elements. The drawing is to scale, and the diffracted angle θ_1 is 13.9° for $\lambda = 800$ nm. The grating was placed close to the galvo mirrors to preserve the telecentric focusing capability of the objective. This requirement limits the achievable separation of wavelengths at the focal plane.

In order to estimate the spatial separation of the diffracted wavelengths at the focal plane, a ray trace model using the optical design software OpTaliX-LT was created. Figure 3.11 shows the model which includes the ‘unfolded’ light path from the transmission grating, through the scanning mirrors, scan lens, tube lens, and Olympus 20x water immersion objective lens. Beam turning at the scanning mirrors and at a turning mirror between the scan and tube lenses is not included. The scan lens used in the OpTaliX model was a 1“ diameter achromat with a 50mm focal length (Edmund Optics, 45-803) and the tube lens was an achromat with $f=180$ mm (Thorlabs, AC508-180). It should be noted that these are substitutions for true scan and tube lens pair used in our system. A 2” diameter achromat

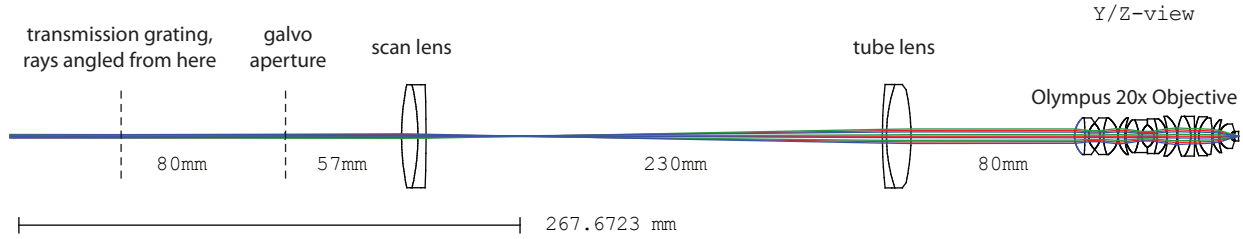


Figure 3.11: OpTaliX model for the scan system beginning with a transmission grating to spatially separate excitation by wavelength and ending with the objective lens. Distances are drawn to scale and match actual instrument parameters.

(same focal length) from Melles Griot is actually used as a scan lens, but since this lens was discontinued, the prescription data for the lens was not available. The tube lens is part of an Olympus trinocular assembly, and the lens data are not made public for proprietary reasons. The achromat from Thorlabs was substituted since it was a similar focal length. Lens data for the 20x Olympus objective lens was obtained from patent literature.

In the model, rays are aimed at a 3mm aperture representing the grating and the beam width before the scanning mirrors. Although the diagram is linear, both the angle and wavelength of the light can be specified using OpTaliX in order to accurately represent the light behavior after the grating. The angle of the propagating light relative to the optical axis is altered after the grating, and this angle can be calculated using Equation 3.2. Using this equation, the angular spread for wavelengths 795-805 nm (representing the 10 nm FWHM measured bandwidth for a central wavelength of 800 nm) is 0.1773° . Therefore, rays were oriented at $\pm 0.089^\circ$ after the grating in the model. A ray intersection plot at the focal plane is shown as Figure 3.12 for rays propagating through the system in this way, showing an expected separation of extreme wavelengths within a laser pulse to be about $7.8 \mu\text{m}$. Results using this model showed chromatic aberration that caused wavelength-dependent separations at the focal plane, and focal planes that varied several microns in z (using wavelengths spanning 780-900nm). Such marked shifts in focal depth are not observed in our system during normal imaging since the objective and tube lens pair are carefully corrected for good performance over the specified wavelength range. We suspect this disparity between

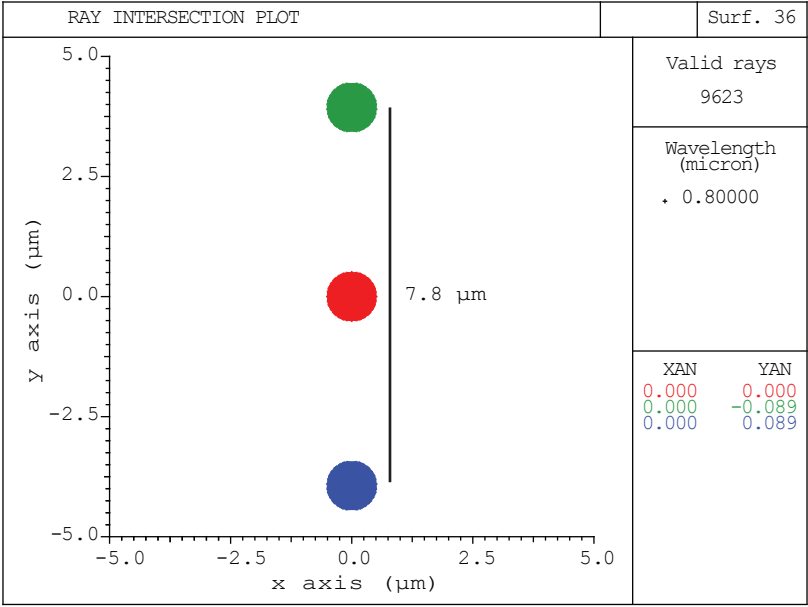


Figure 3.12: Spatial position of wavelengths at the focal plane for wavelengths contained in a pulsed laser at a single central wavelength, separated using a transmission grating.

the model and actual performance results largely from incorrect prescription data for the tube lens, however the model does serve to estimate the outcome.

To experimentally confirm the model and, more importantly, the feasibility of this approach for multiplexing, spectrally resolved detection is required. This is challenging for our application since the bandwidth of the SHG signal that results from a laser pulse is only 5 nm, which requires a spectrometer with high spectral resolution and similar sensitivity to the PMT normally used for detection. Detection options include cooled CCD or PMT arrays coupled with a high-efficiency grating spectrometer (such as the iHR320 Imaging Spectrometer, Horiba, which can have spectral resolution as fine as 0.1nm), or else long integration times to improve signal for less sensitive devices.

3.3.3 Proof of principle demonstration

To test how the ray trace model predicts actual image shifts in our system, the laser was aligned through the transmission grating as shown in Figure 3.10. Using the blue PMT

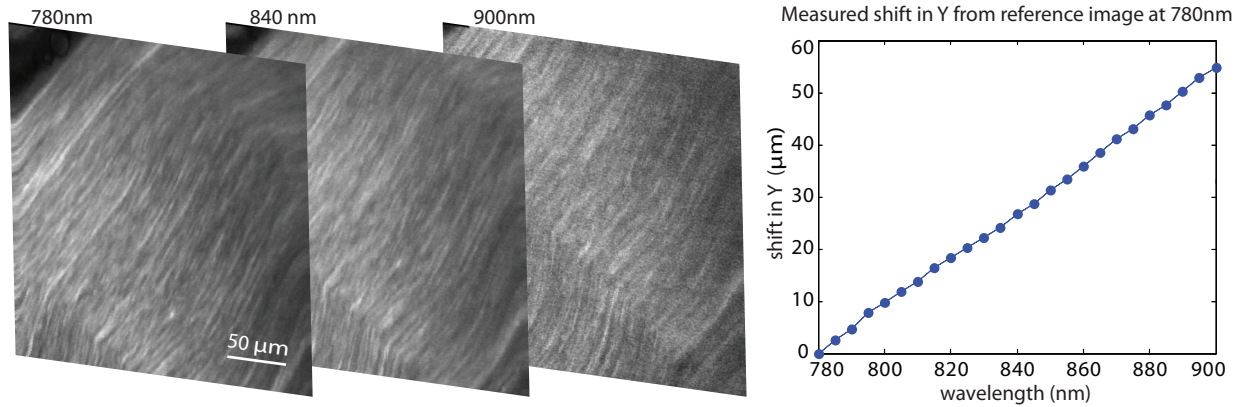


Figure 3.13: Measured image shift for varying central wavelengths. SHG images of fibrous collagen extracted from the tail of a rat and immersed in saline.

detection channel (350-505 nm) to measure SHG signal from all wavelength components of each specified excitation, the laser wavelength was scanned from 780 to 900 nm in 5 nm increments to image SHG from fibrous collagen. The collagen sample was taken from the tail of a rat, placed on a microscope slide and immersed in saline, covered with a coverslip and imaged with the water immersion 20x objective.

Images in Figure 3.13 confirm that the scanned region shifts with excitation wavelength. To quantify the shift, 2D Fourier transforms were performed on each image and the x and y components of the spatial frequencies were cross-correlated between consecutive images. The position of the cross-correlation peak was used to determine the number of pixels to shift an image relative to a reference image such that the two are registered. The shift in microns was computed based on the scale of the 400x400 pixel image. The measured shift in the images from 780 to 900 nm was 55 μm and the mean shift between consecutive images at central wavelengths with 5 nm spacing was 2.3 μm . These values are smaller than the shifts predicted by the ray trace model, which were 90 μm and 7.8 μm , respectively. As noted above, the difference in the model and actual performance is likely a result of aberration corrections in the lens system not accounted for by the lens substitutions made for the model.

Based on the data in Figure 3.13, the expected spatial separation that can be obtained at the focal plane (for this optical geometry) by separating the wavelengths contained in the 10 nm spectral bandwidth of the Ti:Sapphire is less than 5 μm . Therefore, in order to properly discriminate detected SHG signal from an image scanned with this spatio-spectral patterning, an image with both high spatial and spectral resolution is required. The optical resolution limit is well under 5 μm . However, spatial resolution for scanning microscopes is limited by the quantity of pixels in addition to the optical resolution limit, so an image with dense sampling is needed to ensure multiple pixels are captured across the 5 μm excitation wavelength spread. Images shown in Figure 3.13 are sampled at one pixel per 1.25 μm , enough to discern the spatial excitation pattern. Since the goal is ultimately to improve imaging speed through parallelization, high speed data acquisition is an important consideration. The images in Figure 3.13 contain 160000 pixels to achieve adequate spatial resolution, acquired at a rate of 400 kHz for usable frame rates of 2.5 frames/s. Spectrometers with long acquisition times (which would correspond to slower pixel acquisition rates) will not suffice as detectors for fast imaging.

A spectrometer with sufficient spectral or temporal resolution to accurately measure SHG resulting from the Ti:Sapphire laser was unavailable. Therefore, in order to show that SHG signal from output of the laser tuned to one central wavelength can contain spectrally encoded spatial positions, a dichroic filter was used to separate measured signal from the wavelength components of the excitation source split between two PMT detectors. In the following discussion, λ_{ex} is used to denote laser wavelength and λ_{SHG} is used to denote the wavelength of measured signal. The transmission characteristics of the dichroic filter around the cutoff wavelength (for discriminating λ_{SHG}) are displayed in Figure 3.14A. Detection channel 1 captures most of the signal for wavelengths $\lambda_{SHG} < 410$ nm, and detection channel 2 captures signal for $\lambda_{SHG} > 420$ nm. For the wavelengths in between $410 \text{ nm} < \lambda_{SHG} < 420$ nm, the filter cannot cleanly separate SHG signals, and there is cross-talk between the

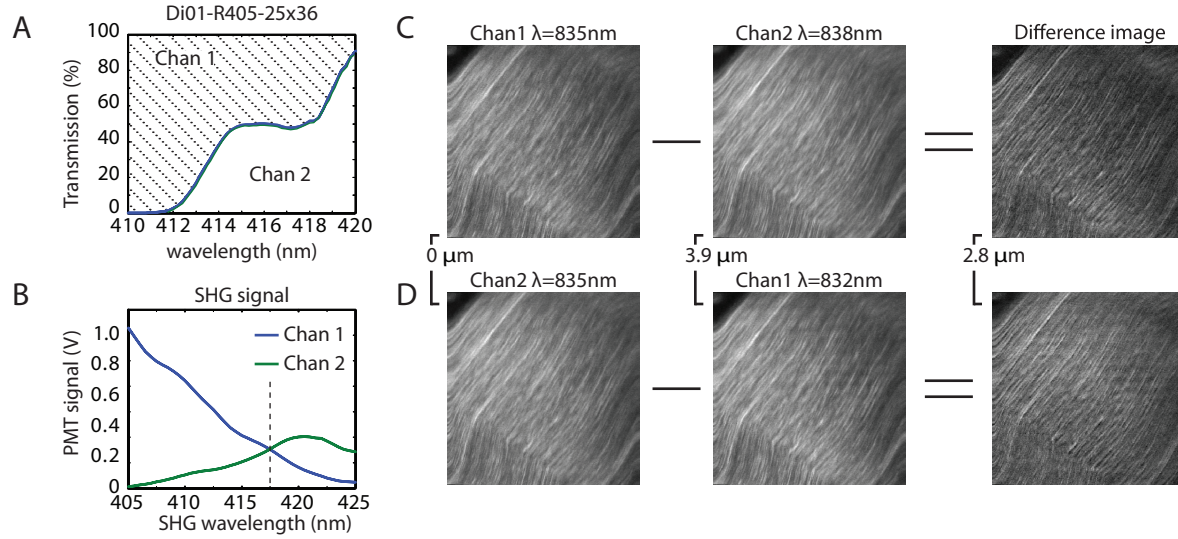


Figure 3.14: A. Spectral characteristics of the dichroic filter used to separate the two detection channels. There is cross-talk around the cut-off wavelength of the filter. B. The average signal in each image obtained by channels 1 and 2 while scanning the excitation wavelength λ_{ex} . SHG wavelengths λ_{SHG} are given as half the excitation wavelength used to generate the image. C & D. SHG images in the two channels at $\lambda_{ex} = 835$ nm are equivalent. Image subtraction is used to demonstrate spatial separation of images from the two channels.

two channels. The signal in each channel as a function of SHG wavelength λ_{SHG} is shown in Figure 3.14B. At $\lambda_{ex} = 835$ nm ($\lambda_{SHG} = 417$ nm), the average signal in each channel was equal.

The images obtained in the two channels at $\lambda_{ex} = 835$ nm are shown, and analysis of the 2D Fourier transforms indicated that the two images are spatially registered. Therefore, we can assume that all excitation wavelengths contained in the pulsed source are causing SHG in both images. Subtraction was used to remove the contribution from wavelengths $\lambda_{SHG} > 417$ nm in channel 1 (Figure 3.14C). The image obtained using $\lambda_{ex} = 838$ nm was used to represent the $\lambda_{SHG} > 417$ nm contribution and was scaled by a factor of 0.5 before subtracting. The scaling factor was chosen to minimize the effect of imposing a ‘negative’ image on the original image. Similarly, subtraction of the contribution from wavelengths $\lambda_{SHG} \leq 417$ nm was performed on the channel 2 image acquired at $\lambda_{ex} = 835$ nm using the channel 1 image acquired at $\lambda_{ex} = 832$ nm (Figure 3.14D). The difference images should

represent SHG signal resulting from either the lower ($830 < \lambda_{ex} < 835$, Figure 3.14C) or higher ($835 < \lambda_{ex} < 840$, Figure 3.14D) excitation wavelengths contained in the spectral spread of the laser source. When the 2D Fourier components of the two difference images were compared, a shift of $2.8 \mu\text{m}$ was found in the y dimension. The shift in the difference image is different than the relative shift between the two subtracted images (which were shifted $3.9 \mu\text{m}$ with respect to one another), indicating that the shift is a result of actual spatial separation of excitation wavelengths at the focal plane. The calculated shift in images obtained with two channels is consistent with the expected shift for wavelengths on either end of the 10 nm bandwidth of the laser centered at 835 nm.

3.3.4 Summary

We showed that multiplexing with SHG can be done easily and cleanly with two excitation sources and two spectrally resolved detectors. Further parallelization with one excitation source is feasible, but challenging for a source with 10 nm spectral bandwidth since the spatial separation of such wavelengths at the focal plane is tricky and detection with very high spectral resolution is required. A specialized supercontinuum source would have advantages of easier separation of excitation wavelengths at the focal plane and more relaxed detection requirements. If necessary, pulse shaping could be used to maintain a tight temporal profile or to selectively choose a few particular wavelengths within the supercontinuum (Pillai et al., 2009). The Meta detector from Zeiss can collect emitted light and separate into component wavelengths detected by an array of PMTs with a minimum bandwidth of 10.7 nm for each channel. The Meta detector can collect a maximum of 32 channels with up to 8 channels acquired at the same time.

3.4 Resonant scanning with remote focusing

High speed 2D imaging techniques for multiphoton microscopy include parallelization techniques (Bewersdorf et al., 1998), faster scanning with resonant scanners, polygon mirrors, or AODs (Bullen et al., 1997; Fan et al., 1999; Kim et al., 1999), and alternative illumination strategies like using light sheet microscopy. All of these methods can be combined with remote focusing for rapid axial scanning to achieve high speed 3D imaging. This chapter details the design and implementation of a high speed volumetric imaging system using resonant scanners that can scan in a single plane with 500×500 pixels at 40 frames/s. This is faster than any commercially available system (see Table 3.3). For volumetric imaging, it incorporates an electrically tunable lens for axial scanning to acquire data from volumes with n planes at a rate of $40/n$ volumes/s.

In order to design this fast scanning system, scanning in both the lateral and axial dimensions was optimized. In Section 3.4.1, technical aspects for fast scanning in two dimensions are considered, followed by the design and characterization of an upgraded scanning microscope in Section 3.4.2. The characterization of the remote focusing scheme is described in Section 3.4.3. Finally, the versatility of the complete system to enable the *in vivo* study of vascular blood flow and neural connectivity is demonstrated.

3.4.1 Technical considerations for fast scanning in 2D

To form an image with a laser scanning microscope, an excitation beam must be steered within a field of view to excite fluorescence, signal from each visited spot must be detected, and signal must then be recorded. The acquisition speed of the microscope is determined by the rate at which these events can be completed. Limiting factors on overall speed include the scan speed of the mirrors or other elements used to steer the beam, available photons for detection, sensitivity and response time of the detector, the bandwidth of the signal amplifier, and the sample rate of the data acquisition card used to digitize the signal.

Scan systems.

Most fast scanning systems use either polygon mirrors, resonant scanners, or acousto-optic deflectors (AODs) to achieve high speed raster scanning. An AOD changes the exit angle of a laser beam by imposing a diffraction grating on the medium inside the AOD by driving an adjacent piezoelectric transducer with electric signal. Since there are no physical moving parts, its speed is not limited by inertia. It has the advantage of fast update rates, which allows user-defined scan patterns that are not limited to raster mode. However, because AODs rely on diffraction to function, their efficiency is wavelength dependent and they require dispersion compensation. Polygon mirrors can achieve very high scan speeds because they can spin very fast and can have many facets, however, the scan speed is generally fixed, and the scan angle cannot be changed. Therefore, the only way to ‘zoom’ on a region is to throw away laser light that hits the sample outside the desired field of view. Resonant scanners operate at a single resonant frequency, oscillating back and forth with amplitude determined by the voltage supplied to the motor. There is no feedback loop that allows the scan pattern to change, so the dwell time and scan pattern are fixed. A table that compares the benefits and functionality of these three high speed scanning systems is presented as Table 3.2.

For our upgraded system, we chose to use scanning mirrors over AODs to avoid the need for dispersion compensation, which would add to overall system complexity and greatly reduce available laser power. Furthermore, AODs have limited scan angles, which limits the size of the FOV. Between the scanning systems, we chose the resonant scanning approach since the scan angle, and therefore the size of the FOV/pixel pitch, is adjustable. A practical downside to resonant scanners is the squealing noise they produce because of their high scan frequencies. For this reason, it is best to choose something outside the audible range if possible ($>16\text{kHz}$).

Table 3.2: Comparison of high-speed 2D scanning methods, adapted from Prairie Tech.

Resonant scanner	Polygon mirror	Acousto-optic deflector
Wavelength independent	Wavelength independent	Limited wavelength
Audible noise	No audible noise	No audible noise
Fixed dwell time	Fixed dwell time (for fixed rotation speeds)	Dwell time customizable
No beam conditioning	No beam conditioning	Requires dispersion compensation
Adjustable scan angle	Fixed scan angle	Adjustable scan angle (limited)

Fluorescence excitation efficiency

From Equation 1.48, the efficiency of two-photon excitation depends strongly on the spatial confinement of the delivered light (determined by geometric factors of the focusing lens and properties of the medium in which light is focused), and the power of the excitation source (which is greatly increased through the use of pulsed lasers).

A few simple steps can be taken to maximize fluorescence excitation efficiency. First, the NA specified for an infinity-corrected objective assumes that the input light completely fills the back aperture of the objective lens. Therefore, scan lenses should be chosen such that the magnification of the laser beam slightly overfills the back aperture. The back aperture of the 20x objective used in our system has a diameter of 18 mm, the scan mirrors can pass a 3 mm beam, and the tube lens designed to match the objective lens has a focal length of 180 mm. To provide sufficient magnification ($M = f_2/f_1$), the scan lens should have a focal length of 30 mm. However, lenses with $f=30$ mm are only available with diameters of 1" or less. The diameter of the scan lens presents another aperture through which light must pass. This limits the scan angles and, therefore, the FOV at the sample plane. Therefore, there is a trade-off between NA and FOV. For our system as described in section 2.2.2, a 2" scan lens with $f=50$ mm was used to allow imaging of larger FOVs, though the back aperture of the objective is underfilled. Here, we are pushing the limits of imaging speed, so it is

essential that all aspects of the scan system are optimized. This can be done by choosing the 30 mm scan lens, sacrificing FOV size with the 20x objective, or by using an objective lens with a smaller back aperture. In data presented towards the end of the chapter using this high-speed system, an objective lens with a smaller back aperture (that was completely filled) was used.

Pulse spreading occurs when the laser pulse travels through optics, since the frequencies contained in the pulse travel at different speeds through the glass in the system. Dispersion precompensation can be done to keep a pulse width short using prisms that delay faster wavelengths. Our upgraded system uses a higher power laser with pulse precompensation for maximum excitation efficiency.

Optimized fluorescence collection

The available signal ultimately depends on the amount of emitted fluorescence. Fluorescence scales with excitation intensity, so increasing the laser power will increase the fluorescence emission. However, there is a trade-off between increasing the laser power and photodamage. By scanning faster, the dwell time of the laser is decreased at each pixel. If average power incident on the sample remains constant, the power per pixel will be reduced inversely with the increase in scan rate. Therefore, faster frame rates will be fundamentally limited by the decrease in signal at each pixel as scan rates increase. In such systems, practical image speeds are essentially dictated by the number of excitation pulses per pixel dwell time. With lasers operating at repetition rates of 80 MHz, a common rate for Ti:Sapphire pulsed lasers such as the one used in our system, pixel dwell times of 100 ns are needed to ensure ~ 8 pulses per pixel. A discussion of parameters important for choosing detectors, amplifiers, and digitization for optimized fluorescence collection are discussed in the following sections.

Signal to noise performance. Signal to noise (SNR) performance is a main factor limiting speed. The SNR is determined by the available photons within range of the detector,

as well as the efficiency and dark noise of the detector. For PMT detectors, the two main types of noise are the dark current generated by photocathode thermionic emission and the shot noise resulting from signal current. For low light measurements, the DC offset of the dark current can be subtracted from the signal and the detection limit is governed by the fluctuations in dark noise. From (Hamamatsu Photonics, 2006, p 72), the detection limit, or light input required to produce an output current equal to the fluctuations in dark current (equivalent noise input, ENI), depends on the electron charge e , the anode dark current I_d , the current amplification μ , circuit bandwidth B , and anode radiant sensitivity S . The relationship is given by

$$ENI = \frac{\sqrt{2eI_d\mu B}}{S} \quad (3.3)$$

Based on equation 3.3, lower light levels can be detected using PMTs with low dark current and high sensitivity. Since light levels are lower when scanning faster, we needed to minimize equation 3.3, and, therefore, selected a PMT based on those parameters. In addition, we needed a PMT with a wide spectral response in the visible region, where most fluorophores emit. Finally, the PMT must have a fast temporal response to ensure that we can use high sampling frequencies, enabling high frame rate imaging. We chose the Hamamatsu H-7422-40P, which addressed these constraints.

Amplification and sampling. After the energy from collected photons is converted to a current, that current must be amplified and converted to a voltage for sampling. We needed an amplifier that could do this for sampling rates up to 10 MHz, which would provide 500 pixels per line on every image. We chose an amplifier with sufficiently high gain with a 10 MHz bandwidth (C9999, Hamamatsu). Sampling at 10 MHz, there are only 8 laser pulses per pixel, and the system was designed for a maximum sample rate of 10 MHz. If necessary, pixels can be binned or frames can be averaged to improve signal, at the cost of image resolution or frame rate.

Commercially available systems

The push for faster imaging technologies in fields such as neuroscience and embryology has resulted in the development of fast-scanning commercial multiphoton imaging systems (Table 3.3). Most of these systems have been developed and released in parallel with this thesis work, and include similar design choices for 2D scanning and detection. The commercial availability of such systems has increased since late 2009, when the original patent for two-photon laser microscopy expired (Denk et al., 1991, U.S. Patent 5,034,613). Specifications for several of these systems are summarized in Table 3.3.

3.4.2 Resonant scanning system design and characterization

Optical layout

A requirement for the resonant scanning optical design was that it could be incorporated into the existing microscope design. The physical layout for the dual beam microscope with resonant scanning is shown in Figure 3.15. In the schematic, the Mai Tai XF-1 provides the excitation light for the ‘slow’ galvanometric scan arm, and the Mai Tai HP is directed toward the resonant scanners for the ‘fast’ imaging mode. As shown, the system is capable of simultaneous dual beam imaging at different speeds by combining the beams after the scan lens of each respective arm (scan lens 1 and 2 in the diagram). Beam combination could be achieved using a dichroic mirror and carefully chosen excitation wavelengths or a PBS cube if the two excitation beams have orthogonal polarization. Alternately, each laser could be used individually. For the resonant scanning arm, it is better to use a NIR coated mirror than a dichroic or PBS at the beam recombination location for maximum throughput, since the mirror is less lossy than the other options. The high power laser can also be directed toward the galvo scanners by placing a prism mirror in the ‘optional mirror’ slot in the diagram.

For maximum collection efficiency in the single channel detection arm, we placed a VIS-coated lens as close to the 680 LP dichroic as possible (Figure 3.15C). Using a lens very

Table 3.3: Commercially available high-speed multiphoton microscopes

Imaging microscope	Image Size (pixels)	Frame Rate	Acquisition Speed	Scan system
Thorlabs Multiphoton Microscope	512×512	30 Hz	7.86 MS/s	Resonant x scanner @ 7.8 kHz, galvanometer y mirror
Olympus FV1200MPE	256×256	16 Hz	1.05 MS/s	Two independent, galvanometric scan mirrors
Zeiss LSM 710 NLO and LSM 780 NLO	512×512	8 Hz	2.10 MS/s	Two independent, galvanometric scan mirrors with max line rates of 4000 lines/s
Nikon A1R MP+ Multiphoton Confocal	512×512	30 Hz	7.86 MS/s	Resonant x scanner @ 7.8 kHz, galvanometer y mirror
Nikon A1MP Multiphoton Confocal Microscope	512×512	4 Hz	1.05 MS/s	Two independent, galvanometric scan mirrors
Leica TCS SP5 MP Broadband Confocal and Multiphoton Microscope	512×512	25 Hz	6.55 MS/s	Resonant x scanner @ 8 kHz, galvanometer y mirror
Prairie Ultima Multiphoton Microscopy System	64×64	10 Hz	41.0 kS/s	Two independent, galvanometric scan mirrors
	34×34	1 kHz	1.16 MS/s	Acousto-optic deflector
	512×512	25 Hz	6.55 MS/s	
This Work	500×500	40 Hz	10 MS/s	Resonant x scanner @ 10 kHz, galvanometer y mirror
	500×200	100 Hz		

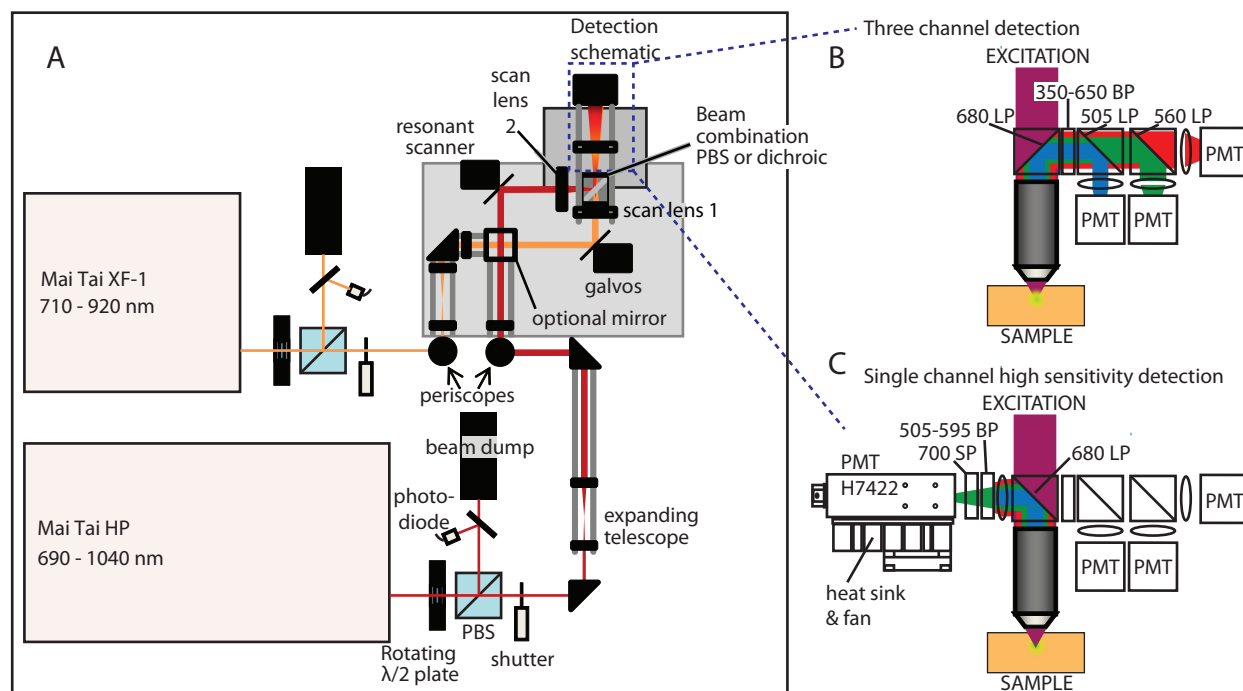


Figure 3.15: A. System schematic for our updated, fast scanning microscope. Two beam arms allow different scan speeds and imaging with either one or both excitation lasers simultaneously. The optional mirror can direct the Mai Tai HP beam toward either the resonant or the galvo scanners. B. Detection geometry for three spectrally resolved detection channels using R3896 PMTs. C. Single channel, more sensitive detection using the H7422 cooled PMT is achieved by rotating the orientation of the 680 LP dichroic mirror. LP, long pass filter; BP, band pass filter.

close to the dichroic is important for capturing photons that were scattered in the sample but remain within the collection angle of the objective, and therefore are not collimated when back-propagating through the objective towards the detector (Zinter and Levene, 2011). Efficiently collected fluorescence translates to better signal to noise, which in turn allows imaging at greater depths and at higher speeds. The detection geometry combined with the cooled high-sensitivity PMT discussed in section 3.4.1 provide optimized collection efficiency for our setup.

Synchronization & custom control software

The synchronization of scanning with acquisition of fluorescence data is a crucial part of software control. Precise knowledge of the position of the scanner in time allows accurate mapping of the fluorescence to its spatial origin. For our galvo scanning system, a string of voltages on multiple channels is generated that provides the scan position for both the x and y mirrors. The fluorescence signal is recorded in synchrony because it uses the same clock. In general, analog output and input signals can be synchronized if they share 1) a common timebase and 2) a triggered start.

The resonant scanning system differs from a galvo scan mirror system in that the frequency of the mirror scan is constant and specified by the manufacturer. Therefore, an arbitrary string of voltages cannot provide the scan pattern to the resonant scanner. Instead, the oscillation phase of the resonant scanner can be locked to an external clock with a frequency equal to that of the natural resonant frequency of the scanner (10kHz). For scanning in the y dimension, a galvanometer mirror is used, allowing variable frame rates. The analog drive signal for the y galvo must be synchronized with the external clock used to set the phase of the resonant scanner. The clock signal and y galvo analog output (AO) signal are both generated by a multifunction DAQ card (PCIe-6259, National Instruments).

A schematic showing the AO signals generated to image a single frame is shown in Figure 3.16. Signals are generated using NI-DAQ drivers and functions in LabVIEW. The timebase and the start trigger both come from a separate data acquisition card, and are shared by the AO and the counter output of the card. The staircase y galvo function increments twice each period of the 10 kHz, so that unique y data is acquired along both scan directions of the resonant scanner (i.e., bidirectional scanning). The number of y lines in an image is equal to $2 \times$ the number of resonant clock periods occurring during one staircase period.

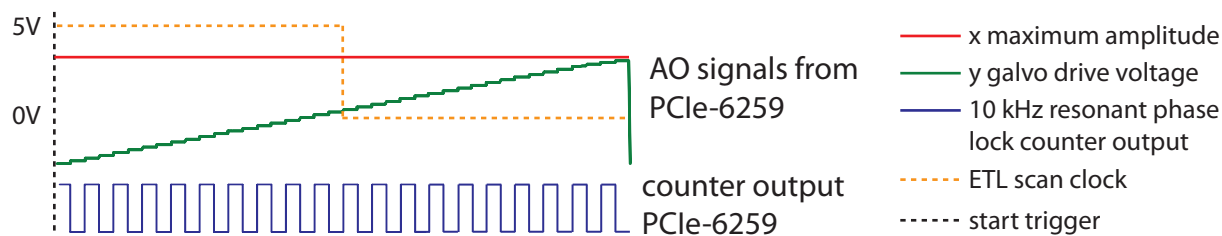


Figure 3.16: The AO signal generated to control the y galvo mirror (green) is synchronized with the counter output used to phase lock the x resonant scanner (blue) using an external start trigger and a shared timebase, which is locked to an external reference clock (not shown). The maximum scan amplitude of the resonant scanner is controlled via a constant applied voltage (red). The signals shown correspond to 1 frame. The ETL scan clock will be defined in the subsequent section and is included here for completeness.

Streaming to disk. Data is acquired at a sample rate of 10 MHz, corresponding to a 100 ns pixel dwell time, using an eight-channel, simultaneous sampling digitizer (PCI-5015, National Instruments). The position feedback signals of the x and y scan mirrors are collected along with the fluorescence data, so three channels of data are acquired. The digitizer uses NI-SCOPE drivers, and is synchronized to the NI-DAQ board used for data acquisition with LabVIEW. Typically, National Instruments data acquisition requests work by storing data on a card's onboard memory before transferring to the computer via a PCI(e) bus after all desired data has been fetched. In this case, several seconds of data need to be recorded, generating $>20\text{MB/s}$ per channel (16-bit data is needed to properly record from the 12-bit digitizer), which quickly exceeds the onboard memory of the card. Instead, data needs to be written to disk as it is acquired.

To stream to disk, a software trigger is configured for the data acquisition request, but is never sent. By doing so, pre-trigger data is fetched to onboard memory of the card in an ongoing loop. If the trigger were sent, data beginning at the trigger would then be sent to the computer. Instead, the pre-trigger data is fetched in chunks relative to a read pointer that indicates the position on the board memory, and the data goes to a queue that writes to a binary file as it is acquired. A caveat for this streaming method is that the data must be written to disk before it is overwritten in memory. To achieve this, the fetch size and queue

length (determining how often the write to disk operation is performed) can be adjusted using the LabVIEW user interface. Since the write function is slower than real-time, the amount of data that can be acquired is ultimately limited.

The digitizer is configured to output its reference clock in order to synchronize the scanning mirrors. It also outputs a start trigger when it begins writing data to memory, which provides the start signal to the AO board. The use of the software trigger for streaming data prevents a hardware triggered data acquisition, so the digitizer must provide the trigger source.

System level control. The file handling and synchronized data acquisition and signal generation for the resonant scanning system was written as a graphical user interface in LabVIEW. Because of physical space and hardware constraints (i.e., a limited number of PCI(e) slots), the resonant scanning data acquisition cards needed to be on a separate computer than the original microscope control software. As a result, the scan control and laser control are on two separate computers. In order to take an image, the main computer sends a signal to the resonant scan computer telling it that the laser shutter has opened and to begin acquiring data. When the scan is complete, the resonant scanning computer sends a signal back to the main control computer telling the laser shutter to close. Control of the translation stages and laser power remains with the main control computer.

Imaging viewing and online processing

Data acquired in pixel-by-pixel streaming mode needs to be 'reshaped' based on the laser scan pattern so that the image can be viewed. For scan mirrors moving at constant velocity in a raster scan, reshaping is done by assigning sequential data points to corresponding points in a rectangular x-y matrix. Since the resonant scanning mirror has a velocity that varies based on its position in a scan, the physical spacing of acquired pixels is uneven when acquiring pixels at fixed time intervals. The reshaping must take this into account. To do so,

Table 3.4: Specifications and components for upgraded scanning system

Parameter	Original hardware	Updated hardware
Scan system		
	Cambridge Tech. galvanometric scanning mirrors	EOPC 10kHz resonant scanning mirrors
Scan speed	4,000 lines/s (max)	20,000 lines/s
Excitation laser source		
	Spectra Physics Mai Tai XF-1	Spectra Physics Mai Tai HP
Laser power	> 900 mW @800nm	> 2.5 W @800nm
Detector		
	Hamamatsu R3896 PMT	Hamamatsu H7422-40 Cooled PMT
Rise time	2.2 ns	0.78 ns
Dark current	10 nA	0.4 nA
Cathode radiant sensitivity	90 mA/W @450nm 85 mA/W @550nm	108 mA/W @420nm 176 mA/W @550nm
TIA		
	Stanford Research Systems (SRS) Model SR570	Hamamatsu C9999
Bandwidth of TIA	1 MHz	10 MHz
Current-to-voltage conversion factor	1000 mV/ μ A	50 mV/ μ A
Data acquisition		
	National Instruments DAQ card NI PCI-6133	National Instruments Digitizer NI PCI-5105
Max acquisition rate	2.5 MHz	60 MHz
Minimum voltage range and sensitivity	-1.25 V, 1.25V 68.8 μ V	-25 mV, 25 mV 12.2 μ V

data is assigned to a rectangular x-y matrix, then the data points from each column (each sweep of the mirror) are interpolated onto a sinusoid.

The components for our upgraded scanning design are summarized in Table 3.4.

3.4.3 Remote focusing with an electrically tunable lens

A 2D fast scanning microscope like the one described in Section 3.4.2 can be converted to a volumetric imaging system by implementing remote focusing. In this section, characterization of volumetric imaging through the use of a commercially available electrically tunable lens (ETL) is presented.

Instrument design The ETL used here (EL-10-30-NIR-LD, Optotune) contains an optical fluid sealed with an elastic polymer membrane. An electromagnetic actuator exerts pressure on the fluid container, which causes a deflection of the lens that is proportional to the current drawn by the actuator (Optotune, 2013). The back focal length of this ETL decreases with increasing current, as shown by Figure 3.17C. The lens can be driven with an applied voltage, using Ohm's law where the resistance in the ETL is 12.5Ω at 25°C . A computer generated analog output signal is used to specify the voltage at the electric lens. Because the output current from the computer is limited to 5 mA, this output signal is buffered through a common collector stage, which is powered through a linear regulator connected to a DC supply, in order to provide sufficient current to drive the ETL. The schematic for this circuit is given in Figure 3.17B. Although this power configuration is accurate if the resistance of the ETL remains constant, the resistance changes with temperature. Thus, the focal length can drift if the ETL is heated either by laser light or by applying voltage. Drift can occur in particular at currents greater than 200 mA. In order to avoid drift due to temperature change, the best way to drive the ETL is with a constant current supply.

Since the ETL contains fluid that is necessary to cause a focal shift, gravitational effects can introduce wavefront aberrations if the lens is vertically oriented. In order to

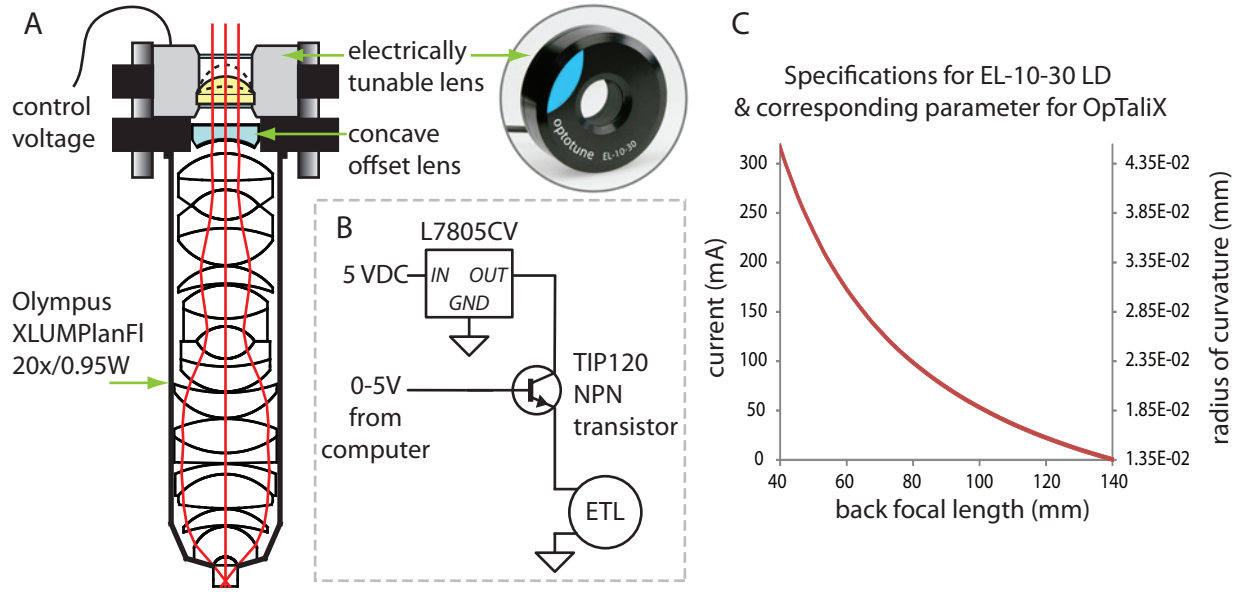


Figure 3.17: A. Experimental setup for remote focusing with an ETL and offset lens placed in front of an imaging objective. B. Circuit to provide voltage sent to the ETL set by a computer-generated analog output. C. The focal tuning range of the EL-10-30-NIR-LD. Applied current is on the left y-axis, and the curvature applied to the variable focus lens in the optical ray trace model to achieve the same behavior is on the right y-axis.

avoid these anticipated aberrations, the lens should be placed horizontally in the system. This restricts the location of the ETL to points along the beam path where the laser is directed vertically using periscope mirrors. In our system, there are two possible locations that meet this condition: before the scanning mirrors, or immediately in front of the objective lens. For dual plane imaging described in section 3.2, remote focusing was achieved using lens telescopes placed in the beam path before scanning mirrors. The physical distance between the telescopes and the objective limited the amount the beam could be conditioned since the diverging laser spot had to fit through all apertures in the downstream beam path. In (Grewe et al., 2011), the use of an ETL lens in combination with a concave lens creates a much shorter lens telescope that can be placed immediately before the objective for remote axial positioning. Here, we opted to place the lens in front of the objective, as depicted in Figure 3.17A.

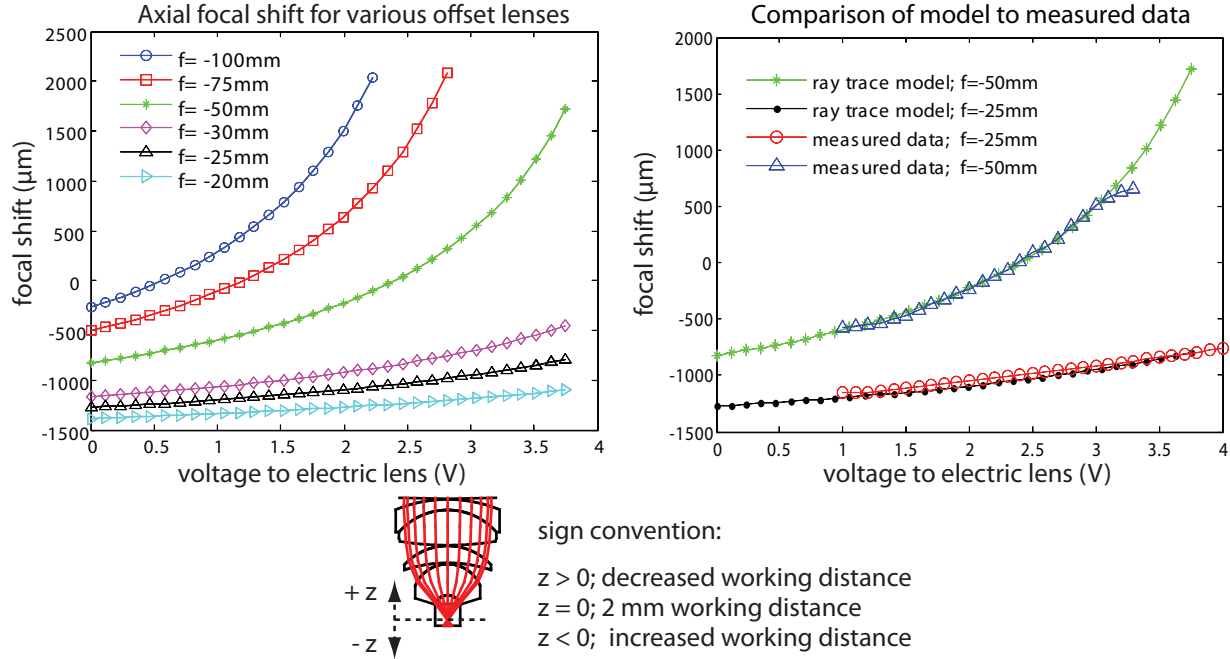


Figure 3.18: Left shows the expected axial focal shift with various offset lenses obtained using a ray trace model. Right shows good agreement between the modeled axial focal shifts and shifts measured using $3\text{ }\mu\text{m}$ fluorescent beads. Positive values correspond to a decreased working distance, as shown in the bottom panel.

Characterization. In order to characterize the expected performance of the ETL in our system, a ray trace model was created using the optical design software OpTaliX-LT. Three components were included in this model: the ETL, an offset lens, and the Olympus 20x water immersion objective used for multiphoton imaging. Specific objective lens components were obtained using information from patent literature (Takashi Kasahara, 2002, U.S. Patent 6,501,603, Embodiment 3), and ZEMAX models for the ETL and offset lenses were available from the websites for Optotune and Thorlabs, respectively. This model was used to calculate the expected axial focal shift in the sample for offset lenses with different focal lengths available from Thorlabs. The model result is shown in Figure 3.18.

The performance of two offset lenses chosen based on the modeled axial shifts were tested experimentally. The offset lens with $f = -25\text{mm}$ was chosen since it had a almost linear focal shift with applied voltage. Additionally, the axial shift was around $400\text{ }\mu\text{m}$ for the entire focal tuning range of the ETL. Since $400\text{ }\mu\text{m}$ is the approximate depth range for

two-photon imaging in scattering tissues, it is advantageous to have a similar shift using our remote focusing scheme so that the dynamic range of the ETL is fully utilized. The drawback associated with the $f=-25\text{mm}$ offset lens is the 1 mm shift away from the normal axial focus. The large shift affects the quality of the spot because aberrations become more significant as the distance of the spot from the true focus increases. A second offset lens with $f=-50\text{mm}$ was tested, since it can be used around the normal focal spot. Axial shifts were measured experimentally using a characterization slide with $3\text{ }\mu\text{m}$ fluorescent beads (Spherotech FPS-3057-6). A piezoelectric positioning system was used to translate the objective and obtain stacks of the beads with various voltages applied to the ETL. Gaussian curves were fit to the axial intensity profiles of the beads in Matlab, and the change in the axial focus was calculated based on the z -values at the intensity maxima of the Gaussian curves. Figure 3.18 shows that the experimentally measured shifts agree very well with the simulated values.

By altering the divergence of the beam as it enters the imaging objective, the specified numerical aperture (NA) is affected. Our OpTaliX model was used to quantify this effect for offset lenses with focal lengths of -25 mm and -50 mm . The results of this simulation are shown in Figure 3.19. Since the probability of two-photon excitation scales with NA^4 , microscope objectives for multiphoton microscopy are designed to have large NA. The back aperture of the microscope objective should be overfilled slightly to ensure that the NA is fully utilized. Figure 3.19A illustrates that the NA of the 20x objective used for imaging is reduced from 0.95 to 0.55 by using a (collimated) beam with a diameter the size of the ETL aperture. Comparing to the case where the ETL is used with an applied voltage of 2.5V (corresponding to a near zero axial focal shift), the NA is only slightly reduced from 0.55 to 0.49 with the ETL and offset lens in place (Figure 3.19B). Undoubtedly, the adverse effects of the ETL on the NA of our objective would be mitigated if the apertures of the objective and the ETL were better matched.

As seen in Figure 3.19C, the effective NA of the lens increases as the axial focus

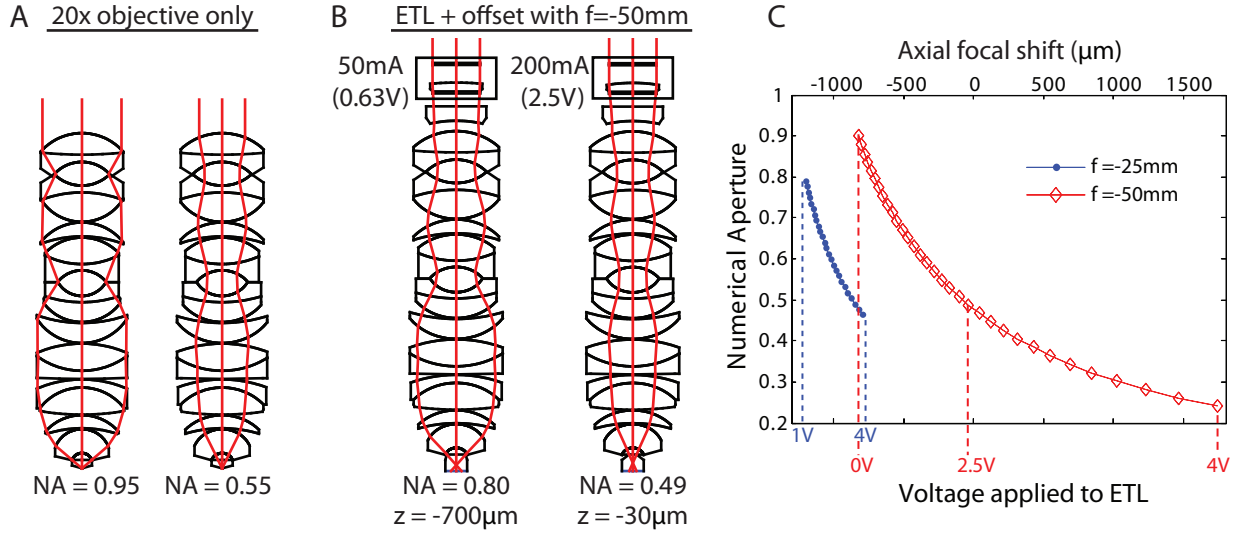


Figure 3.19: Effect of remote focusing with ETL on numerical aperture based on simulations in OpTaliX. A. Underfilling the back aperture of the objective causes a dramatic reduction in NA. Left shows the maximum NA of 0.95, right shows that the NA goes to 0.55 with a 10mm beam diameter (aperture of the ETL). B. Two examples of the change in NA with varying voltage applied to the ETL. C. Relationship between voltage applied to the ETL, axial focal shift, and NA for two offset lenses. Simulated input beam diameter was 10mm for the f=-50mm offset lens, and 6mm for the f=-25mm offset lens.

becomes more negative. At first, this seemed ideal since focusing deeper would provide an increased working distance while preserving the excitation efficiency of the objective. However, because the objective lens is designed to reduce optical aberrations for collimated input light, the performance of the objective is not nearly as good as intended for diverging light entering the back aperture. Therefore, even though the increased NA at more negative focal depths should give better resolution, the introduction of aberrations reduces image quality. To achieve the best possible image quality, we chose to use the offset lens with f=-50 mm, since it can be used around the zero axial focal shift.

The FOV is also affected by the divergence introduced into the beam before entering the objective. For cases where the axial focal shift is positive (a decreased working distance), the light entering the objective is slightly convergent. During scanning, this compressed beam has a larger angular spread than collimated scanned light. For negative axial shifts, the opposite is true. The change in scan angle results in an altered FOV when using the

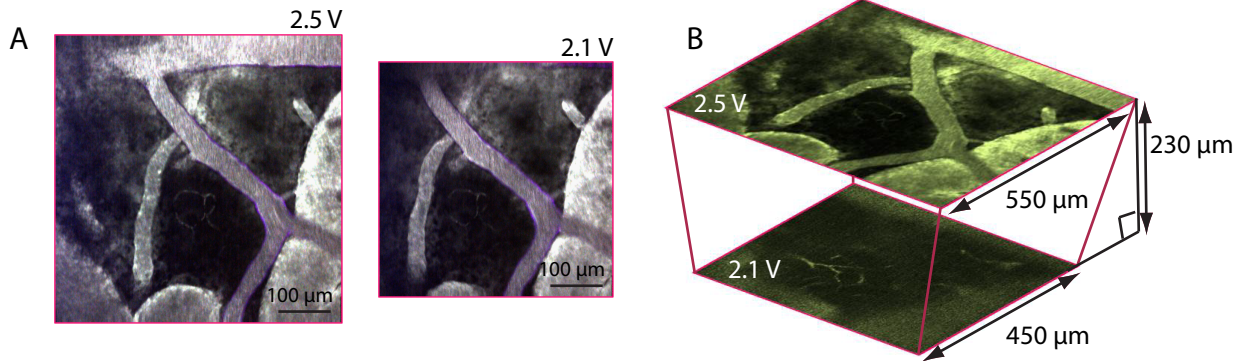


Figure 3.20: The effect of remote focusing on FOV using the ETL with a $f=-50\text{mm}$ offset lens. Images show vasculature labeled with FITC-dextran in an in vivo preparation. A. The same vessel region was imaged with 2.5V (left) and 2.1V (right) applied to the ETL. The 18% reduction in FOV is apparent. B. Images from the green emission channel show data from planes $230\text{ }\mu\text{m}$ apart acquired in rapid succession.

ETL and offset lens for remote focusing (Grewe et al., 2011). Figure 3.20 shows the FOV change using the $f=-50\text{mm}$ offset lens. The images depict the vasculature in an in vivo rat preparation using FITC-dextran as a vascular label. In figure 3.20A, a scan was acquired with 2.5V applied to the ETL in combination with the $f=-50\text{ mm}$ offset lens. The same region was imaged with 2.1V applied to the ETL by translating the objective up $230\text{ }\mu\text{m}$ using mechanical z-positioning. With the negative axial focal shift, the FOV was reduced by 18%, from $550\text{ }\mu\text{m}$ to $450\text{ }\mu\text{m}$. Further tests showed that the FOV changed linearly with axial shift.

Definition of scan types. With fast remote focusing in place, we were able to define new scan types for in vivo imaging. Since the ETL is positioned immediately before the objective lens, it can be used in either the resonant or galvanometric scan pathway. The lens can be used for fast volumetric imaging by updating the applied voltage to the ETL after each each frame. Alternately, the y-galvo can be held constant, and the lens can be used for fast axial scanning to produce x-z scans.

Figure 3.21 shows the voltage signals generated for the new scan types. In panels A and B, the voltages generated for volumetric scans with the original galvanometric scan

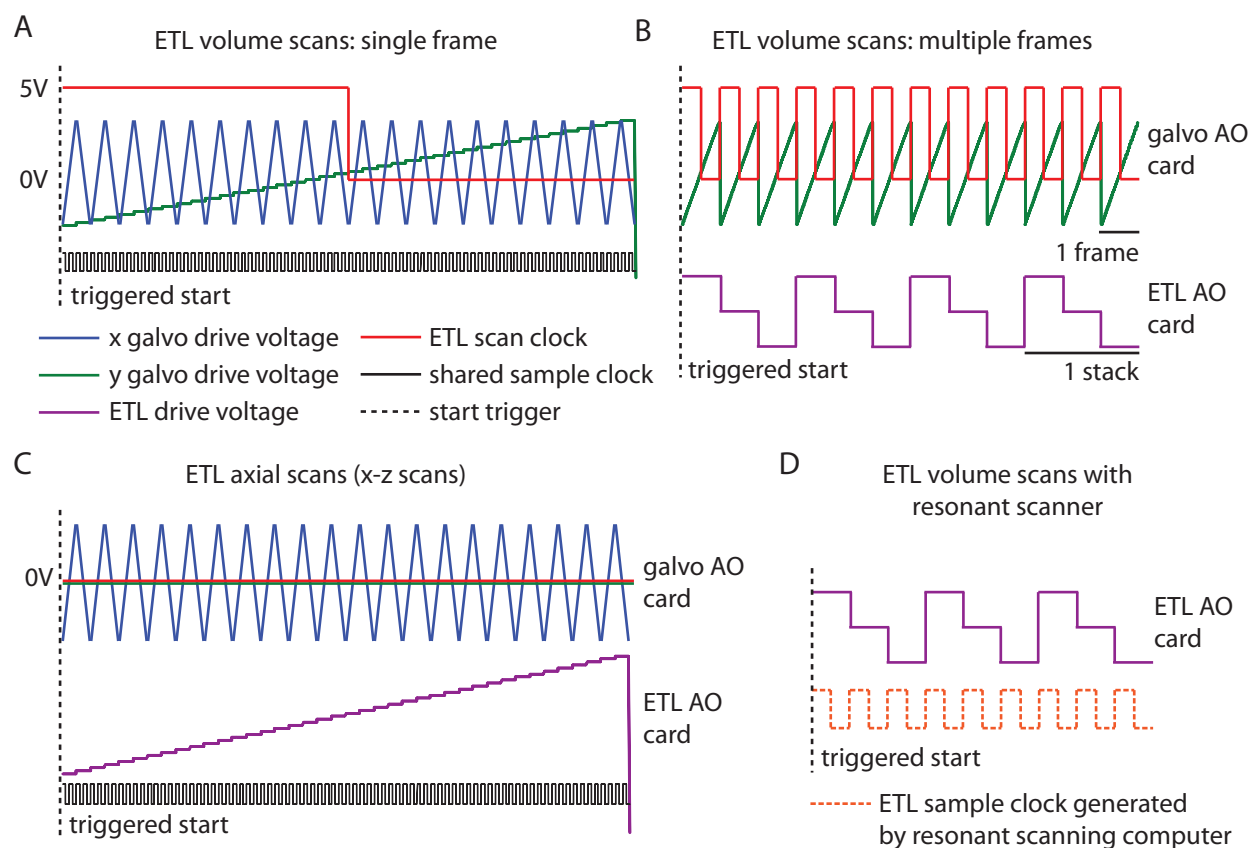


Figure 3.21: Analog output (AO) voltage signals generated for scan types that use the ETL. A and B. The AO voltages for volumetric scanning using the galvanometric mirrors in combination with the ETL. The signals queued to repeat on the galvo AO card are shown in A, and the signal generated by the ETL AO card during multiple frames is shown in B. Signals required for 4 stacks with 3 frames/stack are shown. C. AO voltages for x-z scanning are synchronized across the two AO cards using a shared sample clock and a triggered start. D. The sample clock for the ETL voltage pattern when imaging with the resonant scanner and the ETL is generated on the resonant control computer, Limberger.

mirrors are shown. For long acquisitions, a continuous AO signal must be provided to the scanning mirrors. To do this, the scan pattern for a single frame is queued to the AO card, and that same data is called repeatedly each time the queue is emptied past a threshold defined in the control software. By ‘re-queueing’ data in this way, continuous AO signals can be generated without requiring large onboard memory. The signal given to drive the ETL needs to change with every frame, so it does not repeat in the way a normal, single-frame, scan pattern does. The staircase signal going to the ETL needs to be on a slower clock for it to update properly. Since all AO channels on a given DAQ card must share a timebase, a separate DAQ card is required to control the ETL. To synchronize the ETL DAQ with the scan mirrors, a third AO voltage is generated on the scan mirror card, which is configured as the sample clock for the ETL AO. This sample clock is shown in red in A and B, and the ETL updates with each rising edge. For axial (x-z) scanning, a similar ETL pattern is used, however the sample clock is shared with the galvo mirror generating the x-waveform (Figure 3.21C). Finally, fast axial imaging can be combined with the resonant scan system, for fast volumetric imaging. In this case (3.21D), the sample clock comes from the resonant scanning computer, as shown in the previous section in Figure 3.16.

The control of the ETL voltage output is relatively simple to implement in software. When the user selects ‘volume scans’ or ‘axial scans’, the ETL AO is configured to use a sample clock wired to an input line corresponding to the correct clock signal.

3.4.4 In vivo demonstration of system capability

On its own, the development of a high frame rate 2D nonlinear microscope is useful for many applications. We have developed a custom system that not only matches or surpasses the current state of the art, commercial resonant scanning systems, but also has the ability to perform high speed axial scanning. When this remote focusing ability is coupled with either set of scan mirrors, our microscope offers unparalleled versatility. In this section, a range

Table 3.5: Imaging speed and characteristics for upgraded scan types. Pixel rates used to determine scan speeds for the original system with 3-channel detection are 500 kS/s, and for the resonant scanning system are 10 MS/s.

Scan type	Hardware	Range	Image Size	Speed
Axial scans	X-galvo, ETL, 20x objective	x: up to 750 μm	400 \times 400	3.125 Hz
		z: >500 μm	300 \times 200	8.33 Hz
Fast lateral scans	X-resonant, Y-galvo, 60x objective	x: up to 200 μm	500 \times 500	40 Hz
		y: up to 170 μm	500 \times 200	100 Hz
Volume scans	X,Y-galvos, ETL, 20x objective	x: up to 750 μm y: up to 750 μm z: >500 μm	300 \times 200 \times z planes	8.33/z Hz
Volume scans	X-resonant, Y-galvo, ETL, 60x objective	x: up to 200 μm y: up to 170 μm z: >150 μm	500 \times 500 \times z planes	40/z Hz

of in vivo demonstrations are discussed that showcase the value of this system for dynamic imaging in neuroscience.

Our volumetric microscope allows dual beam imaging, axial scanning, volumetric imaging with 3-channel detection, fast volumetric imaging with single channel detection. The characteristics and imaging speeds of our system are summarized by Table 3.5. Depending on the application, one of these imaging schemes can be used that is tailored to the experiment.

Axial scanning

With currently available, single plane imaging technologies, one of the most difficult things to study is the relationship between activity in different cortical layers of the brain. A simple but useful application of the ETL technology is for axial (x-z) scanning, which allows the visualization of many depths in the same frame.

Figure 3.22 demonstrates the use of axial scanning to visualize x-z planes in the vasculature. The rat was prepared as in section 3.2, and a bolus of FITC-dx was injected to the tail vein to provide vascular contrast, and astrocytes were labeled using Sulforhodamine

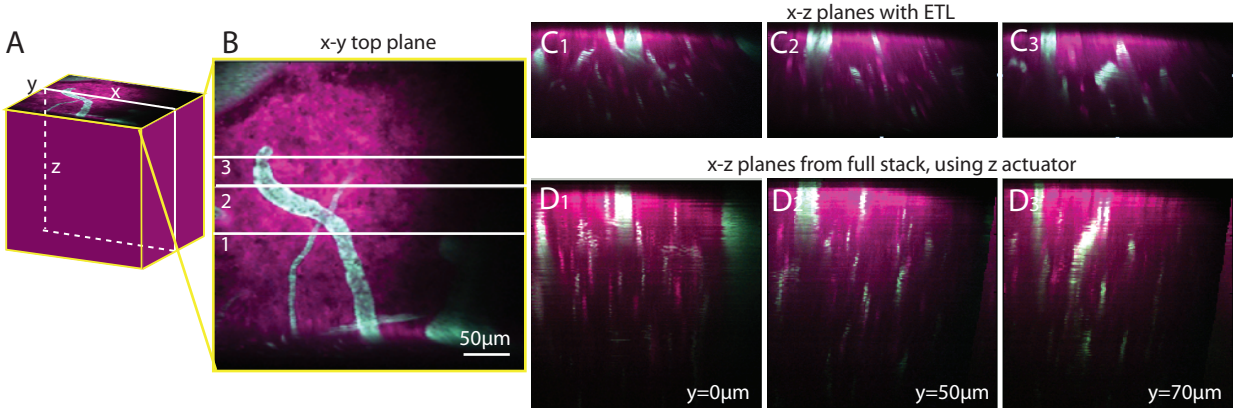


Figure 3.22: Demonstration of axial scanning to view vasculature. A. The total region imaged was a cube $400\text{ }\mu\text{m}$ on a side. The orientation of an example x-z plane is outlined in white. B. Top plane of the stack showing the y locations for the x-z scans shown in C and D. C. Axial slices acquired with the x-galvo and the ETL with a $f=-25\text{mm}$ offset lens. The z-dimension is $\sim 200\text{ }\mu\text{m}$, and the x-dimension is $400\text{ }\mu\text{m}$. Images 1, 2, and 3 correspond to the y positions indicated in B. D. X-Z slices taken from the full 3D data set, acquired sequentially using x-y scanning and an actuator for z-positioning.

101. The vasculature appears green, and astrocytes are visible as red spots. Axial slices at three different y cross-sections are shown in the figure. There is good agreement between the slices obtained using the ETL and the slices that were obtained by conventional 3D imaging of the volume. Because the images in D were acquired as 3D stacks, image acquisition took a minute or more. Brain motion during that time contributed to the discontinuities seen in the images. In contrast, the x-z planes acquired with the ETL are much smoother. Furthermore, the striations in the diving vessels show the shadows of blood cells flowing through the vessel.

Limitations on axial scanning frame rate include the response time of the ETL, which is 15 ms. Since the axial scan is produced by applying a voltage ramp to the ETL, the 15 ms settling time is only an issue when the ETL jumps back to the top of a scan. This can be addressed by changing the scan pattern to a triangle waveform (vs. a staircase), which would result in bidirectional z-scanning and minimize the effect of ETL settling time. The axial range of the scan is limited more by the degradation in power as a result of increased imaging depth in a scattering sample than by the range of the lens.

High frame rate lateral imaging

For imaging of very fast dynamics, such as blood flow, previous techniques have obtained quantifiable data by scanning only a small subset of the FOV. In (Kleinfeld et al., 1998), capillary blood flow was measured at depths up to 600 μm below the pial surface by performing line scans over vessels of interest. The resulting fluorescence signal ‘blinked’ when a red blood cell passed through the scan region, blocking fluorescence coming from the labeled blood plasma. The change in the signal from a single capillary with time can be used to calculate flow speed and red blood cell densities in capillaries. Since then, the line scanning technique has been used frequently to measure capillary flow (Chaigneau et al., 2003; Schaffer et al., 2006). Our fast scanning system has the ability to image capillary flow with full frame imaging. Given that the density of the capillary network increases with depth (McCaslin et al., 2010), the rapid acquisition of full planes for blood flow measurement is useful since it can measure flow in multiple capillaries simultaneously, as well as the capillary flow across branches in the vasculature. In addition, it is compatible with the use of other dyes that could label specific cell types (such as astrocytes or neurons with terminals in the layer of the brain that is under investigation) to study neurovascular coupling, or even metabolism.

Here, we imaged blood flow in an anesthetized mouse to demonstrate our resonant scanning system, using the 60x objective (LUMPlanFL N, Olympus) to focus the excitation light. The mouse was anesthetized using isofluorane, and a bolus injection of a mixture of ketamine/xylazine (0.01 ml/g, injected every ~ 2 hours) was used for anesthesia during surgical preparation and imaging. Figure 3.23 shows an example of the capillary measurements obtained in a full frame image, 80 μm below the pial surface of the brain. Speeds were calculated for two selected capillaries by computing the change in distance over time for the diagonal dark stripes in the position vs. time images (Figure 3.23B and C). Blood flow in the two capillaries is in different directions, but was calculated to be 202.3 $\mu\text{m/s}$ for the red selection, and 250 $\mu\text{m/s}$ for the blue selection. The flow speed was variable within a vessel,

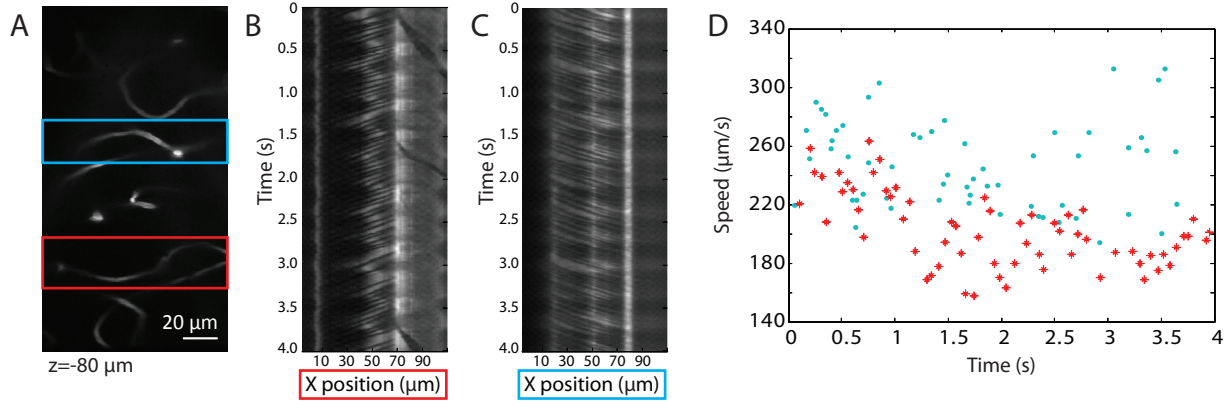


Figure 3.23: A. Full field measurement of capillary flow 80 μm below the pial surface. B. The red selection in A is averaged over the y dimension for all time points measured. Individual red blood cells are visible as dark stripes. Speed of flow can be calculated from the slope of the stripes. C. Same as B, data from the blue selected area. D. Speed (no direction) of capillary blood flow calculated from B and C. The mean speed of the flow within the red and blue selected areas is $202.3 \pm 25.2 \mu\text{m/s}$ and $250.1 \pm 33.5 \mu\text{m/s}$, respectively.

as shown in Figure 3.23D. Similar data was recorded to depths greater than 550 μm .

The speed of flow is slowest in the capillary beds, and faster for arteries and venules at the surface of the brain. Therefore, imaging flow in the arteries is even more challenging since the frame rates required are higher. We tested the ability of our system to track individual red blood cells in an arteriole 20 μm below the surface of the brain at 400 frames/s using a scan range of 500×50 pixels. Resulting images are displayed in Figure 3.24. Single cells can be tracked between frames (arrows), however the cell travels several lengths between each frame. This, combined with pixelated images, makes the speed of arterial flow difficult to compute even using 400 fps.

In order to better resolve the high speed arterial flow, we increased the frame rate by reducing the number of y pixels even further. Imaging at 1000 frames/s, we are closer to line scanning techniques than full-frame imaging since the number of pixels in the y dimension is limited. Figure 3.25 shows the region that was imaged and the spatial resolution available at 1000 frames/s. Still, this technique can resolve the region surrounding the vessel at low spatial resolution. The mean speed of flow in this arteriole was 3.295 mm/s, consistent with

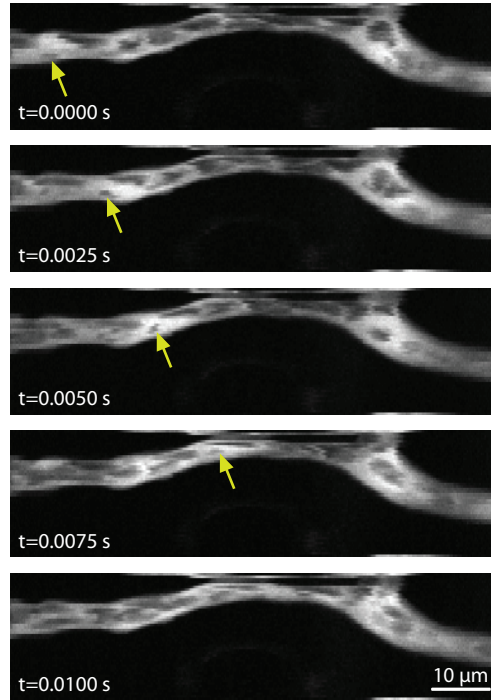


Figure 3.24: Frames displayed show a surface artery imaged at 400 fps using resonant scanners. Images are 500X500 pixels, pixelated. Individual cells can be tracked, but it is difficult.

previously reported results acquired using line-scanning (Santisakultarm et al., 2012). Also consistent with previously published results is the modulation of speed about the mean, which could be a measurement of pulsatory flow. However, since we did not record the mouse's heart rate during imaging, we are unable to confirm.

By imaging full fields at high frame rates, we were able to measure very fast blood flow at the surface of the brain, and capillary flow in complex networks at depths $>550 \mu\text{m}$. Further work could include the investigation of mechanisms regulating changes in the speed of flow, since different types of cells could conceivably be labeled and imaged simultaneously.

Multiplane imaging of neural networks and data analysis tools

An exciting application for our volumetric imaging technique is the study of neural networks. Through the use of genetically encoded calcium indicators, particular types of neurons can be labeled with fluorescent proteins that increase their fluorescent signal during

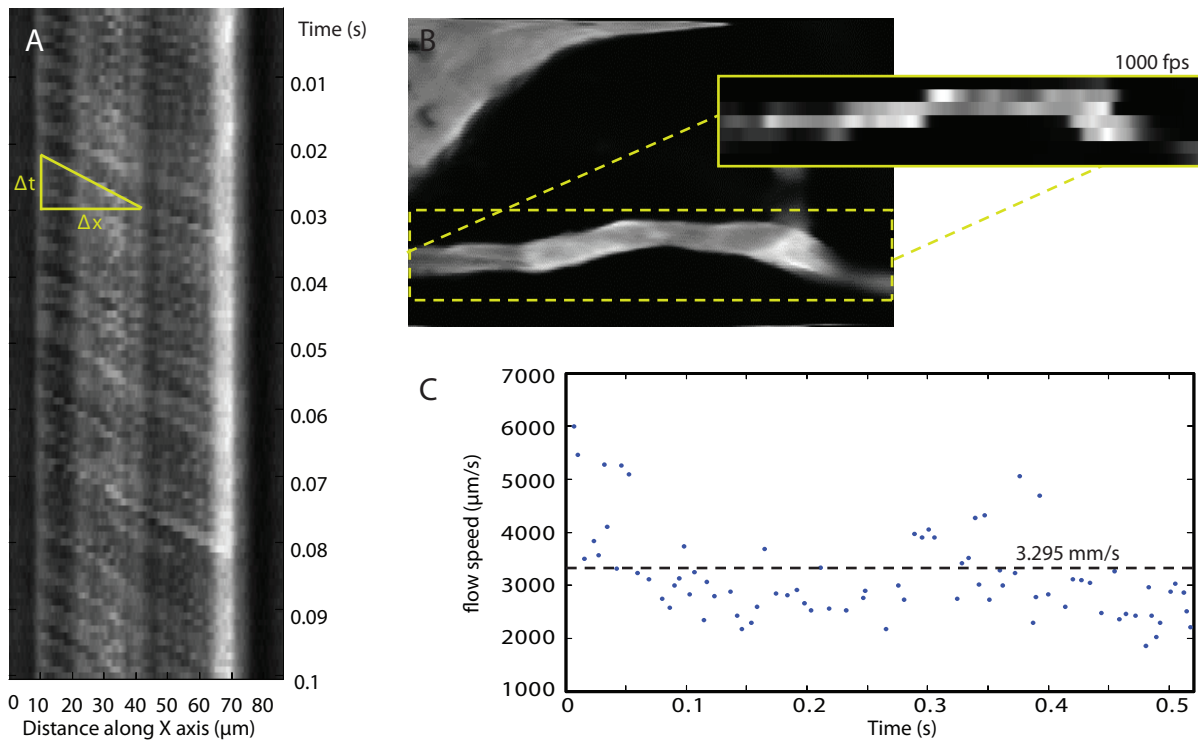


Figure 3.25: Arterial flow speed calculations using image sequences acquired 1000 frames/s. A. Image of the position along the x axis of the image with time. B. The region sampled at high speed is pixelated to achieve that frame rate. C. Average speed of flow is $3.295 \pm 1.4175 \text{ mm/s}$.

action potentials. Therefore, targeted experiments can be performed to study and analyze the development, connectivity, and function of complex neural networks.

Animal preparation. We applied our volumetric imaging technique to study neuronal firing patterns in an awake behaving mouse. A viral injection of the calcium indicator GCaMP5G (Akerboom et al., 2012) was used to induce fluorescent protein expression in layer 5 neurons. Although the cell bodies of the targeted neurons are $\geq 500 \mu\text{m}$ below the surface, dendritic projections extend to more superficial layers 2/3 to form connections and transmit information. A chronic cranial window was implanted over the motor cortex of the animal by a collaborator, and the mouse was trained to press a lever to get a reward in response to a task. A head plate was affixed to the skull of the mouse which allowed the head of the animal to be stabilized during imaging.

Volumetric imaging parameters. Time series images at multiple depths were acquired using the galvanometric scanning mirrors coupled with the ETL for z-scanning. The ETL was used in combination with an offset lens with $f=-50\text{mm}$ and the 20x objective lens. Individual images with 400×400 pixels, $125 \times 125 \mu\text{m}$ (bottom plane) were collected at 3.125 Hz. Three planes were sampled by driving the ETL with a staircase pattern with voltages of 2.5V, 2.45V, and 2.4V for the top, middle, and bottom planes, with corresponding square FOVs with side lengths 137, 131, and $125 \mu\text{m}$, respectively. With three planes per volume, the volumetric sampling rate was $3.125/3 = 1.04 \text{ Hz}$. The planes were separated by $75 \mu\text{m}$, and the top image was about $100 \mu\text{m}$ below the surface of the brain.

Data analysis. Data was acquired sequentially from top to bottom planes, such that images from the three planes were on slightly different time bases (shifted by $1/(3.125 \text{ Hz}) = 320 \text{ ms}$). Before display and further analysis, data from the three planes were interpolated to a shared time base. The time-series data from each pixel was upsampled $\times 3$, with extra

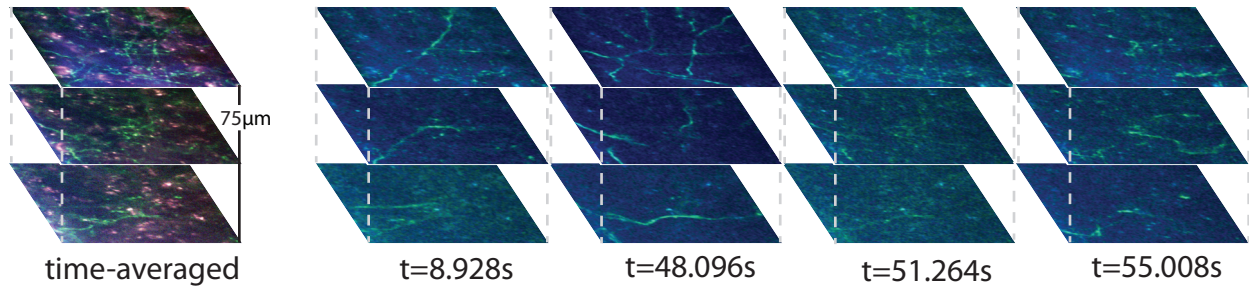


Figure 3.26: Volume imaging of GCaMP6 using the ETL and galvanometric scanning mirrors. The time-averaged images of the 3 planes show interlaced dendritic branches that mostly display green. The FOV goes from 137 μm with 2.5V to the ETL at the top plane to 125 μm with 2.4V to the ETL on the bottom plane. The 3 plane volumes were acquired at 1.04 Hz for a duration of 57 s. Snapshots of images at selected time points reveal dendritic activity.

data points calculated using linear interpolation.

Figure 3.26 shows snapshots at the three depths taken from the interpolated data set at time points exhibiting fluorescence activity. Data in the snapshots is shown from the blue and green channels only, to emphasize dendritic activity, which is visible mostly in the green channel. Images recorded from the three planes are clearly distinct layers, with little apparent cross-talk or instrument error. From shared fluorescence patterns in the data, dendritic connections can be investigated further.

By studying the time-averaged data from the green channel in each plane, a web of dendrites is visible (Figure 3.27A); however, because of their complex spatial arrangement, it is difficult to determine how they connect. Time-correlated signals from the three planes were examined to shed light on possible connections in the brain. Four time courses were chosen from small regions in the top plane with strong fluorescent activity, and are shown in Figure 3.27C. To create the maps presented in B, the cross correlation of the time series data at each pixel was computed for all four time courses. The resulting correlation maps could be displayed either as the spatial distribution of maximum correlation coefficients, or the time lag at each pixel that produced the maximum correlation. Since we were interested in segmenting the image based on the particular timing events shown in 3.27C, only correlations

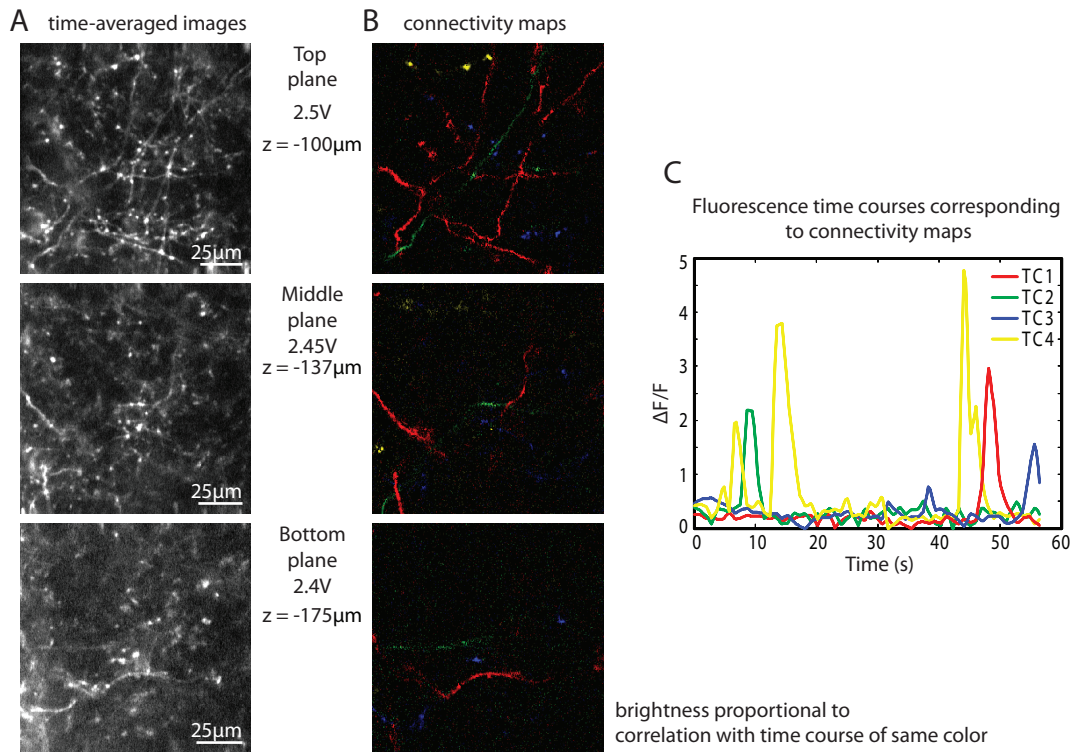


Figure 3.27: A. Time-averaged signal in the three image planes from the green emission channel. The decrease in FOV with increasing depth is indicated by the scale bars. Dendrites are visible but their complex, tangled arrangement makes it difficult to discern connectivity. B. Maps showing correlation of each pixel with the time courses shown in C. If a region is color-coded, it means it has a correlation coefficient with the corresponding time course that is proportional to the brightness, happening within a 2 second window of the time course. C. Time courses used for correlation maps in B.

coefficients with lags close to zero were used for the connectivity maps (3.27B). Masks were created for each correlation map to display data occurring only with $|\text{lag}| < 2$ seconds. The connectivity maps display are a merge of the four correlation maps filtered to have near zero lags. The colors in the merge correspond to the time courses shown, and the brightness of each pixel is proportional to the computed correlation coefficient.

In the first demonstration of the GCaMP5 class of dyes less than a year ago, in vivo image sequences in mice were recorded at maximum speeds of 50 Hz for images with 32×20 pixels, $20 \times 20 \mu\text{m}$, or 4 Hz for images with 512×250 pixels, $250 \times 250 \mu\text{m}$. Here, we have introduced a system that can acquire higher resolution images in multiple planes at comparable speeds. By implementing remote focusing with the resonant scanning system, we have the capability of imaging much faster. In addition, we have shown that correlation analysis can be performed on multiplane data, providing a powerful tool for determining connectivity and signal propagation characteristics in 3D regions of the neocortex.

Summary and future directions

This thesis presented the development and application of methods that enhance the information that can be obtained using nonlinear microscopy.

In Chapter 2, two-photon imaging was used to study freshly excised mouse tissues. By acquiring hyperspectral images that contained information from both excitation and emission properties of the tissues, we were able to better understand the biochemical contributors to intrinsic contrast images. Compared to bulk-tissue spectroscopy studies, hyperspectral microscopy offers more information on the spatial distribution of the biomolecules in specific tissue structures. Using structure-specific spectral signatures obtained from our hyperspectral data, we used linear unmixing for image segmentation. In this way, regions with similar chemical composition were separated from other structures within the image in an analogous way to specific chemical or histological staining. This technique can address the current clinical need for faster and less subjective processing of tissue samples to identify pathologies.

The second part of this work sought to improve temporal resolution for volumetric imaging. This research is motivated by the need for new technologies to study the complex dynamics and interrelationships of the many types of neurons in the brain and their relationship to blood flow and metabolism. In Chapter 3, three techniques for faster 3D imaging were presented:

- Our novel spectrally-encoding multiplexing technique uses the spectral properties of fluorescence to encode the spatial position of multiple images acquired in parallel. By using dyes as to label the vasculature, we used this technique to study spontaneous

fluctuations in vascular tone in the living rat brain. Abnormal blood flow in the resting state has been linked to numerous disorders, including anxiety and depression. The mechanisms that control activity in the resting state are currently unknown, and our technique is capable of providing images with sufficient spatial and temporal resolution to further investigate.

- By extending our spectral multiplexing strategy to harmonic generation, it is possible in principle to greatly increase the degree of parallelization, and therefore the volumetric imaging speed for SHG microscopy. We investigated the feasibility of this approach and demonstrated the technique using minimal modifications to our microscope system.
- The final method presented used high speed scanning mirrors coupled with remote focusing for positioning in three dimensions of a sample. This approach attains high volumetric acquisition speeds by using optimized scanning in all dimensions. Our state of the art research tool can be applied to study blood flow and neuronal activity, and would allow similar studies as we showed with our spectral parallelization technique. However, this upgraded system does not rely on spectral properties of the fluorophores present; therefore it is more versatile and can be used with virtually any fluorescent sample. This system has the potential to significantly contribute to neuroscience research, particularly now when there is significant general interest in brain activity and connectivity mapping.

Bibliography

- Abrat, B. M. K. T. I. and Masters, A. C. I. (2006). Endoscopic Confocal Microscopy Moves into the Clinic. *Biophotonics International*, (November).
- Akerboom, J., Chen, T.-W., Wardill, T. J., Tian, L., Marvin, J. S., Mutlu, S., Calderón, N. C., Esposti, F., Borghuis, B. G., Sun, X. R., Gordus, A., Orger, M. B., Portugues, R., Engert, F., Macklin, J. J., Filosa, A., Aggarwal, A., Kerr, R. A., Takagi, R., Kracun, S., Shigetomi, E., Khakh, B. S., Baier, H., Lagnado, L., Wang, S. S.-H., Bargmann, C. I., Kimmel, B. E., Jayaraman, V., Svoboda, K., Kim, D. S., Schreiter, E. R., and Looger, L. L. (2012). Optimization of a GCaMP calcium indicator for neural activity imaging. *The Journal of neuroscience : the official journal of the Society for Neuroscience*, 32(40):13819–40.
- Albota, M. (1998). Design of Organic Molecules with Large Two-Photon Absorption Cross Sections. *Science*, 281(5383):1653–1656.
- Amir, W., Carriles, R., Hoover, E. E., Planchon, T. A., Durfee, C. G., and Squier, J. A. (2007). Simultaneous imaging of multiple focal planes using a two-photon scanning microscope. *Optics Letters*, 32(12):1731.
- Anderson, J. S., Nielsen, J. A., Froehlich, A. L., Dubray, M. B., Druzgal, T. J., Cariello, A. N., Cooperrider, J. R., Zielinski, B. A., Ravichandran, C., Fletcher, P. T., Alexander, A. L., Bigler, E. D., Lange, N., and Lainhart, J. E. (2011). Functional connectivity magnetic resonance imaging classification of autism. *Brain*, 134(Pt 12):3739–3751.
- Anselmi, F., Ventalon, C., Bègue, A., Ogden, D., and Emiliani, V. (2011). Three-dimensional imaging and photostimulation by remote-focusing and holographic light patterning. *Proceedings of the National Academy of Sciences of the United States of America*, 108(49):19504–9.
- Attwell, D., Buchan, A. M., Charkpak, S., Lauritzen, M., MacVicar, B. A., and Newman, E. A. (2010). Glial and neuronal control of brain blood flow. *Nature*, 468(7321):232–243.
- Bahlmann, K., So, P. T., Kirber, M., Reich, R., Kosicki, B., McGonagle, W., and Bellve, K. (2007). Multifocal multiphoton microscopy (MMM) at a frame rate beyond 600 Hz. *Opt Express*, 15(17):10991–10998.
- Becker, V., Vercauteren, T., von Weyhern, C. H., Prinz, C., Schmid, R. M., and Meining, A. (2007). High-resolution miniprobe-based confocal microscopy in combination with video mosaicing (with video). *Gastrointestinal endoscopy*, 66(5):1001–7.

- Belgard, T. G., Marques, A. C., Oliver, P. L., Abaan, H. O., Sirey, T. M., Hoerder-Suabedissen, A., García-Moreno, F., Molnár, Z., Margulies, E. H., and Ponting, C. P. (2011). A transcriptomic atlas of mouse neocortical layers. *Neuron*, 71(4):605–16.
- Berg, J. M., Tymoczko, J. L., and Stryer, L. (2007). *Biochemistry*. W.H. Freeman, New York, 6th edition.
- Bewersdorf, J., Pick, R., and Hell, S. W. (1998). Multifocal multiphoton microscopy. *Optics Letters*, 23(9):655–657.
- Bohorfoush, A. G. (1996). Tissue spectroscopy for gastrointestinal diseases. *Endoscopy*, 28(4):372–380.
- Botcherby, E., Juškaitis, R., Booth, M., and Wilson, T. (2008a). An optical technique for remote focusing in microscopy. *Optics Communications*, 281(4):880–887.
- Botcherby, E. J., Booth, M. J., Juskaitis, R., and Wilson, T. (2008b). Real-time extended depth of field microscopy. *Optics Express*, 16(26):21843.
- Botcherby, E. J., Juskaitis, R., Booth, M. J., and Wilson, T. (2007). Aberration-free optical refocusing in high numerical aperture microscopy. *Opt Lett*, 32(14):2007–2009.
- Botcherby, E. J., Smith, C. W., Kohl, M. M., Débarre, D., Booth, M. J., Juškaitis, R., Paulsen, O., and Wilson, T. (2012). Aberration-free three-dimensional multiphoton imaging of neuronal activity at kHz rates. *Proceedings of the National Academy of Sciences of the United States of America*, 109(8):2919–24.
- Bouchard, M. B., Chen, B. R., Burgess, S. A., and Hillman, E. M. (2009). Ultra-fast multispectral optical imaging of cortical oxygenation, blood flow, and intracellular calcium dynamics. *Opt Express*, 17(18):15670–15678.
- Brown, E., McKee, T., DiTomaso, E., Pluen, A., Seed, B., Boucher, Y., and Jain, R. K. (2003). Dynamic imaging of collagen and its modulation in tumors in vivo using second-harmonic generation. *Nature medicine*, 9(6):796–800.
- Brown, E. B., Campbell, R. B., Tsuzuki, Y., Xu, L., Carmeliet, P., Fukumura, D., and Jain, R. K. (2001). In vivo measurement of gene expression, angiogenesis and physiological function in tumors using multiphoton laser scanning microscopy. *Nature medicine*, 7(7):864–8.
- Bullen, A., Patel, S. S., and Saggau, P. (1997). High-speed, random-access fluorescence microscopy: I. High-resolution optical recording with voltage-sensitive dyes and ion indicators. *Biophysical journal*, 73(1):477–91.
- Burgess, S. A. (2011). *Development and Applications of Laminar Optical Tomography for In Vivo Imaging*. PhD thesis, Columbia University.
- Cahalan, M. D. and Parker, I. (2008). Choreography of cell motility and interaction dynamics imaged by two-photon microscopy in lymphoid organs. *Annual review of immunology*, 26:585–626.

- Campagnola, P. J. (2008). Second-Harmonic Generation Imaging Microscopy of Structural Protein Arrays in Tissue. In Masters, B. R. and So, P. T. C., editors, *Handbook of Biomedical Nonlinear Optical Microscopy*, chapter 16, pages 377–411. Oxford University Press, New York.
- Campagnola, P. J., Clark, H. A., Mohler, W. A., Lewis, A., and Loew, L. M. (2001). Second-harmonic imaging microscopy of living cells. *J Biomed Opt*, 6(3):277–286.
- Campagnola, P. J. and Loew, L. M. (2003). Second-harmonic imaging microscopy for visualizing biomolecular arrays in cells, tissues and organisms. *Nat Biotechnol*, 21(11):1356–1360.
- Chaigneau, E., Oheim, M., Audinat, E., and Charpak, S. (2003). Two-photon imaging of capillary blood flow in olfactory bulb glomeruli. *Proceedings of the National Academy of Sciences of the United States of America*, 100(22):13081–6.
- Chaigneau, E., Tiret, P., Lecoq, J., Ducros, M., Knöpfel, T., and Charpak, S. (2007). The relationship between blood flow and neuronal activity in the rodent olfactory bulb. *The Journal of neuroscience : the official journal of the Society for Neuroscience*, 27(24):6452–60.
- Chalfie, M., Tu, Y., Euskirchen, G., Ward, W. W., and Prasher, D. C. (1994). Green fluorescent protein as a marker for gene expression. *Science*, 263(5148):802–805.
- Chance, B. (1954). Spectrophotometry of intracellular respiratory pigments. *Science*, 120(3124):767–775.
- Chance, B., Legallais, V., and Schoener, B. (1962). Metabolically linked changes in fluorescence emission spectra of cortex of rat brain, kidney and adrenal gland. *Nature*, 195:1073–1075.
- Chance, B., Schoener, B., Oshino, R., Itshak, F., and Nakase, Y. (1979). Oxidation-reduction ratio studies of mitochondria in freeze-trapped samples. NADH and flavoprotein fluorescence signals. *J. Biol. Chem.*, 254(11):4764–4771.
- Chen, B. R., Bouchard, M. B., Burgess, S. A., and Hillman, E. M. C. (2011). High-speed vascular dynamics of the hemodynamic response. *Neuroimage*, 54(2):1021–1030.
- Chen, J., Zhuo, S., Chen, R., Jiang, X., Xie, S., and Zou, Q. (2007). Depth-resolved spectral imaging of rabbit oesophageal tissue based on two-photon excited fluorescence and second-harmonic generation. *New J. Phys.*, 9.
- Chen, J. X., Lee, A., Zhao, J. H., Wang, H. Q., Lui, H., McLean, D. I., and Zeng, H. S. (2009). Spectroscopic characterization and microscopic imaging of extracted and in situ cutaneous collagen and elastic tissue components under two-photon excitation. *Skin Research and Technology*, 15(4):418–426.
- Cheng, A., Goncalves, J. T., Golshani, P., Arisaka, K., and Portera-Cailliau, C. (2011). Simultaneous two-photon calcium imaging at different depths with spatiotemporal multiplexing. *Nat Methods*, 8(2):139–142.

- Chia, S.-H., Yu, C.-H., Lin, C.-H., Cheng, N.-C., Liu, T.-M., Chan, M.-C., Chen, I.-H., and Sun, C.-K. (2010). Miniaturized video-rate epi-third-harmonic-generation fiber-microscope. *Optics Express*, 18(16):17382.
- Cohen, B. E. (2010). Biological imaging: Beyond fluorescence. *Nature*, 467(7314):407–8.
- Coons, A. H., Creech, H. J., and Jones, R. N. (1941). Immunological properties of an antibody containing a fluorescent group. *Proceedings of the Society for Experimental Biology and Medicine*, 47(2):200–202.
- Cothren, R. M., Richards-Kortum, R., Sivak Jr., M. V., Fitzmaurice, M., Rava, R. P., Boyce, G. A., Doxtader, M., Blackman, R., Ivanc, T. B., Hayes, G. B., and al., E. (1990). Gastrointestinal tissue diagnosis by laser-induced fluorescence spectroscopy at endoscopy. *Gastrointest Endosc*, 36(2):105–111.
- Cui, X. Q., Lee, L. M., Heng, X., Zhong, W. W., Sternberg, P. W., Psaltis, D., and Yang, C. H. (2008). Lensless high-resolution on-chip optofluidic microscopes for *Caenorhabditis elegans* and cell imaging. *Proceedings of the National Academy of Sciences of the United States of America*, 105(31):10670–10675.
- Čulić Viskota, J., Dempsey, W. P., Fraser, S. E., and Pantazis, P. (2012). Surface functionalization of barium titanate SHG nanoprobe for in vivo imaging in zebrafish. *Nature Protocols*, 7(9):1618–1633.
- Cyranoski, D. (2009). Microscopic marvels: The big and the bold. *Nature*, 459(7247):634–635.
- de Grauw, C. J., Frederix, P. L. T. M., and Gerritsen, H. C. (2002). Aberrations and Penetration in In-Depth Confocal and Two-Photon-Excitation Microscopy. In Diaspro, A., editor, *Confocal and Two-Photon Microscopy: Foundations, Applications, and Advances*, chapter 7, pages 153–169. Wiley-Liss, New York.
- Defelipe, J. (2011). The evolution of the brain, the human nature of cortical circuits, and intellectual creativity. *Frontiers in neuroanatomy*, 5:29.
- Deka, G., Wu, W.-W., and Kao, F.-J. (2013). In vivo wound healing diagnosis with second harmonic and fluorescence lifetime imaging. *Journal of Biomedical Optics*, 18(6):061222.
- Dela Cruz, J. M., McMullen, J. D., Williams, R. M., and Zipfel, W. R. (2010). Feasibility of using multiphoton excited tissue autofluorescence for in vivo human histopathology. *Biomed Opt Express*, 1(5):1320–1330.
- Demtröder, W. (2003). *Laser spectroscopy : basic concepts and instrumentation*. Springer, Berlin ; New York, 3rd edition.
- Denk, W., Strickler, J. H., and Webb, W. W. (1990). Two-photon laser scanning fluorescence microscopy. *Science*, 248(4951):73–76.

- Denk, W., Strickler, J. P., and Webb, W. W. (1991). Patent US 5,034,613 - Two-photon Laser Microscopy.
- Diaspro, A. (2002). *Confocal and two-photon microscopy : foundations, applications, and advances*. Wiley-Liss, New York.
- Diaspro, A. and Sheppard, C. J. R. (2002). Two-Photon Excitation Fluorescence Microscopy. In Diaspro, A., editor, *Confocal and Two-Photon Microscopy: Foundations, Applications, and Advances*, chapter 3, pages 39–73. Wiley-Liss, New York.
- Dickinson, M. E., Simbuerger, E., Zimmermann, B., Waters, C. W., and Fraser, S. E. (2003). Multiphoton excitation spectra in biological samples. *J Biomed Opt*, 8(3):329–338.
- Duemani Reddy, G., Kelleher, K., Fink, R., and Saggau, P. (2008). Three-dimensional random access multiphoton microscopy for functional imaging of neuronal activity. *Nat Neurosci*, 11(6):713–720.
- Duemani Reddy, G. and Saggau, P. (2013). High-speed two-photon imaging. *Cold Spring Harbor protocols*, 2013(1):pdb.top072603–.
- Fan, G. Y., Fujisaki, H., Miyawaki, A., Tsay, R. K., Tsien, R. Y., and Ellisman, M. H. (1999). Video-rate scanning two-photon excitation fluorescence microscopy and ratio imaging with cameleons. *Biophysical journal*, 76(5):2412–20.
- Fara, P. (2009). A microscopic reality tale. *Nature*, 459(7247):642–644.
- Farrar, M. J., Bernstein, I. M., Schlafer, D. H., Cleland, T. A., Fetcho, J. R., and Schaffer, C. B. (2012). Chronic in vivo imaging in the mouse spinal cord using an implanted chamber. *Nature methods*, 9(3):297–302.
- Fox, M. D. and Raichle, M. E. (2007). Spontaneous fluctuations in brain activity observed with functional magnetic resonance imaging. *Nat Rev Neurosci*, 8(9):700–711.
- Fox, M. D., Snyder, A. Z., Vincent, J. L., Corbetta, M., Van Essen, D. C., and Raichle, M. E. (2005). The human brain is intrinsically organized into dynamic, anticorrelated functional networks. *Proc Natl Acad Sci U S A*, 102(27):9673–9678.
- Freund, I. and Deutsch, M. (1986). Second-harmonic microscopy of biological tissue. *Opt Lett*, 11(2):94.
- Fukumura, D. and Jain, R. K. (2007). Tumor microvasculature and microenvironment: targets for anti-angiogenesis and normalization. *Microvascular research*, 74(2-3):72–84.
- Garritty, A. G., Pearlson, G. D., McKiernan, K., Lloyd, D., Kiehl, K. A., and Calhoun, V. D. (2007). Aberrant “default mode” functional connectivity in schizophrenia. *Am J Psychiatry*, 164(3):450–457.

- Georgakoudi, I., Jacobson, B. C., Muller, M. G., Sheets, E. E., Badizadegan, K., Carr-Locke, D. L., Crum, C. P., Boone, C. W., Dasari, R. R., Van Dam, J., and Feld, M. S. (2002). NAD(P)H and collagen as in vivo quantitative fluorescent biomarkers of epithelial precancerous changes. *Cancer Res*, 62(3):682–687.
- Göbel, W. and Helmchen, F. (2007). New angles on neuronal dendrites in vivo. *Journal of neurophysiology*, 98(6):3770–9.
- Gobel, W., Kampa, B. M., and Helmchen, F. (2007). Imaging cellular network dynamics in three dimensions using fast 3D laser scanning. *Nat Methods*, 4(1):73–79.
- Grewe, B. F., Voigt, F. F., van 't Hoff, M., and Helmchen, F. (2011). Fast two-layer two-photon imaging of neuronal cell populations using an electrically tunable lens. *Biomed. Opt. Express*, 2(7):2035–2046.
- Griffiths, D. J. (1999). *Introduction to electrodynamics*. Prentice Hall, Upper Saddle River, N.J., 3rd edition.
- Grosberg, L. E., Chen, B. R., and Hillman, E. M. C. (2012). Simultaneous multiplane in vivo nonlinear microscopy using spectral encoding. *Optics Letters*, 37(14):2967–2969.
- Haidekker, M. A., Brady, T. P., Lichlyter, D., and Theodorakis, E. A. (2005). Effects of solvent polarity and solvent viscosity on the fluorescent properties of molecular rotors and related probes. *Bioorganic chemistry*, 33(6):415–25.
- Hamamatsu Photonics, K. (2006). Photomultiplier Tubes: Basics and Applications, 3rd ed.
- Hecht, E. (2002). *Optics*. Addison-Wesley, Reading, Mass., 4th edition.
- Helmchen, F. and Denk, W. (2005). Deep tissue two-photon microscopy. *Nat Methods*, 2(12):932–940.
- Hillman, E. M., Devor, A., Bouchard, M. B., Dunn, A. K., Krauss, G. W., Skoch, J., Bacskaï, B. J., Dale, A. M., and Boas, D. A. (2007). Depth-resolved optical imaging and microscopy of vascular compartment dynamics during somatosensory stimulation. *Neuroimage*, 35(1):89–104.
- Hoover, E. E., Young, M. D., Chandler, E. V., Luo, A., Field, J. J., Sheetz, K. E., Sylvester, A. W., and Squier, J. A. (2010). Remote focusing for programmable multi-layer differential multiphoton microscopy. *Biomed Opt Express*, 2(1):113–122.
- Hsieh, C. L., Grange, R., Pu, Y., and Psaltis, D. (2010). Bioconjugation of barium titanate nanocrystals with immunoglobulin G antibody for second harmonic radiation imaging probes. *Biomaterials*, 31(8):2272–2277.
- Hu, M. and Polyak, K. (2008). Microenvironmental regulation of cancer development. *Current opinion in genetics & development*, 18(1):27–34.
- Huang, S., Heikal, A. A., and Webb, W. W. (2002). Two-photon fluorescence spectroscopy and microscopy of NAD(P)H and flavoprotein. *Biophys J*, 82(5):2811–2825.

- Jacques, S. L. and Prael, S. A. (1998). ECE532 Biomedical Optics.
- Jain, R. K., Munn, L. L., and Fukumura, D. (2002). Transparent Window Models and Intravital Microscopy: Imaging Gene Expression, Physiological Expression, and Drug Delivery in Tumors. In Teicher, B., editor, *Tumor Models in Cancer Research*, pages 647–671. Humana Press.
- Jiang, J. and Yuste, R. (2008). Second-harmonic generation imaging of membrane potential with photon counting. *Microscopy and microanalysis : the official journal of Microscopy Society of America, Microbeam Analysis Society, Microscopical Society of Canada*, 14(6):526–31.
- Jonkman, J. E. N. and Stelzer, E. H. K. (2002). Resolution and Contrast in Confocal and Two-Photon Microscopy. In Diaspro, A., editor, *Confocal and Two-Photon Microscopy: Foundations, Applications, and Advances*, chapter 5, pages 101–125. Wiley-Liss, New York.
- Jung, W., Tang, S., McCormic, D. T., Xie, T., Ahn, Y.-C., Su, J., Tomov, I. V., Krasieva, T. B., Tromberg, B. J., and Chen, Z. (2008). Miniaturized probe based on a microelectromechanical system mirror for multiphoton microscopy. *Optics letters*, 33(12):1324–6.
- Karling, J. S. (1939). Schleiden’s contribution to the cell theory. *American Naturalist*, 73:517–537.
- Kerr, J. N. D., Greenberg, D., and Helmchen, F. (2005). Imaging input and output of neocortical networks in vivo. *Proceedings of the National Academy of Sciences of the United States of America*, 102(39):14063–8.
- Kim, K. H., Buehler, C., Bahlmann, K., Ragan, T., Lee, W. C., Nedivi, E., Heffer, E. L., Fantini, S., and So, P. T. (2007). Multifocal multiphoton microscopy based on multianode photomultiplier tubes. *Opt Express*, 15(18):11658–11678.
- Kim, K. H., Buehler, C., and So, P. T. (1999). High-speed, two-photon scanning microscope. *Applied optics*, 38(28):6004–9.
- Kirkby, P. A., Srinivas Nadella, K. M. N., and Silver, R. A. (2010). A compact acousto-optic lens for 2D and 3D femtosecond based 2-photon microscopy. *Optics Express*, 18(13):13720.
- Kleinfeld, D., Mitra, P. P., Helmchen, F., and Denk, W. (1998). Fluctuations and stimulus-induced changes in blood flow observed in individual capillaries in layers 2 through 4 of rat neocortex. *Proc Natl Acad Sci U S A*, 95(26):15741–15746.
- Kobat, D., Horton, N. G., and Xu, C. (2011). In vivo two-photon microscopy to 1.6-mm depth in mouse cortex. *J Biomed Opt*, 16(10):106014.
- Konig, K. and Riemann, I. (2003). High-resolution multiphoton tomography of human skin with subcellular spatial resolution and picosecond time resolution. *J Biomed Opt*, 8(3):432–439.

- Kozberg, M. G., Chen, B. R., Deleo, S. E., Bouchard, M. B., and Hillman, E. M. (2013). Resolving the transition from negative to positive blood oxygen level-dependent responses in the developing brain. *Proc Natl Acad Sci U S A*, 110(11):4380–4385.
- Kurtz, R., Fricke, M., Kalb, J., Tinnefeld, P., and Sauer, M. (2006). Application of multiline two-photon microscopy to functional in vivo imaging. *Journal of neuroscience methods*, 151(2):276–86.
- Laiho, L. H., Pelet, S., Hancewicz, T. M., Kaplan, P. D., and So, P. T. (2005). Two-photon 3-D mapping of ex vivo human skin endogenous fluorescence species based on fluorescence emission spectra. *J Biomed Opt*, 10(2):24016.
- Lakowicz, J. R. (2006). *Principles of fluorescence spectroscopy*. Springer, New York, 3rd edition.
- Lakowicz, J. R. and Weber, G. (1973). Quenching of fluorescence by oxygen. Probe for structural fluctuations in macromolecules. *Biochemistry*, 12(21):4161–4170.
- Lansford, R., Bearman, G., and Fraser, S. E. (2001). Resolution of multiple green fluorescent protein color variants and dyes using two-photon microscopy and imaging spectroscopy. *Journal of biomedical optics*, 6(3):311–8.
- Lei, M., Xu, H., Yang, H., and Yao, B. (2008). Femtosecond laser-assisted microinjection into living neurons. *Journal of neuroscience methods*, 174(2):215–8.
- Liotta, L. A. and Rao, C. N. (1985). Role of the extracellular matrix in cancer. *Ann N Y Acad Sci*, 460:333–344.
- Masters, B. R. and So, P. T. C. (2008). *Handbook of biomedical nonlinear optical microscopy*. Oxford University Press, New York.
- McCaslin, A. F. H., Chen, B. R., Radosevich, A. J., Cauli, B., and Hillman, E. M. C. (2010). In-vivo 3D morphology of astrocyte-vasculature interactions in the somatosensory cortex: implications for neurovascular coupling. *J Cereb Blood Flow Metab*.
- McCaslin, A. F. H., Chen, B. R., Radosevich, A. J., Cauli, B., and Hillman, E. M. C. (2011). In-vivo 3D morphology of astrocyte-vasculature interactions in the somatosensory cortex: implications for neurovascular coupling. *J Cereb Blood Flow Metab*, 31:795–806.
- Mertz, J. (2004). Nonlinear microscopy: new techniques and applications. *Curr Opin Neurobiol*, 14(5):610–616.
- Mertz, J. and Moreaux, L. (2001). Second-harmonic generation by focused excitation of inhomogeneously distributed scatterers. *Optics Communications*, 196(1-6):325–330.
- Miller, M. J., Wei, S. H., Cahalan, M. D., and Parker, I. (2003). Autonomous T cell trafficking examined in vivo with intravital two-photon microscopy. *Proceedings of the National Academy of Sciences of the United States of America*, 100(5):2604–9.

- Miller, M. J., Wei, S. H., Parker, I., and Cahalan, M. D. (2002). Two-photon imaging of lymphocyte motility and antigen response in intact lymph node. *Science (New York, N.Y.)*, 296(5574):1869–73.
- Moreaux, L., Sandre, O., Blanchard-Desce, M., and Mertz, J. (2000). Membrane imaging by simultaneous second-harmonic generation and two-photon microscopy. *Opt Lett*, 25(5):320–322.
- Mukherjee, S., Wysock, J. S., Ng, C. K., Akhtar, M., Perner, S., Lee, M. M., Rubin, M. A., Maxfield, F. R., Webb, W. W., and Scherr, D. S. (2009). Human bladder cancer diagnosis using Multiphoton microscopy. *Proc Soc Photo Opt Instrum Eng*, 7161:nihpa96839.
- Münch, R. (2003). *Robert Koch und sein Nachlass in Berlin*. Number Bd 104. De Gruyter, Berlin ; New York.
- Nemet, B. A., Nikolenko, V., and Yuste, R. (2004). Second harmonic imaging of membrane potential of neurons with retinal. *J Biomed Opt*, 9(5):873–881.
- Newport (2011). *The Newport Resource* - <http://www.nxtbook.com/nxtbooks/newportcorp/resource2011/>.
- Nikolenko, V., Watson, B. O., Araya, R., Woodruff, A., Peterka, D. S., and Yuste, R. (2008). SLM Microscopy: Scanless Two-Photon Imaging and Photostimulation with Spatial Light Modulators. *Front Neural Circuits*, 2:5.
- Noonan, S. K., Haist, F., and Muller, R. A. (2009). Aberrant functional connectivity in autism: evidence from low-frequency BOLD signal fluctuations. *Brain Res*, 1262:48–63.
- Nuriya, M., Jiang, J., Nemet, B., Eishenthal, K. B., and Yuste, R. (2006). Imaging membrane potential in dendritic spines. *Proc Natl Acad Sci U S A*, 103(3):786–790.
- O’Connor Ilona, C. M. (2008). Developing the chromosome theory. *Nature Education*, 1(1).
- Ohtsuka, A., Piazza, A. J., Ermak, T. H., and Owen, R. L. (1992). Correlation of extracellular matrix components with the cytoarchitecture of mouse Peyer’s patches. *Cell Tissue Res*, 269(3):403–410.
- Olivier, N., Luengo-Oroz, M. A., Duloquin, L., Faure, E., Savy, T., Veilleux, I., Solinas, X., Debarre, D., Bourguine, P., Santos, A., Peyrieras, N., and Beaurepaire, E. (2010). Cell lineage reconstruction of early zebrafish embryos using label-free nonlinear microscopy. *Science*, 329(5994):967–971.
- Optotune (2013). Datasheet: EL-10-30-Series.
- Palero, J. A., de Bruijn, H. S., van der Ploeg van den Heuvel, A., Sterenborg, H. J., and Gerritsen, H. C. (2007). Spectrally resolved multiphoton imaging of in vivo and excised mouse skin tissues. *Biophys J*, 93(3):992–1007.
- Pantazis, P., Maloney, J., Wu, D., and Fraser, S. E. (2010). Second harmonic generating (SHG) nanoprobe for in vivo imaging. *Proc Natl Acad Sci U S A*, 107(33):14535–14540.

- Paoli, J., Smedh, M., Wennberg, A. M., and Ericson, M. B. (2008). Multiphoton laser scanning microscopy on non-melanoma skin cancer: morphologic features for future non-invasive diagnostics. *J Invest Dermatol*, 128(5):1248–1255.
- Papagiakoumou, E., de Sars, V., Oron, D., and Emiliani, V. (2008). Patterned two-photon illumination by spatiotemporal shaping of ultrashort pulses. *Opt Express*, 16(26):22039–22047.
- Pasteur, L. (2002). Summary report of the experiments conducted at Pouilly-le-Fort, near Melun, on the anthrax vaccination, 1881. *The Yale journal of biology and medicine*, 75(1):59.
- Pasteur, L. and H. C. Ernst, M. D. (2010). The germ theory and its applications to medicine and surgery, Read before the French Academy of Sciences, April 29th, 1878. Published in *Comptes Rendus de l' Academie des Sciences*, lxxxvi., pp. 1037–43.
- Pavlova, I., Hume, K. R., Yazinski, S. A., Peters, R. M., Weiss, R. S., and Webb, W. W. (2010). Multiphoton microscopy as a diagnostic imaging modality for lung cancer. *Proc Soc Photo Opt Instrum Eng*, 7569:756918.
- Pawley, J. B. (2006). *Handbook of biological confocal microscopy*. Springer, New York, NY, 3rd edition.
- Pena, A. M., Strupler, M., Boulesteix, T., Godeau, G., and Schanne-Klein, M. C. (2005). Spectroscopic analysis of keratin endogenous signal for skin multiphoton microscopy: erratum (vol 13, pg 6268, 2005). *Optics Express*, 13(17):6667.
- Pillai, R. S., Boudoux, C., Labroille, G., Olivier, N., Veilleux, I., Farge, E., Joffre, M., and Beaurepaire, E. (2009). Multiplexed two-photon microscopy of dynamic biological samples with shaped broadband pulses. *Optics Express*, 17(15):12741.
- Planchon, T. A., Gao, L., Milkie, D. E., Davidson, M. W., Galbraith, J. A., Galbraith, C. G., and Betzig, E. (2011). Rapid three-dimensional isotropic imaging of living cells using Bessel beam plane illumination. *Nature methods*, 8(5):417–23.
- Polyak, K., Haviv, I., and Campbell, I. G. (2009). Co-evolution of tumor cells and their microenvironment. *Trends in genetics : TIG*, 25(1):30–8.
- Porter, J. R. (1976). Antony van Leeuwenhoek: tercentenary of his discovery of bacteria. *Bacteriol Rev*, 40(2):260–269.
- Radosevich, A. J., Bouchard, M. B., Burgess, S. A., Chen, B. R., and Hillman, E. M. (2008). Hyperspectral in vivo two-photon microscopy of intrinsic contrast. *Opt Lett*, 33(18):2164–2166.
- Ramanujam, N. (2000). Fluorescence Spectroscopy In Vivo. In *Encyclopedia of Analytical Chemistry*, pages 20–56. John Wiley and Sons.
- Ramon y Cajal, S. (1899). Comparative study of the sensory areas of the human cortex.

- Rivera, D. R., Brown, C. M., Ouzounov, D. G., Webb, W. W., and Xu, C. (2012). Multifocal multiphoton endoscope. *Optics Letters*, 37(8):1349.
- Rogart, J. N., Nagata, J., Loeser, C. S., Roorda, R. D., Aslanian, H., Robert, M. E., Zipfel, W. R., and Nathanson, M. H. (2008). Multiphoton imaging can be used for microscopic examination of intact human gastrointestinal mucosa ex vivo. *Clin Gastroenterol Hepatol*, 6(1):95–101.
- Ross, M. H. and Pawlina, W. (2006). *Histology : a text and atlas : with correlated cell and molecular biology*. Lippincott Williams & Wilkins, Baltimore, MD, 5th edition.
- Saar, B. G., Johnston, R. S., Freudiger, C. W., Xie, X. S., and Seibel, E. J. (2011). Coherent Raman scanning fiber endoscopy. *Optics Letters*, 36(13):2396.
- Salomé, R., Kremer, Y., Dieudonné, S., Léger, J.-F., Krichevsky, O., Wyart, C., Chatenay, D., and Bourdieu, L. (2006). Ultrafast random-access scanning in two-photon microscopy using acousto-optic deflectors. *Journal of neuroscience methods*, 154(1-2):161–74.
- Santisakultarm, T. P., Cornelius, N. R., Nishimura, N., Schafer, A. I., Silver, R. T., Derschuk, P. C., Olbricht, W. L., and Schaffer, C. B. (2012). In vivo two-photon excited fluorescence microscopy reveals cardiac- and respiration-dependent pulsatile blood flow in cortical blood vessels in mice. *American journal of physiology. Heart and circulatory physiology*, 302(7):H1367–77.
- Sanz-Arigita, E. J., Schoonheim, M. M., Damoiseaux, J. S., Rombouts, S. A., Maris, E., Barkhof, F., Scheltens, P., and Stam, C. J. (2010). Loss of ‘small-world’ networks in Alzheimer’s disease: graph analysis of fMRI resting-state functional connectivity. *PLoS One*, 5(11):e13788.
- Schaffer, C. B., Friedman, B., Nishimura, N., Schroeder, L. F., Tsai, P. S., Ebner, F. F., Lyden, P. D., and Kleinfeld, D. (2006). Two-photon imaging of cortical surface microvessels reveals a robust redistribution in blood flow after vascular occlusion. *PLoS biology*, 4(2):e22.
- Shaner, N. C., Steinbach, P. A., and Tsien, R. Y. (2005). A guide to choosing fluorescent proteins. *Nature methods*, 2(12):905–9.
- Shen, Z., Lu, Z., Chhatbar, P. Y., O’Herron, P., and Kara, P. (2012). An artery-specific fluorescent dye for studying neurovascular coupling. *Nature methods*, 9(3):273–6.
- Skala, M. C., Riching, K. M., Gendron-Fitzpatrick, A., Eickhoff, J., Eliceiri, K. W., White, J. G., and Ramanujam, N. (2007). In vivo multiphoton microscopy of NADH and FAD redox states, fluorescence lifetimes, and cellular morphology in precancerous epithelia. *Proc Natl Acad Sci U S A*, 104(49):19494–19499.
- So, P. T. C. and Kim, D. (2008). An Optical Design Primer for Nonlinear Optical Microscopes. In Masters, B. R. and So, P. T. C., editors, *Handbook of Biomedical Nonlinear Optical Microscopy*, chapter 10, pages 244–265. Oxford University Press.

- Squirrell, J. M., Wokosin, D. L., White, J. G., and Bavister, B. D. (1999). Long-term two-photon fluorescence imaging of mammalian embryos without compromising viability. *Nature biotechnology*, 17(8):763–7.
- Supatto, W., Truong, T. V., Débarre, D., and Beaurepaire, E. (2011). Advances in multiphoton microscopy for imaging embryos. *Current opinion in genetics & development*, 21(5):538–48.
- Supekar, K., Menon, V., Rubin, D., Musen, M., and Greicius, M. D. (2008). Network analysis of intrinsic functional brain connectivity in Alzheimer’s disease. *PLoS Comput Biol*, 4(6):e1000100.
- Svoboda, K. and Yasuda, R. (2006). Principles of two-photon excitation microscopy and its applications to neuroscience. *Neuron*, 50(6):823–839.
- Sweet, R. A., Fish, K. N., and Lewis, D. A. (2010). Mapping Synaptic Pathology within Cerebral Cortical Circuits in Subjects with Schizophrenia. *Frontiers in human neuroscience*, 4:44.
- Takashi Kasahara (2002). Patent US 6,501,603 - Microscope objective lens.
- Theer, P. and Denk, W. (2006). On the fundamental imaging-depth limit in two-photon microscopy. *Journal of the Optical Society of America a-Optics Image Science and Vision*, 23(12):3139–3149.
- Theer, P., Denk, W., Sheves, M., Lewis, A., and Detwiler, P. B. (2011). Second-harmonic generation imaging of membrane potential with retinal analogues. *Biophysical journal*, 100(1):232–42.
- Theer, P., Hasan, M. T., and Denk, W. (2003). Two-photon imaging to a depth of 1000 microm in living brains by use of a Ti:Al₂O₃ regenerative amplifier. *Opt Lett*, 28(12):1022–1024.
- Tian, L., Hires, S. A., Mao, T., Huber, D., Chiappe, M. E., Chalasani, S. H., Petreanu, L., Akerboom, J., McKinney, S. A., Schreiter, E. R., Bargmann, C. I., Jayaraman, V., Svoboda, K., and Looger, L. L. (2009a). Imaging neural activity in worms, flies and mice with improved GCaMP calcium indicators. *Nature methods*, 6(12):875–81.
- Tian, L., Hires, S. A., Mao, T., Huber, D., Chiappe, M. E., Chalasani, S. H., Petreanu, L., Akerboom, J., McKinney, S. A., Schreiter, E. R., Bargmann, C. I., Jayaraman, V., Svoboda, K., and Looger, L. L. (2009b). Imaging neural activity in worms, flies and mice with improved GCaMP calcium indicators. *Nature methods*, 6(12):875–81.
- Tian, P., Teng, I. C., May, L. D., Kurz, R., Lu, K., Scadeng, M., Hillman, E. M., De Crespigny, A. J., D’Arceuil, H. E., Mandeville, J. B., Marota, J. J., Rosen, B. R., Liu, T. T., Boas, D. A., Buxton, R. B., Dale, A. M., and Devor, A. (2010). Cortical depth-specific microvascular dilation underlies laminar differences in blood oxygenation level-dependent functional MRI signal. *Proc Natl Acad Sci U S A*, 107(34):15246–15251.

- Truong, T. V., Supatto, W., Koos, D. S., Choi, J. M., and Fraser, S. E. (2011). Deep and fast live imaging with two-photon scanned light-sheet microscopy. *Nature methods*, 8(9):757–60.
- Tsien, R. Y., Adams, S. R., Griffin, B. A., Kerr, R., Li, W. H., Llopis, J., Miyawaki, A., Schafer, W. R., and Zlokarnik, G. (1998). Imaging protein interactions and gene expression in live cells. *Molecular Biology of the Cell*, 9:2A–2A.
- Wallace, M. B. and Kiesslich, R. (2010). Advances in endoscopic imaging of colorectal neoplasia. *Gastroenterology*, 138(6):2140–2150.
- Ware, W. R. (1962). Oxygen Quenching of Fluorescence in Solution: An Experimental Study of the Diffusion Process. *Journal of Physical Chemistry*, 66(3):455–458.
- Weinberg, R. A. (2006). *The Biology of Cancer*. Garland Science, 1st edition.
- Weinberg, R. A. (2008). Coevolution in the tumor microenvironment. *Nature genetics*, 40(5):494–5.
- Williams, R. M., Zipfel, W. R., and Webb, W. W. (2005). Interpreting second-harmonic generation images of collagen I fibrils. *Biophysical journal*, 88(2):1377–86.
- Wu, Y. and Qu, J. Y. (2006). Autofluorescence spectroscopy of epithelial tissues. *J Biomed Opt*, 11(5):54023.
- Xu, C. (2002). Cross-Sections of Fluorescence Molecules in Multiphoton Microscopy. In Diaspro, A., editor, *Confocal and Two-Photon Microscopy: Foundations, Applications, and Advances*, pages 75–99. Wiley-Liss, New York.
- Zakaryan, A., Karageuzyan, K., Hovsepyan, L., Karabashyan, L., and Zakaryan, G. (2001). Quantitative analysis of phospholipids and gangliosides in bone marrow progenitors of lymphocytes, thymocytes and mature lymphocytes in tumor-bearing animals. *Int Immunol*, 13(9):1141–1145.
- Zinter, J. P. and Levene, M. J. (2011). Maximizing fluorescence collection efficiency in multiphoton microscopy. *Optics Express*, 19(16):15348.
- Zipfel, W. R., Williams, R. M., Christie, R., Nikitin, A. Y., Hyman, B. T., and Webb, W. W. (2003). Live tissue intrinsic emission microscopy using multiphoton-excited native fluorescence and second harmonic generation. *Proc Natl Acad Sci U S A*, 100(12):7075–7080.
- Zoumi, A., Lu, X., Kassab, G. S., and Tromberg, B. J. (2004). Imaging coronary artery microstructure using second-harmonic and two-photon fluorescence microscopy. *Biophysical journal*, 87(4):2778–86.
- Zoumi, A., Yeh, A., and Tromberg, B. J. (2002). Imaging cells and extracellular matrix in vivo by using second-harmonic generation and two-photon excited fluorescence. *Proceedings of the National Academy of Sciences of the United States of America*, 99(17):11014–11019.